VILNIUS UNIVERSITY

INSTITUTE OF CHEMISTRY OF CENTER FOR PHYSICAL SCIENCES AND TECHNOLOGY

RAMŪNAS SKAUDŽIUS

SYNTHESIS AND INVESTIGATION OF CO-SUBSTITUTED YTTRIUM ALUMINIUM AND YTTRIUM GALLIUM GARNETS

Doctoral Dissertation

Physical Sciences, Chemistry (03 P)

Vilnius, 2014

The dissertation was carried out in Vilnius University in the period of 2010-2014.

Scientific supervisor:

Prof. Habil. Dr. Aivaras Kareiva (Vilnius University, Physical Sciences, Chemistry 03P)

Contents

LIST OF ABBREVIATIONS:

CN	Coordination number
CT	Charge Transfer
EN	Electronegativity
HS	High spin
LE	Luminous Efficacy
LED	Light Emitting Diode
LS	Low spin
LuGG	$Lu_3Ga_5O_{12}$
PL	Photoluminescence
QE	Quantum Efficiency
TQ	Thermal Quenching
UV/VIS	Ultraviolet/Visible
VUV	Vacuum Ultraviolet
XRD	X-ray Diffraction
YAG	$Y_3Al_5O_{12}$
YGG	$Y_3Ga_5O_{12}$
YIG	$Y_3Fe_5O_{12}$
YInG	$Y_3In_5O_{12}$

INTRODUCTION

Since 1926 when the preliminary structure of natural silicate minerals having cubic structure was determined the family of garnets became one of the most extensively studied group of compounds [1]. The mixed oxide systems have been of particular interest due to the stability and the fact that a wide range of properties can be obtained by substitution of one ion for another. Garnets containing transition metals and rare-earths carry many important technological uses as magnetic materials, as phosphor materials employed in solid state lasers, television screens and light-emitting diodes, as computer memories, as near UV and near IR radiation up/down-converting compounds in Si solar cells and in other devices as microwave optical elements. These mixed oxide systems also have a brilliance similar to diamond and were used as gemstones till the introduction of synthetic cubic zirconia [2-9].

The most popular garnet is yttrium aluminium garnet ($Y_3Al_5O_{12}$, YAG) which possesses good thermal and chemical stability and therefore it is an important composite for fluorescence [10]. YAG doped with Ce^{3+} [11], Tb^{3+} [12, 13], Er^{3+} [14, 15], Eu^{3+} [16-18] or Cr^{3+} [19] could be employed as the host material for multi-coloured phosphors. By selecting corresponding lanthanide ions may be produced red, green and (RGB) emission for use in tricolour white light [20, 21]. In addition, these phosphors are potential candidates for deep red light emitting diodes application, which could be used even for plants and vegetables cultivation [22, 23]. The human eye sensitivity in the deep red range is very low, but radiation in this wavelength range has a rather high penetration depth into biological matter [24], therefore the europium or chromium doped garnets also could be applied in the new field as optical imaging. The improvements in mechanical and optical properties, the new areas of applications provide a strong motivation for studying garnets in general.

It is well known that physical properties of crystalline materials are very dependent on the host material, phase purity, distribution of the grains sizes and crystalline homogeneity. In the YAG all aluminium ions may be substituted by

gallium or iron ions, while pure yttrium indium or yttrium scandium garnet is not obtained. The substitution limits on yttrium gallium-scandium and yttrium aluminium-gallium-scandium mixed metal garnets were discussed by Muliuoliene *et al.* and Garskaite *et al.* [25, 26], nevertheless the overall assumptions of substitution limits on mixed-metal garnets cannot be determined. Moreover, in mixed-metal garnets the preferred sites of aluminium and gallium, aluminium and iron or gallium and iron were discussed in literature, while the effect of distribution of trivalent cations among the octahedral and tetrahedral sites to the physical properties is still an open question [27-31].

The stoichiometry of cations and chosen synthesis route directly affect the phase formation of product. Traditionally YAG powders were synthesized by a solid-state reaction using the component oxides as starting materials. This technique requires repeated mechanical mixing and extensive heat treatment at temperatures as high as 1700 ºC. Due to insufficient mixing and the low reactivity of raw materials, using this method several intermediate phases such as monoclinic yttrium aluminate and perovskite yttrium aluminate phases easily can be obtained besides YAG in the final products [32, 33]. Meanwhile, the sol-gel route due to its apparent advantages of fine homogeneity, high reactivity of starting materials, easier composition control, lower sintering temperature and lower cost is one of the leading method for preparation of nanostructured ceramic materials and devices [34].

The motivation of this work was to synthesize new mixed-metal garnets by sol-gel method and to study their limitary radius. The investigation of the luminescence properties of new doped garnet crystal structure compounds was also in the field of interest. Finally, the research was focused on the correlation between the structure and the luminescence properties of europium doped garnets which are the potential candidates for the NIR laser or optical imaging applications.

Therefore, the main aims of the present thesis were formulated as follows:

1. To synthesize using sol-gel processing route and characterize mixed-metal $Y_3(Al,M)_5O_{12}$ garnets (M = Ga, In, Cr, Mn, Fe, Co, Ni or Cu); and to investigate the metal substitution limit on the formation of garnet phase.
2. To synthesize and investigate PL properties of lanthanide (Ln = Ce^{3+}, Eu^{3+}, Tb^{3+} and Er^{3+}) and indium or lanthanide and chromium co-doped YAG ($Y_3(Al,In)_5O_{12}$:Ln and $Y_3(Al,Cr)_5O_{12}$:Ln, respectively).
3. To investigate the dependence of the $^5D_0$-$^7F_4$ transitions of Eu^{3+} on the local environment in different garnets.
4. To grow and characterize single crystals of YAG:Eu^{3+}, YGG:Eu^{3+}, $Y_3(Al,In)_5O_{12}$:Eu^{3+} and $Y_3(Ga,In)_5O_{12}$:Eu^{3+}.

1. LITERATURE OBSERVATIONS

1.1. Garnets

The garnet minerals contain an important and widespread group of rock-forming silicates distinguished by their chemical diversity, close structural similarity and physical properties. The first synthetic garnets were synthesized in the middle of XX century. Yttrium-aluminium garnet (YAG) was first synthesized by Yoder and Keith in 1951 [35]. Synthesis of yttrium-gallium (YGG) garnet was accomplished by Keith and Roy in 1954 [36]. The powders of yttrium-iron garnets (YIG) which exhibit magnetic properties were investigated by Bertaut and Forrat in 1956 and by Geller and Gilleo in 1957 [37, 38]. The desirability of obtaining single crystals of these new materials for use in fundamental experimentation resulted the growth of single crystals of YIG by Nielson and Dearborn in 1957 [39]. Finally, since the laser operation of neodymium doped YAG was the first time demonstrated by Geustic *et al.* in 1964 [40], the development of the synthetic garnet have received the attention of the most modern technologies.

1.1.1. Structure of Garnets

Both synthetic and natural garnets are cubic (α = 11.2-13.1 Å), possess a relatively high refractive index and density (ρ = 3.5-7.1 g/cm^3), are hard, and if rare-earth elements are included, can exhibit any colour of the visible spectra. The structure belongs to the Ia3d space group with the cations in special positions (24c, 16a and 24d sites) and oxygen anions in general positions (96h site). The general chemical structural formula for an oxide garnet, with eight formula units per cell, can be written: $\{X\}_3[A]_2(B)_3O_{12}$.The notation in the formula labels the type of oxygen coordination polyhedra formed about each X, A, and B cations. The notation $\{\}$ refers to an eight-coordinated dodecahedral-site, $[]$ refers to a six-coordinated octahedral-site and $()$ refers to a four-coordinated tetrahedral-site. In the case of natural garnets, the formula can be

rewritten as $\{X\}_3[A]_2(SiO_4)_3$, where usually X = Fe^{2+}, Mg^{2+}, Mn^{2+}, and Ca^{2+} and A = Al^{3+}, Fe^{3+}, Cr^{3+} and V^{3+} [41]. The synthetic garnets with interesting properties are based on X = Y^{3+} and Y = Al^{3+}, Ga^{3+}, Sc^{3+} or Fe^{3+} (Fig. 1) where Y^{3+} may be completely or partially replaced by rare earths elements.

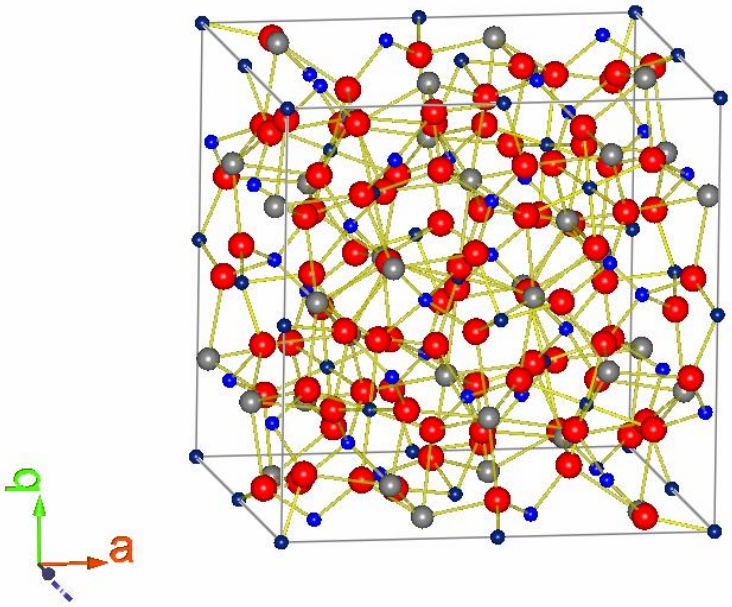

Fig. 1. Structure of YAG. Large red circles, large grey circles, small dark blue circles and royal blue circles represent O, Y, Al (16a) and Al (24d) atoms, respectively.

The structure has many shared edges between adjacent polyhedra. Each tetrahedron and octahedron share edges with two and six triangular dodecahedra, respectively. Each triangular dodecahedron shares edges with two tetrahedra, four octahedra and four other triangular dodecahedra. The tetrahedra and octahedra are linked to each other by sharing all corners (Fig 2.) [42].

The interatomic distances d_i (i = 4, 6, 8, 80, 48, 68, 88, 41, 61, 81, 82, 83) are labelled in Fig. 2. The cation-oxygen distances and shared and unshared edges (oxygen-oxygen distances) vary according to the chemical composition of the compound. The variation of the distances gives the information about the displacement of oxygen ions, covalency of the bonds, cation-cation repulsive force and shielding effect if the composition is changed.

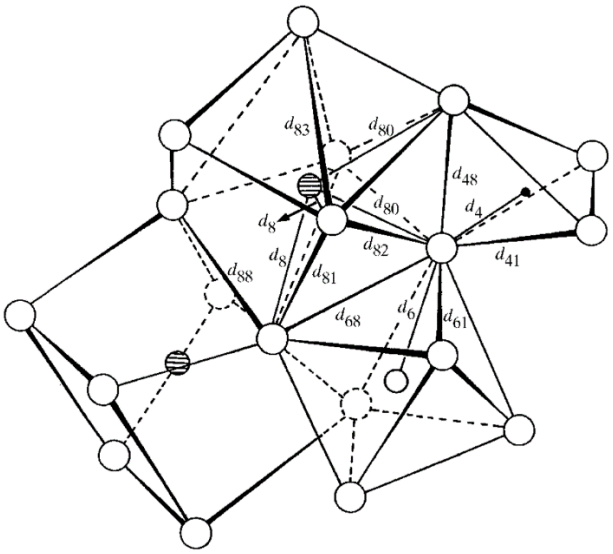

Fig. 2. Schematic O-atom coordination polyhedra in the garnet structure [42]. Large open circles, hatched circles, small open circles and small filled circles represent O atoms, the dodecahedral-site cations, the octahedral-site cations and the tetrahedral-site cations, respectively.

1.1.2. Limiting Radius

The structural variations of garnets are mainly induced by the variation of the cation sizes. The cation size is usually the determining factor of the choice of octahedral versus tetrahedral sites if the presence of covalent bonding (d^2sp^3 versus sp^3 hybridization) and/or ligand field stabilization are of small importance. Naturally, as the size (ionic radius r+) of a cation increases, more anions of a particular size can pack around it and vice-versa. For a specific structure, the limiting radius ratio can be calculated, which is the minimum allowable value for the ratio of ionic radii (r+/r-) for the structure to be stable. This value is important to determine the arrangement of the ions in different types of crystals. A cation will be stable in a curtain hole (tetrahedral, octahedral, cubic or cuboctohedral site) only if it is at least large enough to keep the anions from touching (Fig. 3) [43]. In general, as the cation decreases in size the lattice is stabilized, until anion-anion contact occurs. Further shrinkage of the lattice is impossible without a reduction in coordination number.

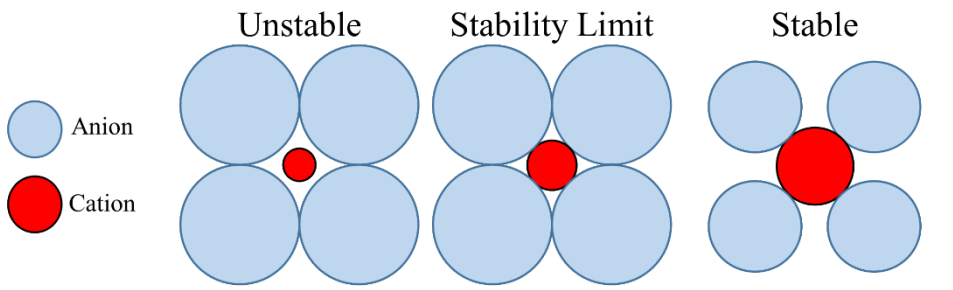

Fig. 3. Schematic view of the cations and anions in the lattice.

Table 1 summarizes the cation to anion radius ratios (r+/r-) for various coordination numbers and gives the name of the coordination polyhedron for each coordination number.

Table 1. Limiting radius ratio for various types of sites [43].

Coordination number	Geometry	r+/r- range
4	Tetrahedral	0.225-0.414
6	Octahedral	0.414-0.732
8	Cubic	0.732-1.000

The radius ratio is a useful, though imperfect, tool in the arsenal for predicting and understanding the behaviour of ionic compounds. The Nathan *et al.* had analysed 227 compounds and came to conclusion that radius ratio is expected to be reliable for compounds in which the cation coordination number is 8, moderately reliable for those with coordination number 6, and unreliable for those with coordination number of 4. Overall, the radius ratio rules are expected to hold about two-thirds of the time [44].

In garnets oxygen has coordination number four. According to the ionic radii presented in Table 2, cations with the radius of 0.31-0.57 Å and 0.57-1.01 Å should fit into the tetrahedral and octahedral sites, respectively. The size of four-coordinated aluminium, gallium and iron ions perfectly matches the ionic radius range for tetrahedral size, while the ionic radius of four-coordinated indium is too large for tetrahedral site. The theoretical data correlates with the practical results. The synthesis of pure YAG, YGG and YIG garnets is widely reported in literature, while yttrium-indium garnets is not obtained. Note, the six-coordinated gallium, iron and indium ions are in proper ionic radius to

occupy octahedral site, while aluminium theoretically is too small stably to fit in the six-coordinated site. This supplementary indicates that radius ratio is an imperfect tool. Moreover, it arise the question if the preferred choice of octahedral versus tetrahedral sites exists in the mixed-metals garnets.

Table 2. The ionic electronegativity (EN) [45, 46], Ahrens ionic radius (A-IR) [47] and effective ionic radius by Shannon (SH-IR) [48] of cations and oxygen in the various positions with different coordination number (CN).

Cation / Anion	Ionic EN (CN)	A-IR	SH-IR, Å (CN)
Al^{3+}	1.691 (IV) 1.513 (VI)	0.51	0.39 (IV) 0.535 (VI)
Ga^{3+}	1.755 (IV) 1.579 (VI)	0.62	0.47 (IV) 0.62 (VI)
In^{3+}	1.627 (IV) 1.480 (VI)	0.81	0.620 (IV) 0.800 (VI)
Cr^{3+}	1.587 (VI)	0.63	0.615 (VI)
Mn^{3+}	-	0.66	0.58 (VI, LS) 0.65 (VI, HS)
Fe^{3+}	1.726 (IV) 1.651 (VI, LS) 1.556 (VI, HS)	0.64	0.49 (IV) 0.55 (VI, LS) 0.645 (VI, HS)
Co^{3+}	1.693 (VI, LS) 1.621 (VI, HS)	0.63	0.545 (VI, LS) 0.61 (VI, HS)
Ni^{3+}	1.695 (VI, LS) 1.650 (VI, HS)	0.60	0.56 (VI, LS) 0.60 (VI, HS)
Y^{3+}	1.291 (VIII)	1.22	1.019 (VIII)
La^{3+}	1.281 (VIII)	1.10	1.16 (VIII)
Eu^{3+}	1.337 (VIII)	1.20	1.066 (VIII)
Gd^{3+}	1.336 (VIII)	1.20	1.056 (VIII)
Lu^{3+}	1.372 (VIII)	1.27	0.977 (VIII)
O^{2-}	-	-	1.378(4) (IV) 1.396(9) (VI)

1.1.3. Preferred Site Occupation

In the early work of the garnets the cation distribution was studied on the purpose to prepare the magnetic materials with controlled magnetic properties. In the paper written by Gilleo and Geller (1958) [49] was demonstrated that aluminium and gallium prefer tetrahedral sites in yttrium-aluminium-iron and yttrium-gallium-iron garnets, respectively. Nakatsuka *et al.* in 1995 and Rodic

et al. in 2001 discussed the structure and magnetic properties of these garnets in more details [28, 30]. The authors approve that Al^{3+} and Ga^{3+} ions prefer four-coordinated sites, but the motives are different. The aluminium is situated at four-coordinated site due to the smaller radius than iron, while the preference of gallium to tetrahedral site was explained by the nature of Ga^{3+} itself rather than the effect of ionic radius. Ions with the d^{10} electron configuration strongly tend to form sp^3-hybrid orbitals. The gallium ions also significantly prefers the tetrahedral site, contrary to the effect of cation size ($r_{Ga} > r_{Al}$, see Table 2) in yttrium-aluminium-gallium garnet [29]. The preference of Ga^{3+} for the tetrahedral site brought about the decrease in the cation-cation repulsive force across the polyhedral shared edges. Finally, gallium preferentially occupy tetrahedral sites in the spinel structure as in the garnet structure [50-53].

1.1.4. Applications

The garnet structure application began with the neodymium doped YAG as active laser medium in solid-state lasers in 1964. YAG:Nd lasers are widely used from low-power continuous-wave lasers to high power Q-switched (pulsed lasers) and produce infrared light at a wavelength of 1064 nm. If the YAG:Nd lasers are used with the frequency doubling or frequency tripling crystals, the green light with a wavelength of 532 nm or ultraviolet light at 355 nm are obtained [10, 54-57]. Recently, the YAG:Nd was improved by adding Cr^{3+}. A YAG:Cr^{3+} saturable absorber is widely used in numerous solid-state lasers to improve thermomechanical properties, to achieve higher average power and low saturable intensity. The YAG:Nd/YAG:Cr composite crystal is an ideal choice for small size and low cost lasers [58-60]. Beside the Nd^{3+} various efficient diode pumped lasers have been investigated on the basis of the rare-earth ions Er^{3+}, Tm^{3+}, Ho^{3+} and Yb^{3+} in combination with garnet host crystals [61-65]. All these lasers are used in industry and particularly in different fields of medicine (starting diagnostics ending surgery) [66, 67].

In recent decays it has been reported that the properties of rare-earth doped solid state compounds are under ongoing improvement for their application in

cathode ray tubes (CRTs), field emission displays (FEDs), electroluminescence displays (ELDs), plasma display panels (PDPs), fluorescent lamps (FLs) and white light emitting diodes (WLEDs) [68-72]. Eu^{3+} doped inorganic materials are successfully employed as orange to red emitting phosphors. These materials are characterized by a very high quantum efficiency, sufficient absorption strength and stability [73, 74]. One of the ways to improve Eu^{3+} phosphors for fluorescent light sources and emissive displays is the reduction of the emission in the range between 680 and 720 nm, because the human eye sensitivity strongly decreases at 650 nm and approaches almost nil at 700 nm. This leads to a respective decrease of luminous efficacy (LE) values. On the other hand, there might be other application areas, where a strong near infrared light is advantageous.

Exclusively the WLEDs have been the subject of increasing interest due to their potential applications in indicators, automobile headlights and general illuminations. Light emitting diodes exhibit excellent properties such as low level of power consumption and their durable lifetime. Moreover, if compared to fluorescent lamps, WLEDs are considered to be environment friendly because they are mercury free. Therefore, the WLEDs are expected to enable new applications in lighting field. The WLEDs are commonly fabricated with InGaN blue LED chips and yellow phosphors such as Ce^{3+} doped YAG, Eu^{2+} doped oxynitrides, and Eu^{2+}/Ce^{3+} doped silicate based materials [75, 76]. The YAG:Ce^{3+} has been the most widely used material because garnets are easy to synthesize with inexpensive, stable physical and chemical properties and are more luminescent compared to oxynitrides and silicate based materials [77].

In addition, rare-earth element doped garnets are used for improving materials in energy industry. Recently europium (III), europium (II), cerium (III), erbium (III), ytterbium (III), chromium (III) and neodymium (III) doped compounds (YAG, Y_2O_3, CaF_2, $NaYF_4$ and etc.) have been explored for up-conversion and down-conversion of near UV and near IR radiation to improve the overall efficiency of Si solar cells. Despite significant development of the photovoltaic industry over the past decades, the efficient and cost-effective

conversion of solar energy into electricity through photovoltaic cells remains a daunting task [9].

Energy storage is a supplementary issue. Lithium ion batteries are important for a wide variety of applications, spanning from portable electronics and hybrid automobiles to large-scale electrical power storage systems. In recent times, oxides with garnet related structures have gained a lot of attention as the potential solid state electrolyte for lithium ion batteries. The increasing the number of lithium per formula unit to five or seven, such as $Li_5La_3Y'_2O_{12}$ (Y′ = Bi, Sb, Na, Ta) or $Li_7La_3Y''_2O_{12}$ (Y″ = Zr, Hf, Sn), resulted an increase in ionic conductivity. The most effective ionic conductivity in garnet-related structures has been reported at room temperature for the cubic $Li_7La_3Zr_3O_{12}$. It shows good thermal stability against lithium metal, air and moisture, further showcasing its potential as the solid state electrolyte materials for future lithium ion batteries [78-81].

If aluminium or gallium is replaced by iron in rare-earth doped YAG or YGG, the changed composition garnets present unique magnetic and magneto-optical properties such as ferromagnetic ordering at room temperature, with constant magnetization over a large temperature range, ferromagnetic resonance and Faraday rotation among others. These features make this system one of the most promising materials for application in the technology of passive not-reciprocal and magneto-optical recording devices [82, 83]. YIG was employed for its narrow line width in magnetic resonance and controllable saturation magnetization in magnetic microwave devices, such as circulators, oscillators and phase shifters [84]. Praveena *et al.* synthesized gadolinium doped yttrium iron garnet nanopowders. The samples had low dielectric constant and losses and a broad distribution of FMR line width resulting the enhanced microwaves absorption properties [85]. Superparamagnetic YIG nanoparticles have been studied even for biomedical applications, such as magnetic field induced localized hyperthermia for the treatment of cancer [86, 87].

To summarize, recently, the new areas of application of garnets are discovered. Nevertheless, the homogeneity and phase purity of the final product

make a significant role for different applications. The choice of the appropriate synthesis route is a key to a successful work.

1.2. Synthesis of Garnets

Many different synthesis methods of synthetic garnets are described in the literature. In this chapter the main advantages and disadvantages of different synthesis routes for making powder and growing crystals will be reviewed.

1.2.1. Powder Synthesis

The solid-state reaction route is a widely used method for the preparation of powders from a mixture of the solid starting materials. The starting compounds are mixed and ground in an agate mortar. Sufficient amount of some volatile organic liquid (regularly acetone or alcohol) is added to the mixture to aid homogenization. During the process of grinding and mixing, the organic liquid gradually volatilizes and completely has evaporated in 10-20 minutes. Then the mixtures are annealed at different temperatures with intermediate pre-grinding. The first YAG was obtained from solid solutions at 1650-2180 °C temperature [35]. The first time YGG and YIG garnets were synthesized by solid state reaction at 600 °C (under pressure) and 1400 °C temperature, respectively [36, 38]. The requirement of extensive mechanical mixing and lengthy heat treatments at high temperatures to prevent the occurrence of intermediate phases are the main disadvantages of the solid-state synthesis of different aluminates, gallates or ferrates. The secondary phases such as perovskite $YAlO_3$ or metastable $Y_2Al_4O_7$ may be formed if YAG is synthesized by a solid-state reaction [88]. However, the simplicity and ease of industrialization production make the solid-state reaction route one of the most popular synthesis methods in the world.

Recently, wet-chemical processing of oxide systems attracts more and more attention of the scientists due to considerable advantages such as good mixing of the starting materials, excellent chemical homogeneity of the final products and lower synthesis temperatures compared with the solid-state

reaction. Various wet-chemical methods, which include combustion, co-precipitation, hydrothermal, spray pyrolysis, sol-gel and emulsion synthesis method have been developed and successfully used for a low-temperature production of phase-pure YAG, YGG, YIG powders and related systems.

Combustion is a synthesis route involving the exothermic reaction of an oxidizer such as metal nitrates, ammonium nitrate and ammonium perchlorate with an organic fuel, typically urea (CH_4N_2O), carbohydrazide (CH_6N_4O), or glycine ($C_2H_5NO_2$). This process was described in details by Kingsley *et al.* and McKittrick *et al.* [89, 90]. The combustion reaction is initiated in a muffle furnace or on a hot plate at 150-500 °C temperature. In a typical reaction, the precursor mixture of water, metal nitrates and fuel dehydrates, decomposes and ruptures into a flame. The combustion reaction itself is violently and hardly controlled, but if complete combustion occurs the only gaseous products obtained are N_2, CO_2 and H_2O, making this an environmentally clean processing technique. In general, a good fuel should react non-violently, produce non-toxic gases, and act as a complexant for metal cations. The chemical energy released from the exothermic reaction between the metal nitrates and fuel can rapidly heat the system to a momentum 1200-1900 °C temperature without any external heat source. The resultant product is a voluminous, foamy powder which can be easily milled becoming the precursor powder for desirable ceramics. Combustion synthesized powders are generally more homogeneous, have fewer impurities, smaller particle sizes and have higher surface areas than powders prepared by conventional solid-state methods. In general the particle size of the final product is nanoscale powders (30-90 nm). However, the size strongly depends on the final annealing temperature which affects the grain growth to micro-scale particles. By combustion method Ramanathan *et al.* using glycine as fuel have been able to synthesize YAG micro-scale powders at 1100 ºC [91], which is still too high in comparison with other methods. Liao *et al.* used varying amount of either glycine or urea, or mixture of them as fuel. The temperature of crystallization process was decreased while the particle size increased if more urea was added. Pure 25-900 nm scale terbium doped lutetium aluminium garnet

powder were obtained at 900-1000 °C [92]. Eventually the combustion method was improved by combining the combustion method with the sol-gel technique. The main idea of the improvement is that complexing agent (usually citric or tartaric acid) acts as a fuel for a combustion reaction. Recently, the number of different samples such as YIG, LuAG, YAG and YAG:Ce, using sol-gel combustion method were obtained at 800-900 °C. The average size of nano-powders was 30-100 nm range [93-96].

The wet-chemistry process is called a sol-gel route if complexing agent is used instead of the fuel. The simplified scheme of the sol-gel route is presented in Figure 4.

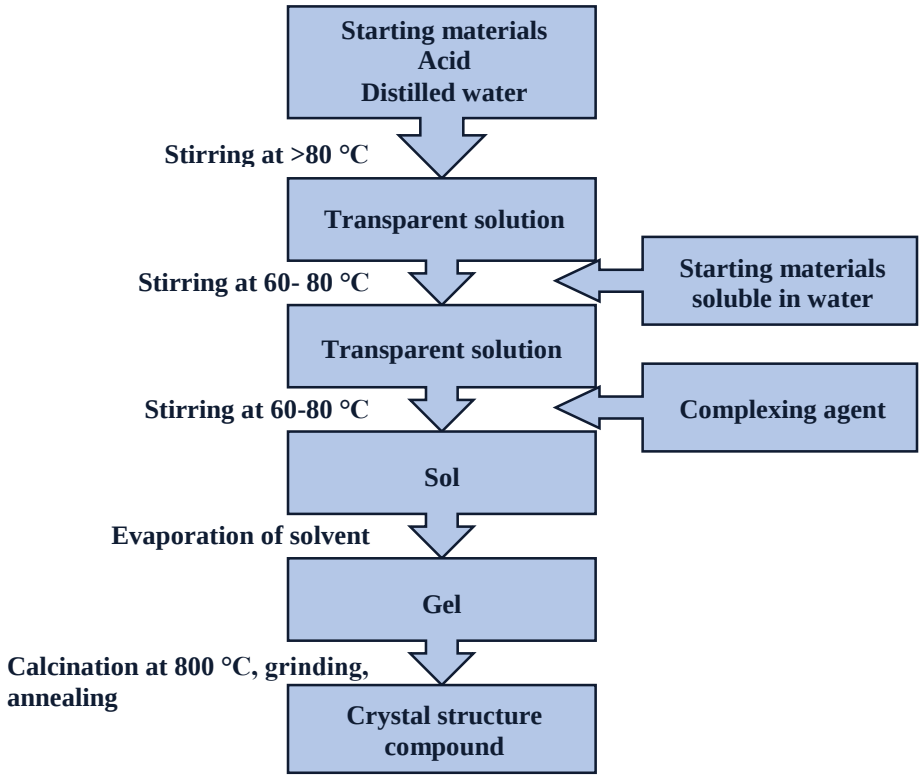

Fig. 4. Schematic representation of the steps involved in the sol-gel route.

The starting compounds (oxides) insoluble in water are dissolved in concentrated acid (acetic acid, nitric acid). The access of the acid is evaporated. To the transparent solution the starting compounds (metal acetates or nitrates) are added. The final mixed the complexing agent is put in. 1,2-ethanediol, tartaric acid, malonic acid, citric acid, oxalic acid or ethylenediaminetetraacetic acid (EDTA) is usually employed as complexing agent [34, 97]. The choice of

it affects the purity and scale of the particles of the final product. The beaker with formed sol is placed into the dryer or left on the heating plate under stirring to evaporate all the solvent. The obtained gel is dried, ground and annealed at different temperatures including intermediate pre-grinding on purpose to get well crystalized powder. The first sol-gel syntheses of YAG using a water based routes were described by Vaqueiro and Lopez-Quintela [98] and Veith et al. [99]. For the first time it was demonstrated that by alkoxide route the crystalline and single phase YAG was sintered at 700 °C which was the lowest temperature reported for the synthesis of garnets. Meanwhile, by the citrate and glycolate sol-gel process the pure polycrystalline YAG samples were obtained at 1000 °C. The mean size range of the particles made by citrate and alkoxide sol process has varied from 20 to 80 nm depending on the thermal treatment whereas the micro scale particles (grains ranging from 5 to 15 μm) have been obtained by glycolate route. In the last decays the sol-gel technique was extensively employed as synthesis route to produce the new garnet structure compounds. In the literature have been reported sol-gel synthesis of YAG:Re^{3+} (Re = Nd, Ce, Sm, Tb, Eu), lanthanide aluminium and gallium garnets (GdGG, TbAG, DyAG, HoAG, ErAG, TmAG, YbAG, LuAG and EuAG) [100-105], iron containing garnets (YIG) [106-110] and mixed-metal garnets ($Y_3(Al,Fe)_5O_{12}$, $Y_3(Al,Ga)_5O_{12}$, $Y_3(Sc,Ga)_5O_{12}$, $Y_3Sc_2Al_1Ga_2O_{12}$, $Y_3Sc_2Al_1Ga_2O_{12}$:Re^{3+} (Re = Nd, Ho, Er, Tb, Dy, Yb) and $(Y,Ln)_3(Al,Mg,Si)_5O_{12}$) [22, 25, 86, 111-118]. The main advantage of the sol-gel process is the versatility in the control of particle size, particle size distribution and arrangement of nanopores. As a result, an aqueous sol-gel process is likely to continue attracting the attention of chemists interested in designing advanced functional nanomaterials [34].

Co-precipitation method is another wet-chemistry method to produce YAG. This method is a relatively convenient and cost-effective way for powder synthesis. Precipitants such as ammonia and ammonium hydrogen carbonate are employed to produce YAG powders. Chemical precipitation can be performed by the normal-strike method (adding precipitant solution to the salt one) or by the reverse-strike technique (adding salt solution to the precipitant one). Sang *et*

al. has demonstrated that for better cation homogeneity the reverse-strike precipitation should be selected [119]. Generally, precipitation is performed on a magnetic stirrer, in an ice-cold water bath in order to maintain the temperature constant and to avoid chemical decomposition of the precipitant. The ammonium hydrogen carbonate is known to decompose between 35 and 60 °C. The initial pH of the ammonium hydrogen carbonate solution can be adjusted with an addition of nitric acid before the beginning of the precipitation. The resulting suspension after the mixing metals nitrate solution with the precipitant solution under vigorous stirring is aged for 30 min to 36 h. After being filtered, washed and dried, the precursors are calcinated at different temperatures. The pure YAG is obtained at 900-1100 °C. The 50-200 nm size particles make agglomerates [120-122]. Consequently, YAG powders synthesized via ammonia or ammonium hydrogen carbonate co-precipitation technology are preferably used to sinter transparent ceramics. Nevertheless, even starting with preformed YAG powder via co-precipitation technology, prolonged sintering at quite high temperatures, generally 1730-1790 °C, is necessary [123]. The main weaknesses of the co-precipitation route is the agglomeration problem, which takes place during the drying step and is practically difficult to completely avoid. Moreover, the intermediate phases $YAlO_3$ and $Y_4Al_2O_9$ are usually observed before the pure garnet is formed.

Hydrothermal and solvothermal syntheses are also important branches of inorganic synthesis. These routes usually are preferred in order to obtain spherical particles. Hydrothermal synthesis refers to the synthesis through chemical reactions in aqueous solution above boiling point of water and solvothermal synthesis in nonaqueous solution (ethylenediamine and etc.) relatively high temperatures. The synthesis by chemical reactions of substances in a sealed and heated aqueous solution or organic solvent occurs at 100-1000 °C temperature and 1-100 MPa pressure. Thus hydrothermal and solvothermal synthesis allow for the precise control over the size, shape distribution, and crystallinity of metaloxide nanoparticles or nanostructures. These characteristics can be altered by changing certain experimental parameters, including reaction

temperature, reaction time, solvent type, surfactant type, and precursor type [124]. In the last decays the serious of garnets were obtained using these particular methods. The hydrothermal route was employed to form 40-140 nm cubic-like YAG:Tb particles at 400 °C and 40 MPa pressure in 2003 [125] and pure micro scale YAG:Ce at 1200 °C in 2009 [126]. In 2013 Huang *et al.* has demonstrated that micro scale irregular shape YAG:Ce particles can be obtained at 360 °C and 20MPa pressure [127]. The hydrothermal synthesis of YAG can avoid the problem such as agglomeration, anyway, relatively high temperatures were required to form single phase YAG, meanwhile by solvothermal route the synthesis of spherical 60-220 nm garnets particles heated at 200-300 °C with pressure up to 10 MPa were reported in literature by Li *et al.* in 2004 [128], by Wu *et al.* in 2009 [129], by Xing *et al.* in 2010 [130] and by Park *et al.* in 2013 [131].

To conclude, the variety of the different synthesis routes allows to choose particular method to synthesize specific size, shape and homogeneous powders in order to obtain the required physical properties. Anyway, the improvement of the existing synthesis routes is still the state-of-the-art on the purpose to reduce synthesis temperature and to control more precisely the features of the final product.

1.2.2. Crystal Growth

Nowadays crystals of garnets are produced in three different forms: bulk crystals (large three dimensional crystals up to thousand cm^3), epitaxial layers (films) or two-dimensional crystals (10 Å to 500 μm thick) and fiber crystals (diameter ranging from 1 to 500 μm and length up to 1 m). The Czochralski, the Bridgman-Stockbarger, the floating zone and the flux growth-high temperature solution methods are mainly used for growing garnets bulk crystals [132].

The Czochralski method dominates in the technology of melt growth. The crystals grown by this method are obtained by dipping a seed into a melt and then lifting it up slowly. During the pulling process a given fraction of the melt is cooled and solidified. Garnets possess very high melting points, 1700±1970

°C, and for this reason the crucible has to be made of iridium, tungsten or molybdenum. During the growth process, the crystal is rotated around the vertical axis at constant speed. The exception is the formation of the conical part, if the rotation rate is accelerated in order to attend the crystal-melt interface. The crystal detached from the melt, is kept in the chamber and cooled slowly. Normally it is annealed by the heat of the crucible and sometimes by an active after heater. The separation of the crystal from the melt produces a thermal shock in the crystal, which can cause mechanical stresses and even induce cracks. Garnet crystals have very good thermoelastic parameters-high thermal conductivity and small thermal expansion, however particular care is needed if large diameter crystals are grown. The cooling rates used should be 50±150 °C h^{-1} [132]. By this method the series of crystals were synthesized. Kimura *et al.* have grown the crystals of the garnets such YAG, YGG, $Gd_3Ga_5O_{12}$, $Dy_3Ga_5O_{12}$, $Gd_3(Al,Ga)_5O_{12}$, $Dy_3(Al,Ga)_5O_{12}$, $(Gd,Y)_3Ga_5O_{12}$, $(Gd,Dy)_3Ga_5O_{12}$, $(Dy,Y)_3Ga_5O_{12}$, $(Gd,Y)_3Al_5O_{12}$, $(Gd,Dy)_3Al_5O_{12}$, $(Dy,Y)_3Al_5O_{12}$ [133]. The single crystals of neodymium, cerium, erbium or ytterbium doped yttrium aluminium garnets were investigated by Kanchanavaleerata *et al.* [134], Xiang *et al.* [135], Yu *et al.* [136] and Xu *et al.* [137], respectively.

The Bridgman-Stockbarger method, like the Czochralski method, is used for obtaining bulk crystals. The quality of these crystals is poor and usually not sufficient for technical applications. Nevertheless, because of lower costs, this method is often used in research. This method involves heating polycrystalline material above its melting point and slowly cooling it from one end of its container, where a seed crystal is located. A single crystal of the same crystallographic orientation as the seed material is grown on the seed and is progressively formed along the length of the container. The process can be carried out in a horizontal or vertical geometry. This method was successfully applied to grow YAG:Nd, YAG:Ti and LuAG:Ce crystals [138-140]. The optical quality of the crystals made by the Bridgman-Stockbarger method was comparable to that of the crystals grown by the Czochralski technique.

The crystals obtained by the floating zone method is a high-purity alternative to crystals grown by the Czochralski technique. This method is based on the zone-melting principle and was developed by Theuerer in the middle of XX century. The production takes place under vacuum or in an inert gaseous atmosphere. The process starts with two high-purity polycrystalline rods (the feed and seed rods) that are held face to face in a vertical position and are rotated into the opposite directions. With a radio frequency field or focused light of the lamps both rods are partially melted. The seed rod is brought up from below to make contact with the drop of melt formed at the tip of the feed rod. A necking process is carried out to establish a dislocation free crystal before the neck is allowed to increase in diameter to form a taper and reach the desired diameter for steady-state growth. As the molten zone is moved along the polycrystalline rod, the molten part solidifies into a single crystal. Unlike the Czochralski or Bridgman-Stockbarger growth, the molten zone is not in contact with any substances except ambient gas. Therefore, floating zone product can easily achieve much higher purity. Additionally, multiple zone refining can be performed on a rod to further reduce the impurity concentrations if the secondary phases evaporates from the melt at a fairly high rate [132]. The development of magnetic bubble devices and the application to microwave communication technology has stimulated crystal growers to seek deeper and more extensive knowledge of the growth of YIG. The floating zone method was effectively employed to grow YIG crystals by Shindo *et al.* [141], Kimura *et al.* [142] and Kita *et al.* [143]. In 1983 Balbashov *et al.* published the paper where the conditions of the growth of $Y_3(Al,Fe)_5O_{12}$, $Gd_3Fe_5O_{12}$, YGG, YAG:Nd, $Gd_3Ga_5O_{12}$, $Sm_3Ga_5O_{12}$, $Nd_3Ga_5O_{12}$ were discussed. Recently, the crystals of LuGG:Nd [144], $Y_3Sc_2Ga_3O_{12}$:Nd [145] and $Gd_3(Al,Ga)_5O_{12}$:Ce [146] were grown, meanwhile to the best our knowledge there is no data about europium, chromium, terbium or erbium doped garnets grown by the floating zone method.

In the flux growth-high temperature solution raw material is melted and then slowly cooled. The melt contains oxides (not necessarily in stoichiometric composition) of final product and a solvent (flux). Mixtures of PbO, B_2O_3 or

PbF_2 are mainly used as suitable fluxes for garnets. The growth process is carried out in a platinum crucible, inside a variable-temperature furnace. Lowering the crucible temperature causes supersaturation of the solution, followed by crystallization. The crystallization occurs on spontaneously-formed nuclei of crystallization at the crucible walls, or on a seed introduced from above (top-seed method). The seed can be replaced by a substrate plate (with a lattice parameter fitted to that of the crystal to be grown). In this case an epitaxial layer on a substrate material can be obtained and the method is practically a liquid phase epitaxy [132]. This technique was used to obtain the number of rare earth (Ce, Pr, Nd, Er, Tm and/or Yb) doped YAG films [147-151]. With the flux growth-high temperature technique all kinds of garnet can be grown, even those that face difficulties if being obtained by Czochralski technique.

1.3. Lanthanide Luminescence

The electronic configuration of each raree earth ion determines the characteristic emission properties. The energy levels of the trivalent rare earth ions which arise from the $4f^n$ configuration are given in Figure 5 [152]. In this chapter the individual luminescence properties of cerium, europium, erbium and terbium are shortly discussed.

1.3.1. Luminescence of Ce^{3+}

Cerium ions show broad band emission. In this type of emission transition an electron returns from a 5d orbital to the 4f orbital. The Ce^{3+} ion ($[Xe]4f^1$) is the simplest example, since it is a one-electron case.

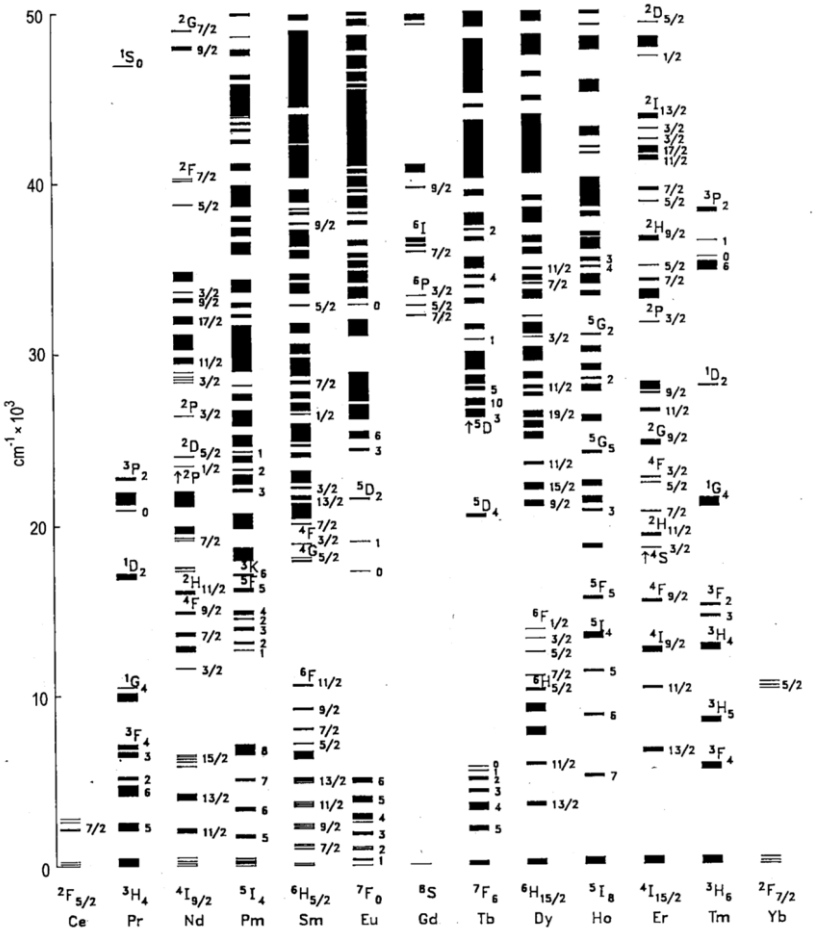

Fig. 5. Energy levels of the $4f^n$ configurations of the trivalent lanthanide ions [152].

The excited configuration is [Xe]$5d^1$. The [Xe]$4f^1$ ground state configuration yields two levels separated by ~ 2000 cm^{-1} due to spin-orbit coupling. The emission occurs from the lowest crystal field component of the [Xe]$5d^1$ configuration to the two levels of the ground state giving a double-band shape for the Ce^{3+} emission. Since the 5d → 4f transition is parity allowed and spin selection is not appropriate, the emission transition is a fully allowed one. Therefore, the decay time of the Ce^{3+} is a few ten ns. It is dependent on the emission wavelength. The longer emission wavelength, the longer decay time is gained. In general, the spectra position of the emission band depends on covalency, crystal field splitting of the $5d^1$ configuration and the Stokes shift. Usually the Ce^{3+} emission is in the ultraviolet or blue spectral region, but in YAG

it is in the green-yellow spectral region, because the crystal field in YAG is strong due to a high symmetry of the cubic lattice [5, 11].

1.3.2. Luminescence of Eu^{3+}

Upon excitation of the Eu^{3+} ([Xe]$4f^6$) ion it emits due to the $^5D_0 \rightarrow {}^7F_J$ transitions, in particular for a high doping level and/or hosts with rather high phonon frequencies, e.g. phosphates or borates. Emission lines originating from $^5D_{1,2} \rightarrow {}^7F_J$ transitions are only present if the concentration is low and the highest phonon frequency of the host is low to prevent multiphonon or cross-relaxation of the higher excited states. Generally the most intense emission lines of Eu^{3+} ions originate from the $^5D_0 \rightarrow {}^7F_{1,2,4}$ transitions, which are located in the range from 580 to 720 nm [5]. Y_2O_3:Eu^{3+}, Y_2O_2S:Eu^{3+} and (Y,Gd)BO_3:Eu^{3+} are widely used as the red component in tricolour lamps, cathode ray tubes and plasma display panels [72, 74, 153, 154]. The first two compounds exhibit dominant $^5D_0 \rightarrow {}^7F_2$ transition, meanwhile the $^5D_0 \rightarrow {}^7F_1$ transition at 595 nm becomes the most pronounced one of europium doped borate. The situation is somehow ambiguous if garnet is doped by europium. According to the paper published by Zhou *et al.* the $^5D_0 \rightarrow {}^7F_1$ transition is leading in YAG:Eu under 228 nm excitation [17], meanwhile the $^5D_0 \rightarrow {}^7F_4$ transition is the most pronounced in the emission spectra of $Ca_3Sc_2Si_3O_{12}$ garnet doped with Eu^{3+} proposed by Bettinelli et al. [155].

1.3.3. Luminescence of Tb^{3+}

The emission of the Tb^{3+} originates due to transitions $^5D_0 \rightarrow {}^7F_J$ which are mainly in the green. Often there is a considerable contribution to the emission from the higher-level emission $^5D_3 \rightarrow {}^7F_J$, mainly in the blue. Since the J values, involved in the transitions, are high, the crystal field splits the levels in many sublevels which gives the spectrum its complicated appearance. A cross-relaxation process involving two Tb^{3+} ions depopulates the $^5D_3$ level and thus reduces $^5D_3$ emission intensity. The process involves a transfer of energy from an ion in the $^5D_3$ state to a nearby ion in the ground state. The closely matched

energy difference between $^5D_4$ and $^5D_3$ levels and the $^7F_6$ and $^7F_0$ levels enables this process. In general, the observed fluorescence lines are located between 370 and 670 nm. The $^5D_4$ emission spectra typically dominates in high Tb^{3+} concentration samples. The strong $^5D_4 \rightarrow {}^7F_5$ transition produces the characteristic green colour associated with terbium [5, 156].

1.3.4. Luminescence of Er^{3+}

According to the energy level diagram (Fig. 5) there are many different possible transitions of Er^{3+} ($4f^{11}$) ions. However, Er^{3+} doped compounds are an active laser medium. These lasers find application in surgery, telecommunication, scientific research, etc. and for this reason the investigations in this ambit are continuously in progress. If the Er^{3+} ion in silica fibers are pumped with 0.98 or 1.48 μm radiation from a semiconductor laser, the $^4I_{15/2} \rightarrow {}^4I_{11/2}$ or $^4I_{13/2}$ transition occurs, respectively. The emission is given at 2.5 μm ($^4I_{11/2} \rightarrow {}^4I_{15/2}$) or 1.5 μm ($^4I_{13/2} \rightarrow {}^4I_{15/2}$) [5]. YAG:$Er^{3+}$ is probably the most active medium for laser generation at 1.6 μm. It shows absorption lines at 350 - 1800 nm. The green $^4S_{3/2} \rightarrow {}^4I_{15/2}$ emission system is of interest in order to develop compact laser devices for data storage and display applications. The $^4I_{13/2} \rightarrow {}^4I_{15/2}$ emission transition consists of a relatively broad system extending from 1470 to 1700 nm, and it is the most interesting for telecommunication and medicine. The luminescence properties of erbium doped compounds highly depend on the dopant concentration and matrix itself [157].

1.4. Luminescence of Cr^{3+}

The luminescence of Cr^{3+} (d^3) in Al_2O_3 (ruby) formed the basis on the first solid state laser in 1960. This emission of chromium doped aluminium oxide consists of two sharp lines contributed to ^2E-$^4A_2$ transition in the far red. In general, the emission of transition metal ions originates from the lowest excited state with the life time of some ms. Not always the ^2E level is the lowest excited state for Cr^{3+}. For the relatively low crystal fields the $^4T_2$ level is lower. In this case the emission is changed to broad-band $^4T_2$-$^4A_2$ transitions in the infrared

with a decay of ~ 100 μs. Garnet phosphors doped with chromium exhibit luminescence in the red and far-red region depending on crystal field. If the crystal field is strong like in YAG, luminescence occurs due to the $^2E \rightarrow {}^4A_2$ transition, which peaks at around 700 nm and is relatively narrow [12]. Substituting Al with Ga results in a weaker crystal field and in this case luminescence occurs due to the $^4T_2 \rightarrow {}^4A_2$ transition, which is characterized by a broad band peaking at around 720 nm [12, 13].

2. EXPERIMENTAL PART

2.1. Synthesis Methods

All garnet powder samples were synthesized by glycolic or citric sol-gel processing routes. The solid-state reaction was used to obtain precursor powders for crystal growth by the traveling solvent floating zone method.

2.1.1. Sol-Gel Method

The Y-Al-M-O (M = Ga, In, Cr, Mn, Fe, Co, Ni or Cu), Y-Ga-In-O, Lu-Al-Ga-O, Lu-Y-Gd-Al-O or Y-Fe-Co-O precursor gels were prepared by using stoichiometric amounts of analytical grade appropriate metal oxides, nitrates or acetates as starting materials. In the sol-gel process metal oxides were first dissolved in small amount of diluted CH_3COOH or concentrated HNO_3 under heating and stirring in a beaker covered with a watch glass. In the case of using acetic acid, the mixture was stirred till the clear solution was obtained. If the nitric acid was used, after a clear solution was obtained the excess of HNO_3 was evaporated and the metal nitrates were washed twice by pouring and evaporating a little amount of distilled water. Finally, 25 mL of distilled water were added. Next, to the obtained clear solution the metal nitrates or acetates dissolved in 50 mL of distilled water were added and the resulting mixture was stirred for 2 h at 60-70 °C. Then complexing agent (1,2-ethanediol or citric acid) was added with the molar ratio of ~ 1:2 to all metal ions. After 2 h the clear solution was concentrated by evaporation at ~ 80 °C under stirring or left in the oven over night at 150 °C. The obtained brownish sponge-like gel was crushed and ground to fine powders in an agate mortar. Then the powders were first annealed at 800-1000 °C for 2 h in air. After intermediate grinding the powders were heated at 1000-1500 °C for 4-10 h in air for improvement of crystallinity.

2.1.2. Traveling Solvent Floating Zone Method

The europium doped precursor powders for YAG, YGG or $Y_3In_{0.5}Al_{4.5}O_{12}$ were prepared from stoichiometric mixtures of appropriate metal oxides. These

oxides were accurately weighed and adequately mixed. The concentration of Eu in the starting material was 5 or 30 at%. The mixture was annealed at 1000 °C for 20 h and then sintered at 1500-1550 °C for 40-60 h in order to complete the solid-state chemical reaction. After that the polycrystalline material was ground and loaded into a rubber membrane to fabricate the feed and seed rods. The rods were hydrostatically pressed to about 40 MPa. The obtained rods had a diameter of 5-8 mm and a length of 60-100 mm and were sintered at 1500 °C for 20 h in air. The crystal was grown in an optical floating-zone furnace (Crystal Systems Inc., FZ-T-10000-H-VI-VP-PC) equipped with four 1 kW Halogen lamps reaching a maximum temperature of 2200 °C. The bulk crystals were grown in nitrogen, oxygen or a mixed nitrogen/oxygen atmosphere (Fig. 6).

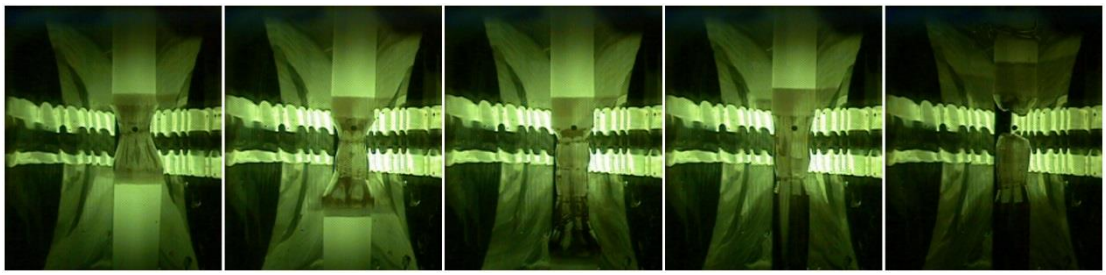

Fig. 6. YAG:5%Eu^{3+} crystal growth in an optical floating zone furnace in argon atmosphere.

The gas flux was 250 or 50 mL/min. The growth rate was in the range 15-20 mm/h and typical rotation rates of the feed rod and seed rod were 20 rpm in opposite directions, respectively. Once the melting zone was stabilized in the growth process, the growth temperature was controlled by maintaining the lamp power in the range of 72.5-81.8 %. After the growth, the crystal was cooled down to room temperature from the melting temperature of YAG:Eu^{3+}, YGG:Eu^{3+} or $Y_3In_{0.5}Al_{4.5}O_{12}$:$Eu^{3+}$ in 1 h. To release the thermal stress formed in the growth process, the as-grown crystal was annealed according to the following procedure: the crystal was put into an annealing furnace, heated to 1200 °C in air at a rate of 100 °C/h and maintained at that temperature for 15-60 h. Then it was cooled down to room temperature at a rate of 30 °C/h [144].

2.2. Chemicals

The starting materials were Y_2O_3 (99.99% Treibacher), $Al(NO_3)_3 \cdot 9H_2O$ (≥98% Sigma-Aldrich), Al_2O_3 (99.99%, Sigma-Aldrich), $Ga(NO_3)_3 \cdot 6H_2O$ (≥99.9% Alfa Aesar) or Ga_2O_3 (99.999%, Alfa Aeser), In_2O_3 (99.9% Alfa Aesar), Gd_2O_3 (99.99% Treibacher), Lu_2O_3 (99.99% Treibacher), Fe_2O_3 (>99% Merck), $Fe(NO_3)_3 \cdot 9H_2O$ (p. a. Alfa Aeser), $Cr(NO_3)_3 \cdot 9H_2O$ (99% Aldrich), $Cu(CH_3COO)_2 \cdot H_2O$ (p. a. Sigma-Aldrich), $Mn(CH_3COO)_2 \cdot 4H_2O$ (p. a. Lach-Ner), $Ni(CH_3COO)_2 \cdot 4H_2O$ (p. a. Aldrich) $Co(NO_3)_2 \cdot 6H_2O$ (97.7% Alfa-Aesar), $Ce(NO_3)_3 \cdot 4H_2O$ (99.9% ChemPur), Eu_2O_3 (99.99% Treibacher), Er_2O_3 (99.99%% Treibacher) Tb_4O_7 (99.99% Alfa-Aesar), $Mg(NO_3)_2 \cdot 6H_2O$ (≥98% Sigma-Aldrich), $C_6H_8O_7$ (citric acid; GPP Reactupur VNR) and $HOCH_2CH_2OH$ (100% BDH Prolabo).

2.3. Materials Characterization

2.3.1. X-ray Powder Diffraction

The synthesized samples were characterized by XRD performed with a Siemens D-5000 powder diffractometer equipped with a conventional X-ray tubes (Cu $K_{\alpha 1}$ radiation (λ = 1.54060 Å); a Stoe-Cie transmission diffractometer STADI P operating with a Ge monochromatized Co radiation (λ = 1.788965 nm) and equipped with a PSD detector; a Siemens D-5005 or D8 Bruker AXC diffractometers (CuK_{a1} radiation) or with Ni-filtered Cu K_α radiation on Rigaku MiniFlex II diffractometer working in Bragg-Brentano ($\theta/2\theta$) geometry.

Variable temperature XRD was measured on a PANalytical-HT-XRD. HT powder diffraction was performed in high-temperature XRD cell (Anton Paar HTK 16) with a thin layer of sample deposited as ethanol suspension on the platinum sample holder in the PANalytical X'Pert PRO diffractometer, equipped with CoKα tube (40 kV, 30 mA) and X'Celerator detector. Diffraction data were taken from ambient temperature to 700 ºC in 100 ºC steps and from 700 ºC to 1000 ºC in 25 ºC steps. The sample temperature was held constant during 30 minute data collection and raised at 1 ºC min^{-1} between measurements.

2.3.2. Laue XRD

The Laue method was used to determine orientation and quality of single crystals. White (polychromatic) X-ray radiation was transmitted through a crystal. Each set of planes in the crystal structure diffracted the particular wavelength from the white radiation that satisfied the Bragg law. The diffracted beams form arrays of spots recorded by the CCD camera.

2.3.3. X-ray Fluorescence

X-ray fluorescence is an elemental analysis technique. Orbis Micro X-ray Fluorescence Analyzer (Orbis, EDAX) uses X-ray excitation to induce element specific characteristic X-ray fluorescence emission for the elemental analysis. The method allowed examination of large sample areas with resolution of 30 μm which was a spot of the focused primary X-ray beam.

2.3.4. High-Resolution Neutron Powder Diffraction

The High-Resolution Powder Diffractometer for Thermal Neutrons (HRPT at the Swiss Spallation Neutron Source (SINQ), PSI) was used to collect neutron diffraction data. The multidetector diffractometer HRPT is designed as flexible instrument for efficient neutron powder diffraction studies-also for small sample sizes. High resolution is achieved by thermal neutrons, large scattering angles of the monochromator and of the sample (up to 165°). 1.49375 Å and 1.88570 Å neutron wavelengths were used for the measurements. The data was collected at room temperature.

2.3.5. SEM Analysis

SEM images were taken by FE-SEM Zeiss Ultra 55 (Limited Edition), EVO 50 XVP (Carl Zeiss SMT AG) or a FE-SEM Hitachi SU-70 scanning electron microscopes for morphological surface studies.

2.3.6. VUV Spectroscopic Investigations

The VUV spectrometer (Edinburgh Instruments FS920) was used for exciting phosphor samples. The spectrometer was equipped with VUV monochromator VM504 from Acton Research Corporation (ARC) and deuterium lamp as an excitation source. Sample chamber was flushed with dried nitrogen in order to prevent absorption of VUV by water and oxygen. Excitation (excitation slit 1 mm, emission slit 2 nm) and emission (excitation slit 2 mm, emission slit 1 nm) spectra were recorded in the ranges of 150-375 nm and 200-800 nm, respectively. The emission spectra were corrected by correction file obtained from tungsten incandescent lamp certified by the NPL (National Physical Laboratory, UK). The relative VUV excitation intensities of the samples were corrected by dividing the measured excitation spectra of the samples with the excitation spectrum of sodium salicylate (o-$C_6H_4OHCOONa$) taken under the same excitation conditions. During the measurements of entire emission spectra and excitation spectra in the range of 150-220 nm the sample chamber was flushed with dried nitrogen in order to avoid absorption of VUV radiation by oxygen and moisture.

2.3.7. UV/VIS Spectroscopic Investigations

Reflection spectra in the UV/VIS range were recorded on Edinburgh Instruments FS920 spectrometer equipped with a 450 W Xe arc lamp, a cooled (-20 °C) single-photon counting photomultiplier (Hamamatsu R928) and an integration sphere coated with barium sulphate. $BaSO_4$ (99% Sigma-Aldrich) was used as a reflectance standard.

Excitation and emission spectra in the UV/VIS range were recorded on Edinburgh Instruments FLS920 spectrometer equipped with a 450 W Xe arc lamp, mirror optics for powder samples and a cooled (-20 °C) single-photon counting photomultiplier (Hamamatsu R2658P). The photoluminescence emission spectra were corrected by correction file obtained from tungsten incandescent lamp certified by the NPL.

2.3.8. Structure Refinement

The crystal structure of heated at elevated temperatures the Y-Eu-Al-Ga-O, Y-Eu-Al-In-O, Y-Eu-Ga-In-O and Y-Al-Fe-O systems was refined by the Rietveld profile method with the use of the program Fullprof. The nuclear reflections were indexed for $(Y,Eu)_3(Al,Ga)_5O_{12}$, $(Y,Eu)_3(Al,In)_5O_{12}$ and $(Y,Eu)_3(Ga,In)_5O_{12}$, while the crystal and magnetic structures were refined for $Y_3(Al,Fe)_5O_{12}$. From consideration of the effective ionic radii [48], it was considered that Y^{3+} and Eu^{3+} occupy only the dodecahedral site and Al^{3+}, Ga^{3+} and Fe^{3+} occupy both the octahedral and the tetrahedral sites. The occupancy of the dodecahedral site was therefore fixed at unity, and the occupancies of the octahedral and tetrahedral sites were constrained to maintain the chemical composition of each specimen.

2.3.9. LE Calculations

The luminous efficacy (LE), in lumen per watt optical, is a parameter describing how bright the radiation is perceived by the average human eye. It scales with the protopic human eye sensitivity curve *V(λ)* and can be calculated from the emission spectrum *I(λ)* of the sample as [158]:

$$LE(lm/W) = 683\ (lm/W) \times \frac{\int_{360nm}^{830nm} I(\lambda)V(\lambda)d\lambda}{\int_{360nm}^{830nm} I(\lambda)d\lambda} \qquad \text{(Eq. 1.)}$$

3. RESULTS AND DISCUSSIONS

3.1. Limitary Radius of Mixed-Metal Garnets

Limitary radius is the average of ionic radius of the cations distributed among the tetrahedral and octahedral sites in the crystal lattice at which the garnet structure starts to decompose. In the first part of experimental investigations, to obtain crystalline garnets the Y-A-B-O (A = Al, Ga or Fe; B = Cr, Mn, Co, Ni, Cu or In) precursor gels were calcined at 800 °C and sintered at 1000 °C in air.

3.1.1. Phase evaluation of $Y_3Al_{5-x}In_xO_{12}$ and $Y_3Ga_{5-x}In_xO_{12}$

The X-ray diffraction patterns for the non-substituted YAG and YInG samples are shown in Figure 7.

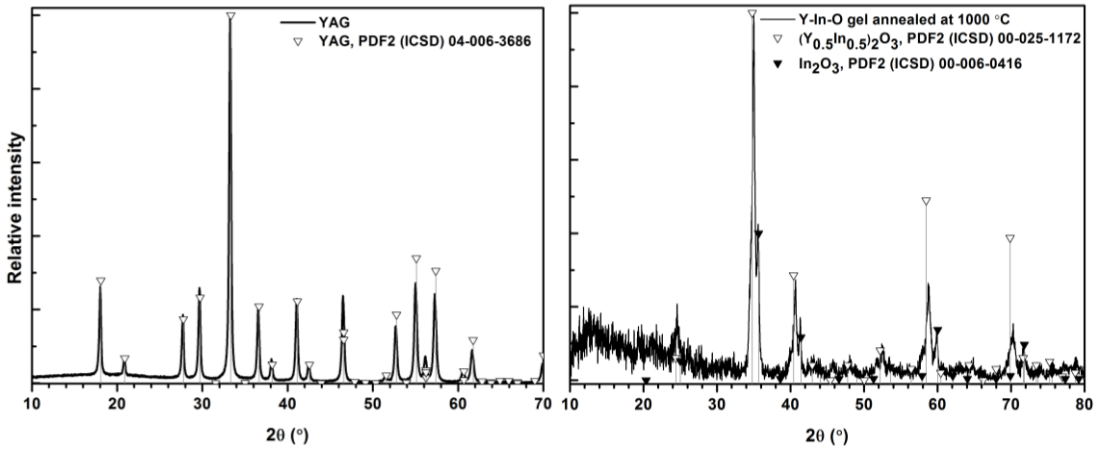

Fig. 7. XRD patterns of Y-Al-O (left) and Y-In-O (right) acetate-nitrate-glycolate gels annealed at 1000 °C.

As seen, sintering of Y-Al-O gel at 1000 °C produced single-phase YAG. Sintering at 1000 °C of Y-In-O gel, however, produced the mixture of indium-yttrium oxide and indium oxide ($(Y_{0.5}In_{0.5})_2O_3$ (PDF2 (ICSD) 00-025-1172) and In_2O_3 (PDF2 (ICSD) 00-006-0416), respectively) and no traces of $Y_3In_5O_{12}$ have formed. The peaks of indium-yttrium oxide do not perfectly match the intensities of the peaks of recorded diffraction pattern indicating that probably indium and yttrium ratio is not exactly 1:1 in the compound.

Next, the same aqueous sol-gel synthesis method has been applied for the preparation of mixed-metal garnets $Y_3(Al,In)_5O_{12}$ obtained by substituting part of aluminium by indium. The XRD patters of synthesized samples with different nominal compositions of $Y_3Al_{5-x}In_xO_{12}$ (x = 0.75, 1.0, 1.25, 1.5, 1.75, 2.0, 2.5, 3.0, 3.5, 4.0, 4.5 and 5.0) are shown in Figure 8.

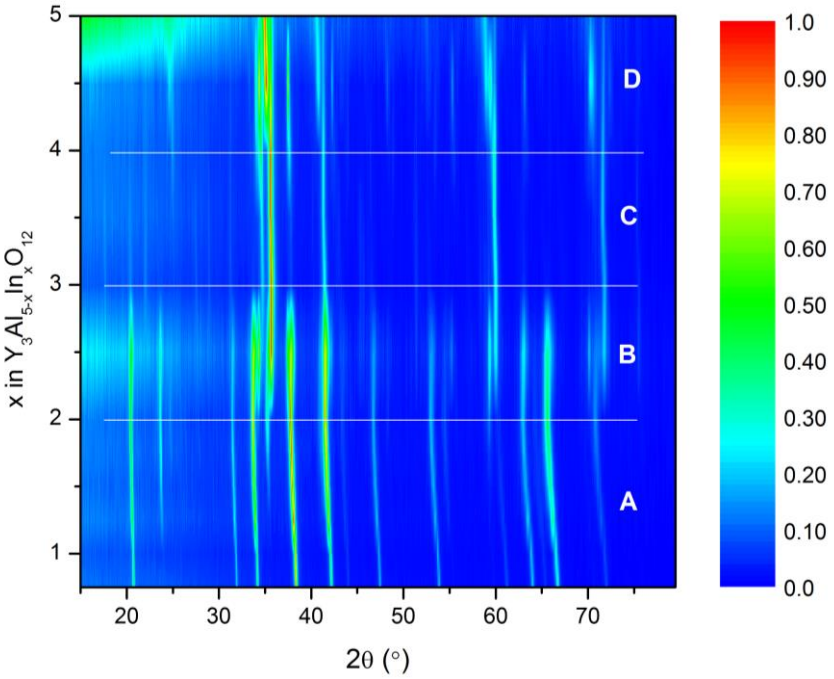

Fig. 8. XRD patterns of $Y_3Al_{5-x}In_xO_{12}$ with different indium content.

All diffraction patterns can be separated into four domains (marked as A-D). In the domain A ($0.75 \leq x < 2.0$) the peaks are attributed to cubic garnet phase. The peaks attributed to garnet phase are gradually shifted to the left if indium content is increased indicating that the crystal lattice is slightly enhanced. These results are in good agreement with limiting radius theory, which states that indium ion is too large for the tetrahedral site. The shift of peaks is observed until indium content becomes two (indium ions occupy all octahedral sites). Afterwards the shift of the peaks ends. Moreover, the characteristic reflections of garnet phase starts to vanish from the XRD pattern of $Y_3Al_{3.25}In_{1.75}O_{12}$. The ionic radius of indium could be the main reason of this observation. If all octahedral sites are occupied (x exceeds the value 2) the garnet structure compound starts to decompose. The formation of mixed $Y_3(Al,In)_5O_{12}$ garnets is problematic also at lower substitutional level of indium. With increasing

amount of indium in the composition of $Y_3(Al,In)_5O_{12}$ (In > 1.25) the peaks observed at 23.8° and 36.0° attributable to the impurity phases already are seen. Thus, it can be concluded that for the system of $Y_3(Al,In)_5O_{12}$ the limiting content of indium is $1.75 \leq x \leq 2$.

In the domain B ($2 < x < 3$) the peaks attributed to In_2O_3 (PDF2 (ICSD) 00-006-0416) and $Al_2Y_4O_9$ (PDF2 (ICSD) 00-034-368) appear, while in the domain C ($3 < x < 4$) these phases become the pre-dominant phases and the garnet phase is not formed anymore. Finally, in the domain D ($4 < x < 5$) the multi-phases product turns to the mixture of $(Y_{0.5}In_{0.5})_2O_3$ (PDF (ICSD) 00-025-1172) and In_2O_3 (PDF (ICSD) 00-006-0416) if all aluminium is changed by indium.

To check the exact temperature for the formation of mixed-metal garnet, the Y-Al-In-O precursor gel with the composition of $Y_3Al_4In_1O_{12}$ was chosen. The gradual formation of the $Y_3Al_4In_1O_{12}$ phase is shown in Figure 9.

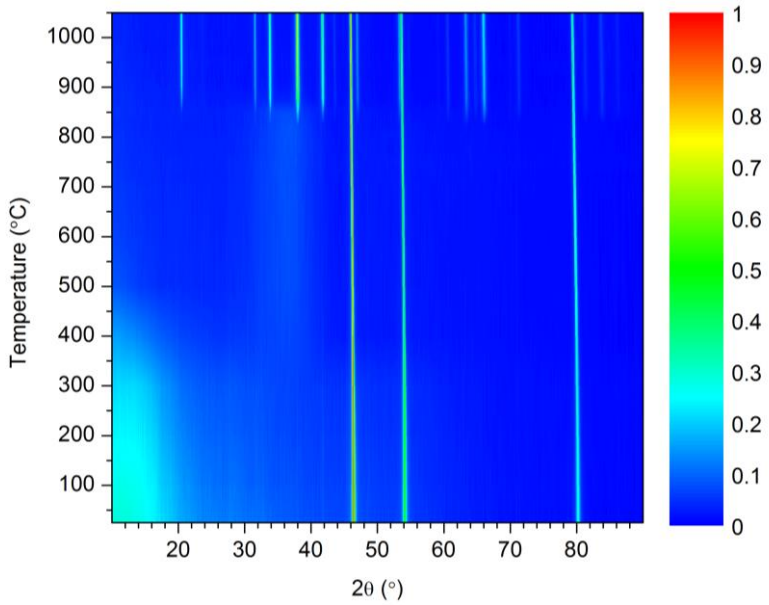

Fig. 9. XRD of $Y_3Al_4In_1O_{12}$ synthesized at different temperatures.

In all patterns three the most intensive lines of Pt sample holder at 46.4°, 54.1° and 80.2° are observed. The appearance of characteristic lines for garnet at 33.8°, 22.8°, 41.7°, 20.5° and etc. shows that the formation of garnet phase starts already at ca 850 °C. According to XRD data the variation of temperature

from 850 °C to 1050 °C does not influence the phase composition of the end products, though the crystallinity is improved.

The investigation of the limitary radius of Y-Ga-In-O precursor gels sintered at 1000 °C for 10 h in air has shown rather similar results. The diffraction patterns of $Y_3Ga_{5-x}In_xO_{12}$ (x = 1.25, 1.5, 1.75, 2.0, 2.25, 2.5, 3.0 and 3.5) are given in Figure 10.

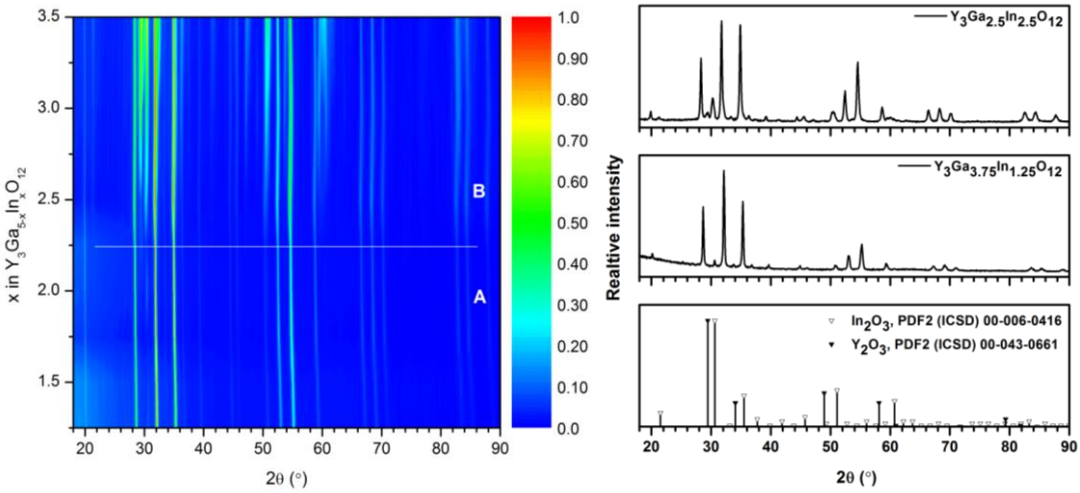

Fig. 10. XRD patterns of $Y_3Ga_{5-x}In_xO_{12}$ with different indium content.

If indium content is 1.25, the observed peaks are attributed to cubic garnet structure. However, the evidence of impurity phase of In_2O_3 30.31° (PDF2 (ICSD) 00-006-0416) is monitored in each sample even with narrow substitutional range of indium. This peak increases and extra peaks at 21.25°, 35.33°, 60.33° and etc. attributed to In_2O_3 appear if indium is increased from 2.25 to 3.5. Moreover, if $x \geq 2.25$ in $Y_3Ga_{5-x}In_xO_{12}$, the peaks of Y_2O_3 at 29.42°, 32.27°, 61.50° and etc. arise indicating the limit of indium is exceeded in Y-Ga-In-O system (B domain in Fig. 10). Therefore, for the system of $Y_3(Ga,In)_5O_{12}$ the mean cationic radius at which still formation of garnet phase occurs seems to be in the range of 0.696-0.706 Å which corresponds to the chemical compositions of $Y_3Ga_3In_2O_{12}$ and $Y_3Ga_{3.75}In_{2.25}O_{12}$, respectively.

A closer look to the positions of three the most intensive garnet phase peaks at 28-36° is demonstrated in Figure 11. The shift of Y-Ga-In-O system peaks is

not so expressed as in Y-Al-In-O system because the ionic radius of gallium is closer to indium than aluminium (Table 2).

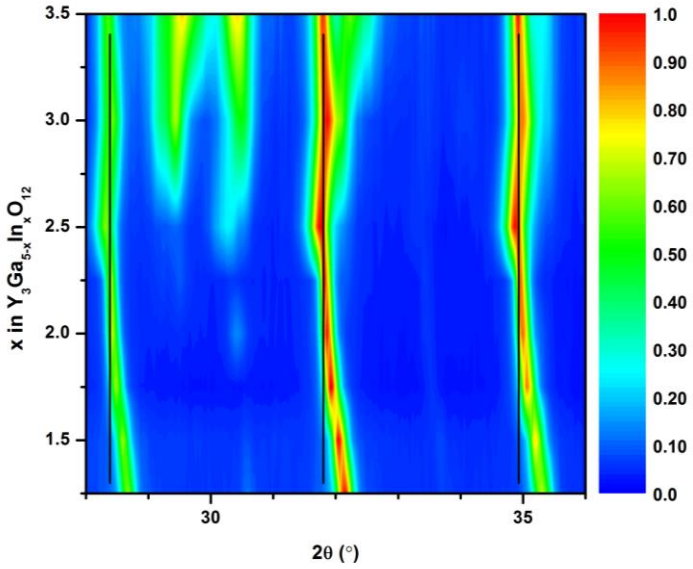

Fig. 11. A closer look to the positions of three the most intensive garnet phase peaks at 28-36°.

Three black lines at the positions 28.4°, 31.8° and 34.9° are placed in the graph for better visualisation of the shift which vanishes in the $2 < x < 2.25$ range. This implies that probably some indium ions occupy tetrahedral sites contrary to the limiting radius rules. Nevertheless, an extra experimental analysis or Rietveld method investigation is needed to discuss in more details this open question.

3.1.2. Phase evaluation of $Y_3A_{5-x}B_xO_{12}$ (A = Al or Fe; B = Cr, Mn, Co, Ni or Cu)

X-ray diffraction patterns of the Y-Al-Cr-O precursor gels sintered at 1000 °C with the different molar part of chromium are shown in Figure 12A. The single phase product is obtained only within the narrow substitution range. If x = 1.25 $Y_3Al_{5-x}Cr_xO_{12}$, the XRD pattern of $Y_3(Al,Cr)_5O_{12}$ is analogous to the XRD pattern of YAG (PDF2 (ICSD) 00-033-0040). All high intensity peaks could be attributed to characteristic cubic garnet lattice. However, since the most intensive peaks of $Y_3Al_{5-x}Cr_xO_{12}$ (2θ = ~33.3°) and $YCrO_3$ (2θ = 33.5°) almost

overlap, it is very difficult to identify precisely and correctly the beginning of the appearance of the $YCrO_3$ phase which the most intensive peak clearly appears only if x = 1.75. With increasing of the molar part of chromium (x = 2.75), the garnet structure compound phase still remains, but also the perovskite yttrium chromate phase becomes the dominant. The side phase peaks are marked with the solid triangular (PDF2 (ICSD) 00-034-0365). The deeper analysis lets to presume, that the decomposition of $Y_3(Al,Cr)_5O_{12}$ starts with the lower molar part of chromium in the structure. The beginning of the appearance of the main peak of $YCrO_3$ phase could be associated with the increase of asymmetry of the most intensive $Y_3Al_{5-x}Cr_xO_{12}$ reflection if x = 1.25. The beginning of the decomposition of $Y_3(Al,Cr)_5O_{12}$ is coherent to the appearance of the extraneous phase. This is sufficiently evident if the peak area in the XRD pattern is enlarged. Therefore, the range of $1.00 < x < 1.25$ could be a limit of the introduced amount of chromium in $Y_3Al_{5-x}Cr_xO_{12}$.

Figure 12B shows the XRD patterns of manganese substituted YAG. According to the results presented in the XRD pattern, the phase composition of the synthesized products varies with increasing the amount of manganese in $Y_3Al_{5-x}Mn_xO_{12}$. If x = 1.00 the single phase garnet of composition $Y_3Al_4Mn_1O_{12}$ was obtained. All peaks are characteristic to the cubic lattice of YAG. If x = 1.25 in $Y_3Al_{5-x}Mn_xO_{12}$, the $Y_3(Al,Mn)_5O_{12}$ is still the major phase. However, few peaks characteristic to the yttrium dimanganate phase (YMn_2O_5) (signed with solid triangular) are also observed at 24.4°, 29.1°, 31.0°, 34.0°, 35.5° (PDF2 (ICSD) 00-034-0667). If the molar part of manganese is enhanced, the intensity of these peaks is also increased. The appearance of impurity phase alerts about the limit of manganese instead of aluminium, therefore the range of $1.00 < x < 1.25$ could be attributed to the limit of manganese in $Y_3Al_{5-x}Mn_xO_{12}$.

The analysis of Figure 12C has assisted to determine the limit of the molar part of cobalt in $Y_3Al_{5-x}Co_xO_{12}$. It shows that pure garnet structure material is obtained only within narrow substitutional range of cobalt. Again, if x = 0.25 in $Y_3Al_{5-x}Co_xO_{12}$, all reflections in the XRD pattern are attributed to the garnet phase. With increasing the molar part of cobalt to x = 1.00 the new peaks

attributable to the side crystalline phases appear. The peaks at 24.0°, 34.2° and 42.6° (signed with the solid triangular) are attributed to the perovskite yttrium aluminate (YAP, (PDF2 (ICSD) 00-033-0041)).

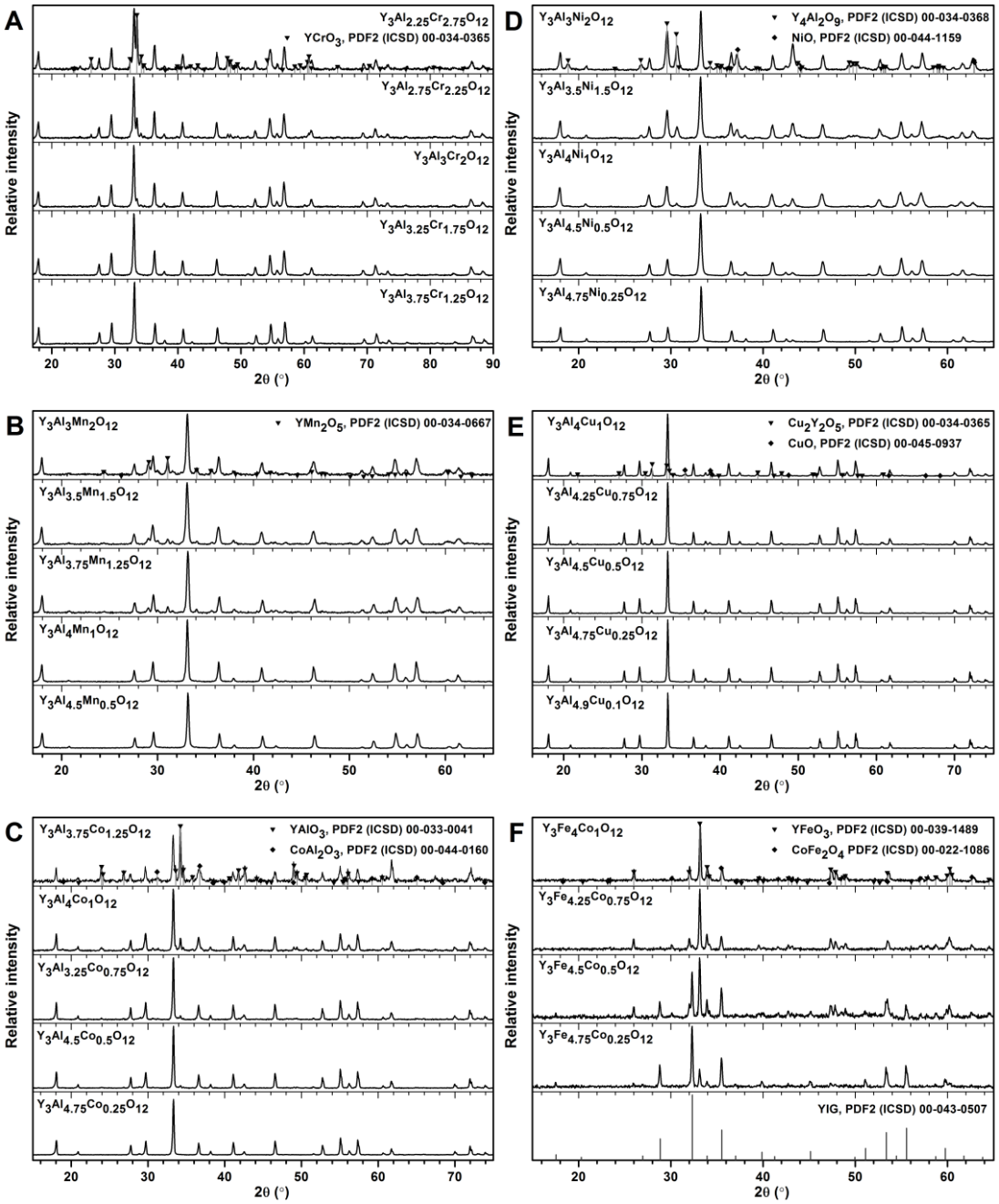

Fig. 12. XRD patterns of $Y_3A_{5-x}B_xO_{12}$ (A = Al or Fe; B = Cr, Mn, Co, Ni or Cu) with different x content.

The intensity of these peaks increases with enhanced amount of cobalt. Moreover, the new additional peaks of YAP are observed at 26.9°, 34.6°, 41.8°

and etc. Finally, if x = 1.25 the major phase becomes YAP instead of $Y_3(Al,Co)_5O_{12}$. The formation of second extraneous phase is also determined. The peaks signed with the solid rhomb at 31.3°, 36.8°, 44.8°, 65.2° and etc. belongs to the spinel structure cobalt aluminate (PDF2 (ICSD) 00-038-0814). To conclude, the most intensive peak of the side phase of YAP at 34.2° appears if x = 0.50 and gradually increases. Thus, the range $0.25 < x < 0.50$ could be attributed to the limit of cobalt in $Y_3Al_{5-x}Co_xO_{12}$.

The XRD patterns of $Y_3Al_{5-x}Ni_xO_{12}$ samples are presented in Figure 12D. The peaks of major phase $Y_3(Al,Ni)_5O_{12}$ are analogous to the XRD pattern of YAG. The minor amount of nickel oxide NiO (PDF2 (ICSD) 00-044-1159) is formed already if x = 0.25 (characteristic peaks of NiO are signed with the solid rhomb in Figure 12D). Again, the intensity of these peaks increases with increasing the nickel content in the precursor. New reflections characteristic to yttrium metaaluminate $Y_4Al_2O_9$ also appear at 18.9°, 26.8°, 29.6°, 30.6°, 34.3°, 35.0°, 43.8° and etc. (PDF2 (ICSD) 00-034-0368, signed with the solid triangular) if $x \geq 1$. The most intensive (-122) peak of $Y_4Al_2O_9$ at 29.6° overlaps with the (400) peak of $Y_3(Al,Ni)_5O_{12}$ at ~29.8°, therefore it is difficult accurately to determine the presence point of impurity phase. The second most intensive (112) peak of $Y_4Al_2O_9$ at 30.6° appears if $x \geq 1$ indicating the decomposition of garnet structure. Therefore the $0.5 < x < 1$ range could be attributed to the limit of nickel in $Y_3Al_{5-x}Ni_xO_{12}$.

The single-phase garnet structure compound is obtained only within extremely narrow substitutional range of copper in $Y_3Al_{5-x}Cu_xO_{12}$ (Figure 12E). If x = 0.10 each peak in the XRD pattern of $Y_3Al_{4.9}Cu_{0.1}O_{12}$ is analogous to that of YAG (PDF2 (ICSD) 00-040-0033). With the slight increase of the copper (x = 0.25) in addition to the main phase the minor amount of impurity phases of yttrium cuprate ($Y_2Cu_2O_5$) and copper (II) oxide (CuO) has formed (PDF2 (ICSD) 00-033-0511 and PDF2 (ICSD) 00-045-0937, respectively). The peaks of $Y_2Cu_2O_5$ at 31.3°, 39.8° and etc. are signed with the solid triangular, while the solid rhomb is the character for the CuO (the peaks at 35.5°, 38.8° and etc.). As in all cases, the intensity of peaks characteristic to extraneous phases increase

with increasing the content of copper. The appearance of impurity phases suggests that the garnet structure starts to decompose. Thus, the range of $0.10 < Cu < 0.25$ could be attributed to the limit of copper in $Y_3Al_{5-x}Cu_xO_{12}$.

By introducing a small amount of cobalt instead of iron into yttrium-iron garnet pure yttrium-iron-cobalt garnet was obtained along with the impurity phases (Figure 12F). Three different phases were identified even if the content of cobalt is $x = 0.25$ in $Y_3Fe_{5-x}Co_xO_{12}$. The peaks of major phase are analogous to the XRD pattern of YIG (PDF2 (ICSD) 00-043-0507). The peaks signed with solid triangular are attributed to perovskite yttrium ferrite ($YFeO_3$, PDF2 (ICSD) 00-039-1489) and the peaks signed with solid rhomb are characteristic of spinel cobalt ferrite ($CoFe_2O_4$, PDF2 00-022-1086). Figure 12F shows that the garnet structure phase completely disappears if the content of cobalt is $x \geq 0.75$.

3.1.3. Morphology of products

The morphology of the $Y_3A_{5-x}B_xO_{12}$ (A = Al, Ga or Fe; B = Cr, Mn, Co, Ni, Cu or In) powders was inspected by taking SEM pictures. The representation of images is rather similar. Therefore, only the pictures of $Y_3Ga_{3.75}In_{1.25}O_{12}$ and $Y_3Ga_3In_2O_{12}$ are chosen to represent in Figure 13.

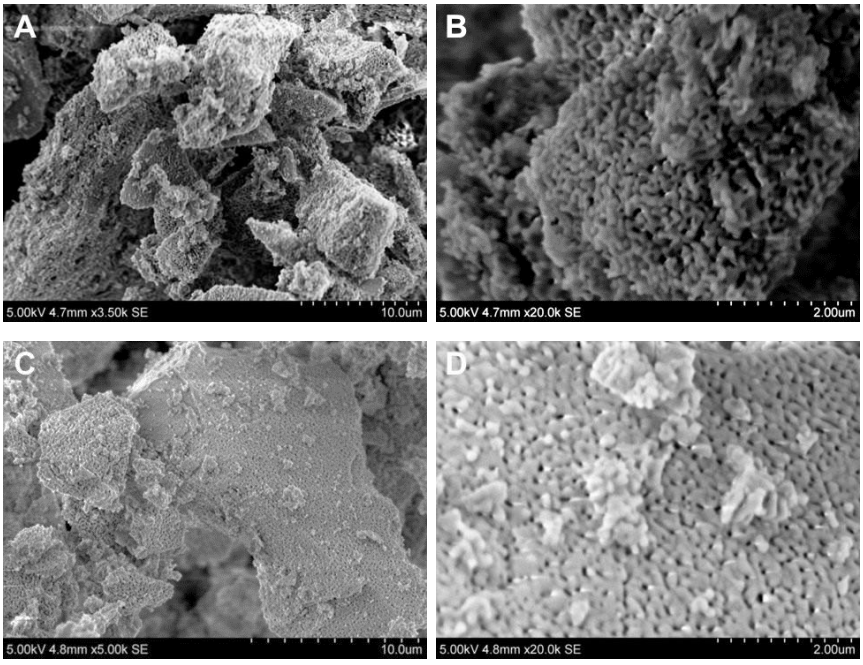

Fig. 13. SEM images of $Y_3Ga_{3.75}In_{1.25}O_{12}$ (A), (B) and $Y_3Ga_3In_2O_{12}$ (C), (D) obtained under different magnification.

The scanning electron micrographs consist of ~200 nm sized oval particles forming ~1-50 μm sized porous agglomerates. The plate-like agglomerated particles are irregular shaped. The powders made by sol-gel method has unique the particular shape and size, because under the high temperature, the relatively high surface of nanosheets may cause them to partly melted and the surface tension results in the sphere-like morphology. The partly melted particles become cross-linked [159]. However, no significant differences were observed in the SEM pictures for the samples with different content of indium. Finally, the main morphological features are the same for all synthesized samples, i. e. are independent on the nature of the substituent B (B = Cr, Mn, Co, Ni, Cu or In) in $Y_3A_{5-x}B_xO_{12}$.

3.1.4. Limitary radius of $Y_3A_{5-x}B_xO_{12}$ (A = Al, Ga or Fe; B = Cr, Mn, Co, Ni, Cu or In)

According to experimental results the limitary radius of any $Y_3A_{5-x}B_xO_{12}$ garnet can be calculated by Equation (2):

$$R_{A,B}^{x} = \frac{(5-x)\times R_A + x\times R_B}{5} \qquad (2)$$

R_A and R_B are the average of ionic radius. If it is assumed that R_A and R_B may occupy either octahedral either tetrahedral sites, according to the notation proposed by Gilleo & Geller in 1959 [28, 160], the chemical formula of the $Y_3A_{5-x}B_xO_{12}$ system can be generally expressed as

$$\{Y\}_3[A_{1-p}B_p]_2(A_{(3-x+2p/3}B_{(x-2p)/3})_3O_{12}$$

where p and x refer the occupancy parameter of B^{3+} in the six-coordinated site and the composition for the specimens, respectively. Thus, the Equation (2) is modified to the Equation (3):

$$R_{A^iB^{ii}}^{x,p} = \frac{2(1-p)R_{A_{oct.}} + 2pR_{B_{oct.}} + (3-x+2p)R_{A_{tetr.}} + (x-2p)R_{B_{tetr.}}}{5} \qquad (3)$$

The ionic radii values for the calculation of the limitary radius are taken from the Table 2. The obtained results are presented in Table 3. The first column gives the limit range of ion B^{3+}. The second column presents the calculated value of $R_{A,B}^{x}$ by using Equation 2. The results of limiting ionic radius calculated by using Equation 3 are presented in the third column. For this calculation it was assumed that all B^{3+} ions preferably occupy octahedral site.

Table 3. Calculated limitary radius for $Y_3Al_{5-x}B_xO_{12}$ (B = In, Cr, Mn, Co, Ni) and $Y_3Ga_{5-x}In_xO_{12}$.

The limit range of B^{3+}	$R_{A,B}^{x}$, Å	$R_{A^iB^{ii}}^{x,p}$, Å
1.75 < In < 2.00, in $Y_3(Al,In)_5O_{12}$	0.615-0.630	0.541-0.554
2.00 < In < 2.25, in $Y_3(Ga,In)_5O_{12}$	0.696-0.706	0.602-0.610
1.00 < Cr < 1.25	0.534-0.540	0.464-0.468
1.00 < Mn < 1.25	0.540-0.548	0.471-0.477
0.25 < Co < 0.50	0.516-0.522	0.452-0.456
0.50 < Ni < 1.00	0.519-0.528	0.455-0.461

The mean cationic radius at which still formation of garnet phase occurs seems to be in rather large range of 0.516-0.706 Å or 0.452-0.610 Å irrespective whether the site occupancy have been involved or not into the calculation. Moreover, the limitary radius of $Y_3(Ga,In)_5O_{12}$ (0.701 Å) is comparable with published previously for the $Y_3(Sc,Ga)_5O_{12}$ system (0.711 Å) [111]. To conclude, there is no a particular rigid range of limitary radius value for garnet structure compounds. However, the limitary radius could be roughly predicted taking into account the ionic radius, the major oxidation state and the characteristic coordination number of the cations.

3.2. Luminescence Properties of co-Substituted YAG

According to the literature analysis and the experimental results, the Y-Al-In-O and Y-Al-Cr-O systems were chosen as the matrices to develop the luminescence properties of cerium, europium, terbium and erbium. In co-doped YAG aluminium situated at tetrahedral-octahedral sites is substituted by indium or chromium, while yttrium located at dodecahedral site is replaced by lanthanide.

3.2.1. Synthesis and Phase Identification of co-Substituted YAG

$Y_3Al_{3.5}In_{1.5}O_{12}$, $Y_3Al_{3.25}In_{1.75}O_{12}$, $Y_3Al_3In_2O_{12}$ and $Y_3Al_{4.75}Cr_{0.25}O_{12}$ garnets doped with different concentration (1%, 2%, 3%, 4% or 5%) of Ln^{3+} synthesized by sol-gel method were analysed by XRD. The XRD patterns of $Y_3Al_{3.5}In_{1.5}O_{12}$:3%$Ln^{3+}$ and $Y_3Al_{4.75}Cr_{0.25}O_{12}$:3%$Ln^{3+}$ powders prepared at 1000 °C are shown in Figure 14.

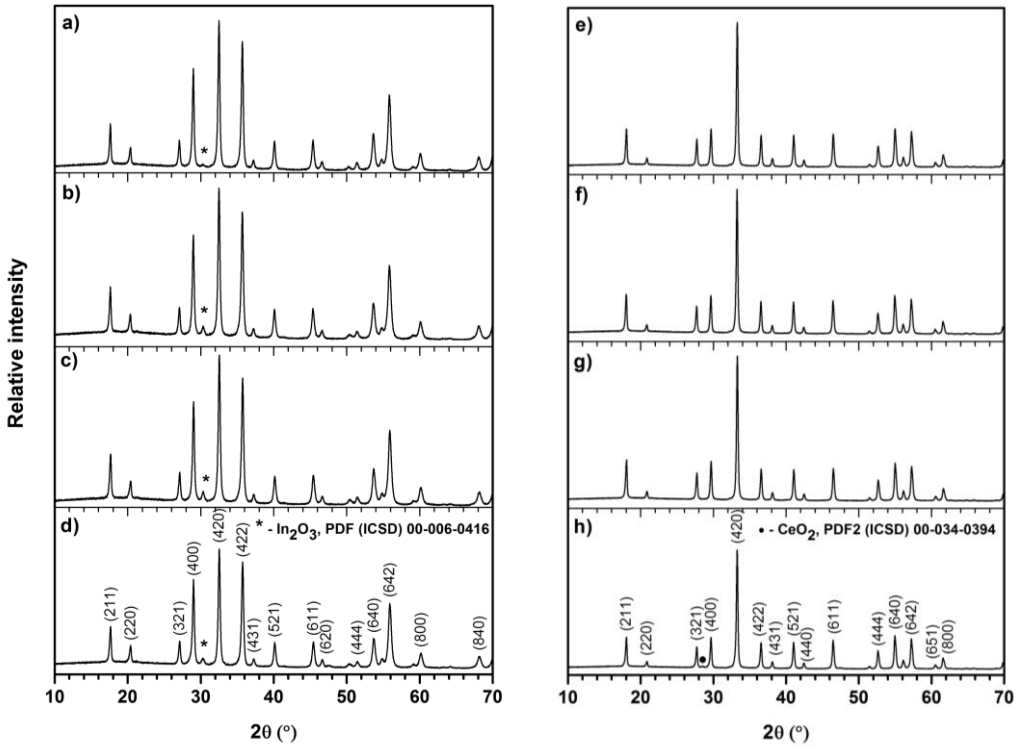

Fig. 14. XRD patterns of $Y_3Al_{3.5}In_{1.5}O_{12}$:3%$Ln^{3+}$ and $Y_3Al_{4.75}Cr_{0.25}O_{12}$:3%$Ln^{3+}$ samples annealed at 1000 °C for 10 h in air: a) $Y_3Al_{3.5}In_{1.5}O_{12}$:$Tb^{3+}$, b) $Y_3Al_{3.5}In_{1.5}O_{12}$:$Eu^{3+}$, c) $Y_3Al_{3.5}In_{1.5}O_{12}$:$Er^{3+}$, d) $Y_3Al_{3.5}In_{1.5}O_{12}$:$Ce^{3+}$, e) $Y_3Al_{4.75}Cr_{0.25}O_{12}$:$Tb^{3+}$, f) $Y_3Al_{4.75}Cr_{0.25}O_{12}$:$Eu^{3+}$, g) $Y_3Al_{4.75}Cr_{0.25}O_{12}$:$Er^{3+}$ and h) $Y_3Al_{4.75}Cr_{0.25}O_{12}$:$Ce^{3+}$.

The patterns evidently show the formation of single phase garnets, since all single spectral lines are indicated by Miller indexes corresponding to cubic crystal structure lattice and are in a good agreement with the reference data for YAG (PDF2 (ICSD) 04-006-3686). The diffraction line (420) with a relative intensity of 100%, the line (422) with 84-89% intensity and the line (400) with 69-74% intensity are the most intensive lines of $Y_3Al_{3.5}In_{1.5}O_{12}$:3%$Ln^{3+}$ samples, while the first three most intensive diffraction lines of $Y_3Al_{4.75}Cr_{0.25}O_{12}$:3%$Ln^{3+}$

compounds are indicated as (422), (211) and (640) and have 100%, 26-28% and 26-28% relative intensity, respectively. Note that each XRD pattern of $Y_3Al_{3.5}In_{1.5}O_{12}$:3%$Ln^{3+}$ contains an additional low-intensity line at 30.3°. This position corresponds to the most intensive (222) line of the In_2O_3 phase. If the content of indium is increased in the $Y_3(Al,In)_5O_{12}$:Ln^{3+} system ($Y_3Al_{3.25}In_{1.75}O_{12}$:$Ln^{3+}$ and $Y_3Al_3In_2O_{12}$:Ln^{3+}) the (222) line is expanded and new (211) and (440) diffraction peaks corresponding to In_2O_3 are observed at 21.3° and 50.5°, respectively.

All $Y_3Al_{4.75}Cr_{0.25}O_{12}$ samples doped with different content of Er^{3+}, Eu^{3+} or Tb^{3+} have no traces of crystalline phases of other garnet. The situation for the $Y_3Al_{4.75}Cr_{0.25}O_{12}$:$Ce^{3+}$ samples, however, was found to be different. $Y_3Al_{4.75}Cr_{0.25}O_{12}$ with up to 2 mol-% of cerium still have the structure corresponding solely to the garnet crystal. However, the XRD pattern of $Y_3Al_{4.75}Cr_{0.25}O_{12}$:3%$Ce^{3+}$ contains evidence of the secondary phase. The low-intensity (111) and (220) lines of CeO_2 phase are observed at 28.6° and 47.5°, respectively. The intensity of (111) and (220) lines is increased if cerium content is increased. The similar results were observed in the XRD patterns of $Y_3Al_5O_{12}$:Ce^{3+}[11]. Thus, single garnet structure phase was obtained only with a low concentration of Ce (up to 3 mol-%).

The microstructure and particle size distribution of the samples fabricated in the present study was characterized by SEM. Again, the morphology of co-doped garnet powder synthesized by sol-gel method is comparable of all samples made by this way. Thus, only SEM images of the representative $Y_3Al_{3.5}In_{1.5}O_{12}$:1%$Ce^{3+}$ and $Y_3Al_{4.75}Cr_{0.25}O_{12}$:3%$Ce^{3+}$ samples at different magnification are represented in Fig. 15. The particles of garnets possess foamy like morphology formed from highly agglomerated irregular spherical form crystallites with typical size of 0.5-1 μm. The size of agglomerates varies from 5 to 200 μm. The matrix influences the porosity of agglomerates [104]. The particles of $Y_3Al_{4.75}Cr_{0.25}O_{12}$:$Ln^{3+}$ seem to be more porous in comparison with $Y_3Al_{3.5}In_{1.5}O_{12}$:$Ln^{3+}$ powders. Furthermore, the inclusion of other phases is not

observed in the SEM images, while XRD patterns show the secondary phase of In_2O_3 or CeO_2, respectively.

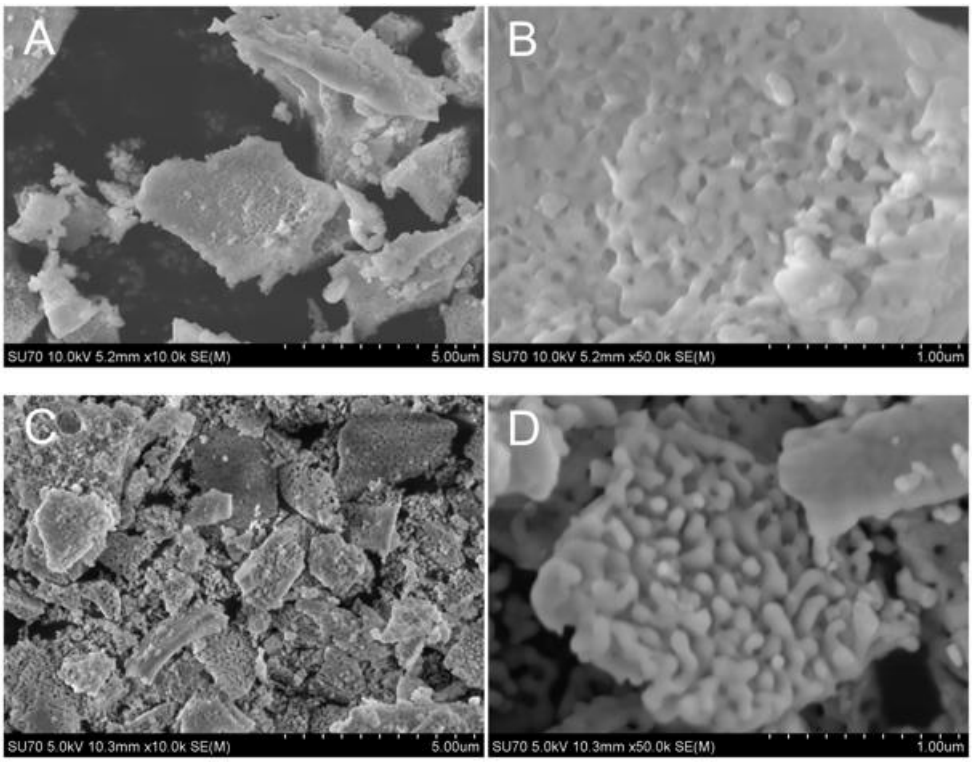

Fig. 15. SEM micrographs of $Y_3Al_{3.5}In_{1.5}O_{12}$:1%$Ce^{3+}$ (A), (B) and $Y_3Al_{4.75}Cr_{0.25}O_{12}$:3%$Ce^{3+}$ (C), (D) sintered at 1000 °C and obtained under different magnification.

3.2.2. $Y_3(Al,In)_5O_{12}$:Ce^{3+}phosphors

Figure 16 shows reflection, excitation and emission spectra as a function of Ce^{3+} concentration and indium content in $Y_3(Al,In)_5O_{12}$:Ce^{3+}. The luminescence spectra are normalized to unity by dividing the measured value by the maximum value of excitation and emission spectra, respectively. The body colour of prepared phosphors was yellowish, thus strongly suggesting that the absorption edge is located in the blue spectral range what is in a good agreement with the reflection spectra (see Fig. 16.). The absorption in blue region with the maximum at 440 nm depends on the concentration of cerium. The lowest reflection is observed if Ce^{3+} content is 3 mol-%.

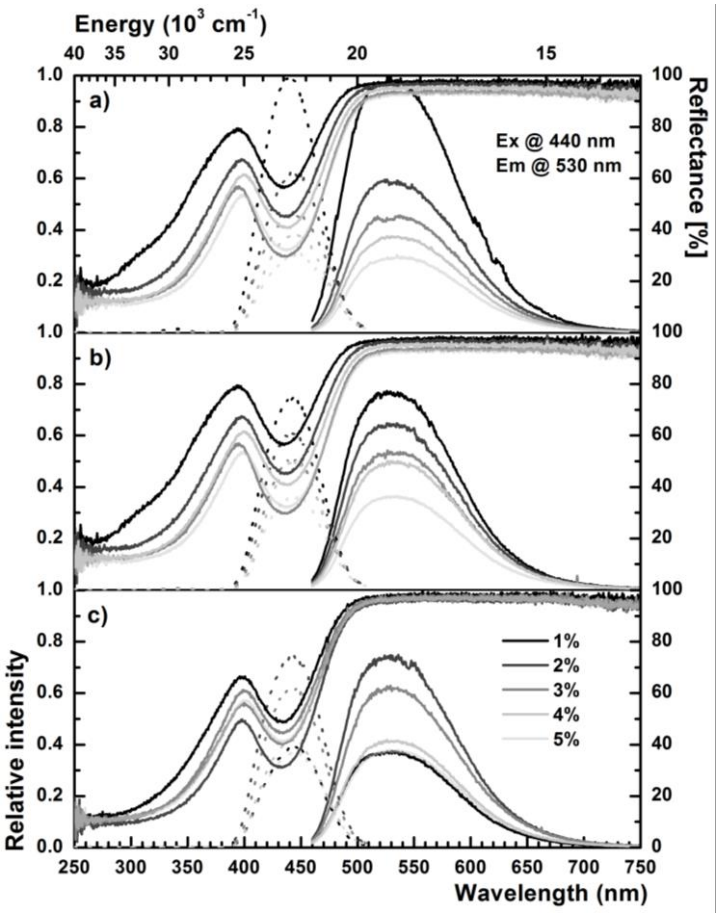

Fig. 16. Cerium-indium concentration dependent luminescence and reflection spectra of co-doped $Y_3Al_5O_{12}$: (a) $Y_3Al_{3.5}In_{1.5}O_{12}$:1-5%$Ce^{3+}$, (b) $Y_3Al_{3.25}In_{1.75}O_{12}$:1-5%$Ce^{3+}$ and (c) $Y_3Al_3In_2O_{12}$:1-5%Ce^{3+}.

If this limit is exceeded the reflection starts to increase. The minimum of reflection directly matches with the maximum of the peak in an excitation spectra. The monitored excitation spectra were measured at room temperature for the 530 nm emission. The peak with the maximum at 440 nm arises due to $[Xe]4f^1 \rightarrow [Xe]5d^1$ transitions. The excited state returns to the ground state, thus the phosphors doped with Ce^{3+} exhibit a broad band peak with the maximum at 530 nm corresponding to the $5d^1 \rightarrow {}^2F_{5/2}$ and $5d^1 \rightarrow {}^2F_{7/2}$ transitions in the emission spectra. The peak positions of experimental spectra illustrated in Fig. 16 a, b and c are in a good agreement with the PL data reported in the literature [11, 161, 162]. With increasing In^{3+} concentration a slight blue shift was observed by Zang *et al.* [163], while the emission shift of these $Y_3(Al,In)_5O_{12}$:Ce^{3+}samples was not detected. To conclude, the increase of

cerium concentration in the garnet matrix, as well as the replacement of aluminium by indium has led to weaker emission intensity.

3.2.3. $Y_3(Al,In)_5O_{12}:Eu^{3+}$phosphors

$Y_3(Al,In)_5O_{12}:Eu^{3+}$phosphors exhibit expectable luminescence properties for the europium doped garnets (Fig. 17) [155, 164].

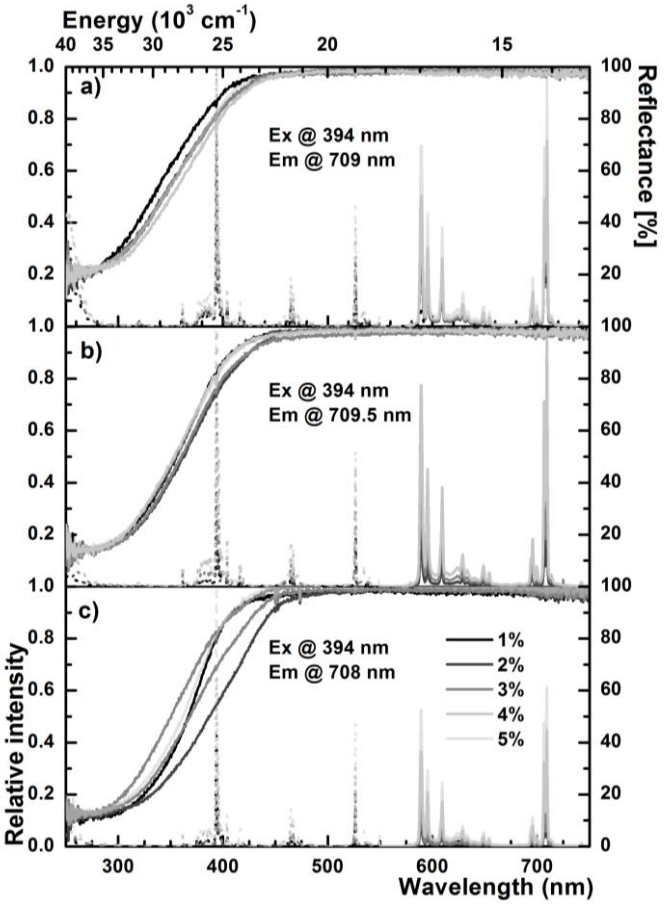

Fig. 17. Europium-indium concentration dependent luminescence and reflection spectra of co-doped $Y_3Al_5O_{12}$: (a) $Y_3Al_{3.5}In_{1.5}O_{12}$:1-5%$Eu^{3+}$, (b) $Y_3Al_{3.25}In_{1.75}O_{12}$:1-5%$Eu^{3+}$ and (c) $Y_3Al_3In_2O_{12}$:1-5%Eu^{3+}.

The reflectance in the visible region is very close to 100% indicating the good quality of the samples. The monitored excitation spectra of the europium doped $Y_3Al_{3.5}In_{1.5}O_{12}$, $Y_3Al_{3.25}In_{1.75}O_{12}$ and $Y_3Al_3In_2O_{12}$ powders were measured at room temperature for 709 nm, 709.5 nm and 708 nm emission, respectively. Three major sharp excitation lines are observed at 360-420, 450-

490, and 520-545 nm. These peaks originate from the $^7F_0 \rightarrow {}^5D_3$, $^7F_0 \rightarrow {}^5D_2$ and $^7F_0 \rightarrow {}^5D_1$ transitions of Eu^{3+}, respectively. The increase of europium concentration in the compound causes a slight intensity rise of the peaks. There is an additional domain in the PHE spectra at 250-280 nm corresponding to the Eu^{3+}-O^{2-} charge-transfer band (CTB). The maximum of the peak is not in the measured excitation range, but it is clearly visible that the increase of indium concentration causes a slight blue-shift of the CTB. The excited electronic states are quenched to the $^5D_0$ energy level. Then the energy is released as visible light and the excited electrons returns to the ^7F_Jground states multiplets. The intensity of the emission lines at 570-720 nm decrease with the increase of the indium concentration. This behaviour could be explained by the decrease of the local symmetry around Eu^{3+} for the solid solutions. The peaks at 580-600 nm, 600-640 nm, 640-660 and 690-715 nm are attributed to the $^5D_0 \rightarrow {}^7F_1$, $^5D_0 \rightarrow {}^7F_2$, $^5D_0 \rightarrow {}^7F_3$ and $^5D_0 \rightarrow {}^7F_4$ transitions, respectively. To conclude, the emission of $Y_3(Al,In)_5O_{12}$:Eu^{3+}samples is enhanced with the europium content upsurge caused by the increase of absorption centres.

3.2.4. $Y_3(Al,In)_5O_{12}$:Tb^{3+}phosphors

Figure 18 shows the luminescence and reflection spectra of Tb^{3+}-doped yttrium aluminium-indium garnets. The reflection spectra have no evidence of any absorbance lines at 400-750 nm and are close to unity demonstrating a low defect density of the samples. At 250-400 nm ~20% of the light is reflected due to the absorbance of the compound lattice, while in the monitored excitation spectrum for the 542.5 nm emission the peaks with the maximums at 267 nm and 317 nm are attributed to the low and high spin $[Xe]4f^8 \rightarrow [Xe]4f^75d^1$ transitions of Tb^{3+}, respectively. Evidence for the presence of $^7F_6 \rightarrow {}^5D_3$ transitions is given by the lines at 350-390 nm. Note, that excitation and emission peaks are heavily quenched if indium concentration is increased. The emission spectrum exhibits peaks at 487, 492, 543, 552, 583, 591, 618, 622, and 628 nm, while the most intense one is the peak at 543 nm. This yields a green-yellowish emission spectrum.

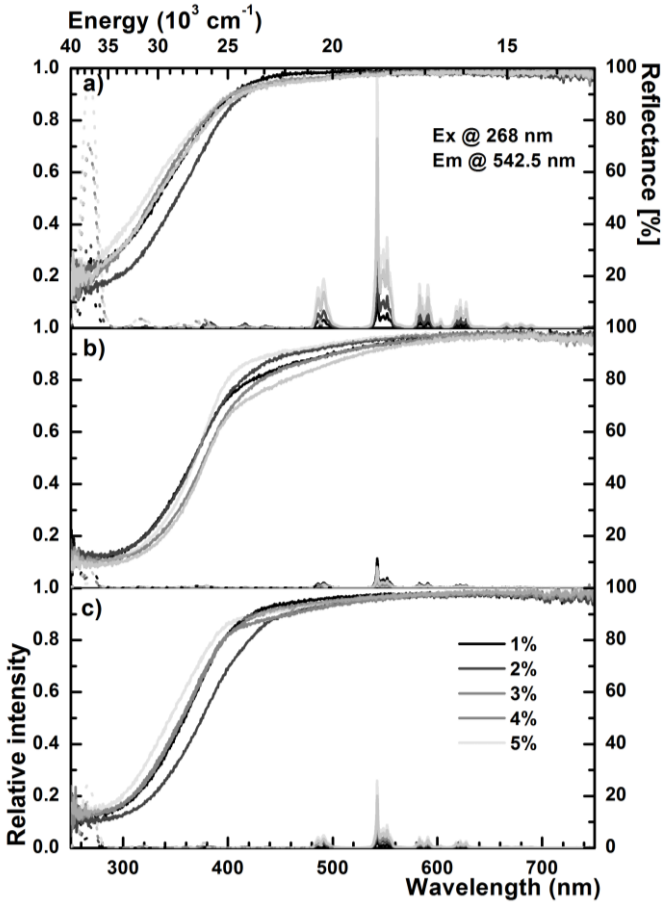

Fig. 18. Terbium-indium dependent luminescence and reflection spectra of co-doped $Y_3Al_5O_{12}$: (a) $Y_3Al_{3.5}In_{1.5}O_{12}$:1-5%$Tb^{3+}$, (b) $Y_3Al_{3.25}In_{1.75}O_{12}$:1-5%$Tb^{3+}$ and (c) $Y_3Al_3In_2O_{12}$:1-5%Tb^{3+}.

The different emission peaks corresponds to $^5D_4 \rightarrow {}^7F_6$ (at 480-510 nm, blue region), $^5D_4 \rightarrow {}^7F_5$ (at 535-565 nm, green region), $^5D_4 \rightarrow {}^7F_4$ and $^5D_4 \rightarrow {}^7F_3$ (at 580-610 nm and 610-635 nm, red region) transitions. Green emission is dominant because the Tb^{3+} concentration for all samples is high enough that cross relaxation from $^5D_3$ to $^5D_4$ occurs between adjacent ions. If the indium concentration is increased, the dramatic drop of emission intensity could be caused by the incorporation of Tb^{3+} ions not only into the D_{2h} symmetry sites. Therefore, energy transfer between dopants is decreased due to non-radiative relaxation processes [12, 165, 166].

3.2.5. $Y_3(Al,In)_5O_{12}:Er^{3+}$ phosphors

The luminescence properties of Er^{3+} in $Y_3(Al,In)_5O_{12}$ powders were measured at room temperature. The monitored spectra measured at room temperature for the 559 nm emission or under 487 nm excitation are illustrated in Figure 19.

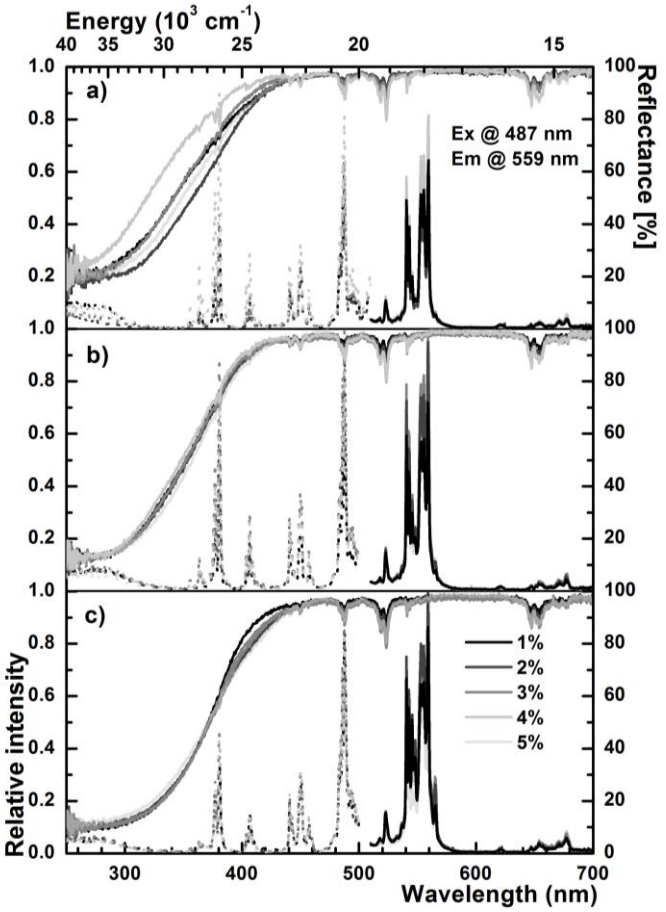

Fig. 19. Erbium-indium concentration dependent luminescence and reflection spectra of co-doped $Y_3Al_5O_{12}$: (a) $Y_3Al_{3.5}In_{1.5}O_{12}$:1-5%$Er^{3+}$, (b) $Y_3Al_{3.25}In_{1.75}O_{12}$:1-5%$Er^{3+}$ and (c) $Y_3Al_3In_2O_{12}$:1-5%Er^{3+}.

One can see that $Y_3(Al,In)_5O_{12}:Er^{3+}$ garnets with higher content of indium exhibit slightly higher intensity of the emission. The peaks corresponding to $^4S_{3/2} \rightarrow {}^4I_{15/2}$ transitions in the 530-580 nm range also become more broaden probably due to none-equivalent Er^{3+} sites in the compound. More lines of the weak erbium emission observed in the 515-530 nm and 640-690 nm ranges are attributed to $^2H_{11/2} \rightarrow {}^4I_{15/2}$ and $^4F_{9/2} \rightarrow {}^4I_{15/2}$, respectively [157]. Note that Er^{3+} ions emission is dependent not only on the indium content in the compound, but

it also irregularly varies due to the concentration of the lanthanide. The maximum of the emission of the erbium doped $Y_3Al_3In_2O_{12}$, $Y_3Al_{3.25}In_{1.75}O_{12}$ and $Y_3Al_{3.5}In_{1.5}O_{12}$ samples is reached if the Er^{3+} concentration is 2 mol-%, 3 mol-% and 4 mol-%, while the weakest emission is observed if the Er^{3+} concentration is 5 mol-%, 1 mol-% and 2 mol-%, respectively. The inconsistence of the erbium-doped phosphors emission probably arises regarding to the sensitivity of erbium ions to the secondary phase. The present of up-conversion (anti-Stokes luminescence) stage [15, 157] of yttrium indium aluminium garnet of the $Y_3(Al,In)_5O_{12}:Er^{3+}$ was not investigated.

In the excitation spectra in the range of 350-500 nm the observed groups of the peaks correspond to the transitions from the $^4I_{15/2}$ ground state to the $G_{9/2}$, $^4G_{11/2}$, $^2H_{9/2}$, $^4F_{5/2}$ and $^4F_{7/2}$ excited states. The excitation spectra perfectly match to the reflection spectra. It is worth noting that in the excitation spectra the ratio of the two most intensive peaks (the $^4I_{15/2} \rightarrow {}^4G_{11/2}$ and the $^4I_{15/2} \rightarrow {}^4F_{7/2}$ transitions) usually is <1. In the $Y_3Al_{3.5}In_{1.5}O_{12}$:4%$Er^{3+}$sample the situation is different. The reason why the $^4I_{15/2} \rightarrow {}^4G_{11/2}$ and $^4I_{15/2} \rightarrow {}^4F_{7/2}$ ratio is larger than one in this particular case was not found in the literature.

3.2.6. $Y_3Al_{4.75}Cr_{0.25}O_{12}:Ln^{3+}$ phosphors

The luminescence and reflection spectra of $Y_3Al_{4.75}Cr_{0.25}O_{12}:Ln^{3+}$ phosphors are presented in Figure 20. The reflection spectrum can be subdivided into two regions. In the green to red range the broad peak with the minimum at ~605 nm is observed in all $Y_3Al_{4.75}Cr_{0.25}O_{12}:Ln^{3+}$ phosphors. In the blue to green range the absorption peak with the minimum at ~457 nm is expressed only in the $Y_3Al_{4.75}Cr_{0.25}O_{12}:Ce^{3+}$ samples, while these peaks are not found in the rest of the samples. The region at 250-420 nm exhibits the highest absorption. Only 27 - 50% of radiation is reflected due to the absorbance of the host material. The reflectance of the samples is in a good agreement with their excitation spectra. All excitation and emission spectra were normalized to unity by dividing the data by the maximum value of excitation or emission intensity, respectively. This normalisation allows to compare the effect of doping lanthanide to the

luminescence properties in different $Y_3Al_{4.75}Cr_{0.25}O_{12}:Ln^{3+}$ phosphors. Note that the luminescence of lanthanides are completely quenched for all samples. Only evidence for the emission of Tb^{3+} is observed in the $Y_3Al_{4.75}Cr_{0.25}O_{12}:Tb^{3+}$ samples, while the excitation and emission peaks caused by Cr^{3+} transitions are dominating in all $Y_3Al_{4.75}Cr_{0.25}O_{12}:Ln^{3+}$ samples.

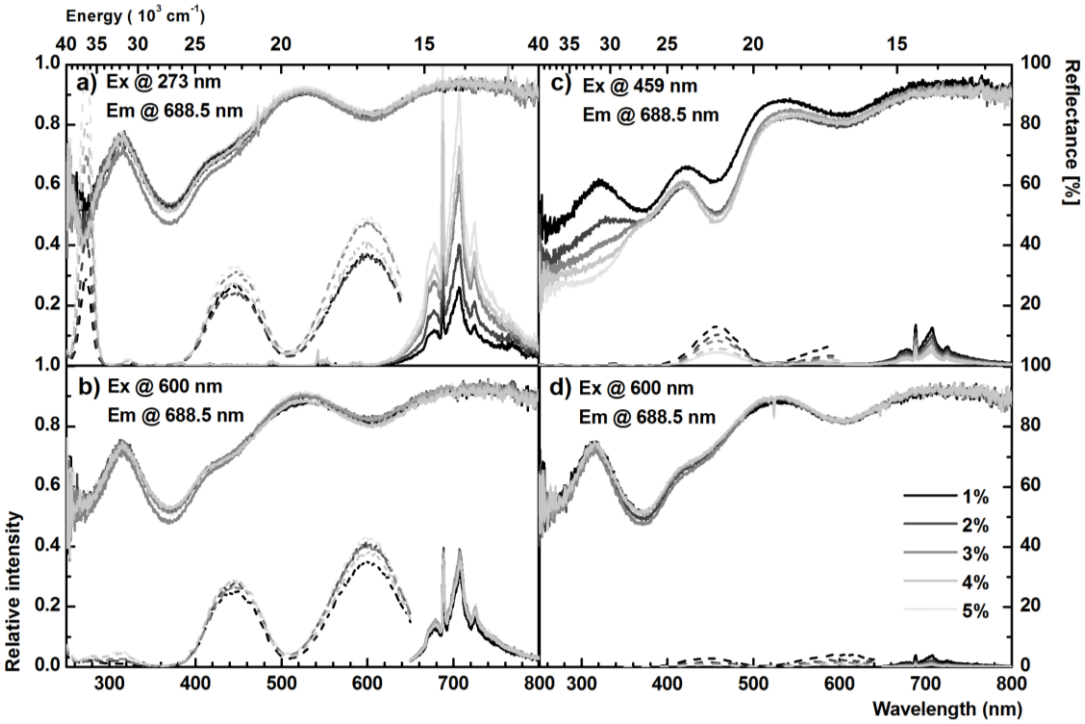

Fig. 20. Lanthanide concentration dependent luminescence and reflection spectra of doped (a) $Y_3Al_{4.75}Cr_{0.25}O_{12}$: 1-5%$Tb^{3+}$, (b) $Y_3Al_{4.75}Cr_{0.25}O_{12}$: 1-5%$Eu^{3+}$, (c) $Y_3Al_{4.75}Cr_{0.25}O_{12}$: 1-5%$Ce^{3+}$ and (d) $Y_3Al_{4.75}Cr_{0.25}O_{12}$: 1-5%$Er^{3+}$.

The excitation spectra of $Y_3Al_{4.75}Cr_{0.25}O_{12}:Ln^{3+}$ phosphors were measured at room temperature for the 688.5 nm emission. Each sample contains two broadband absorption bands of Cr^{3+} with a maximum at ~602 nm and ~446 nm, which are contributed to the spin-allowed $^4A_2 \rightarrow {}^4T_2$ and $^4A_2 \rightarrow {}^4T_1$ transitions, respectively. Only the $Y_3Al_{4.75}Cr_{0.25}O_{12}:Tb^{3+}$ samples show extra excitation peaks at ~267 nm and ~317 nm. The broad excitation bands caused by the Cr^{3+} crystal-field transitions in $Y_3Al_{4.75}Cr_{0.25}O_{12}:Ln^{3+}$ perfectly matches to the excitation peaks of Tb^{3+} in $Y_3(Al,In)_5O_{12}:Tb^{3+}$. This is a definite proof that in the co-doped garnet efficient energy transfer from Tb^{3+} to Cr^{3+} ions occurs. Moreover, energy transfer from Ce^{3+} to Cr^{3+} ions is also observed [167]. In

general, for the Tb^{3+}, Eu^{3+}, or Er^{3+} doped $Y_3Al_{4.75}Cr_{0.25}O_{12}$ and Cr^{3+} doped $Y_3Al_5O_{12}$ [19] the ratio of the intensities of the $^4A_2 \rightarrow {}^4T_1/{}^4A_2 \rightarrow {}^4T_2$ transitions is larger than one. Solely the $Y_3Al_{4.75}Cr_{0.25}O_{12}:Ce^{3+}$ composites have the opposite ratio of $^4A_2 \rightarrow {}^4T_1/{}^4A_2 \rightarrow {}^4T_2$ transitions intensities (lower than one). This behaviour could be explained by energy transfer from Ce^{3+} to Cr^{3+}, because excitation peaks of these ions overlap and match quite well (Fig. 16 and Fig. 20).

Fig. 20 shows that upon excitation at 273, 600, 459 or 600 nm, emission of $Y_3Al_{4.75}Cr_{0.25}O_{12}:Ln^{3+}$ (Ln^{3+} = Tb^{3+}, Eu^{3+}, Ce^{3+} or Er^{3+}, respectively) samples is observed in the far-red region. The most intense sharp line at 688.5 nm corresponds to the $^2E_4 \rightarrow {}^4A_2$ transitions [19]. The intensity of this peak decreases by 2.5 times once terbium is exchanged by europium, while the emission of $Y_3Al_{4.75}Cr_{0.25}O_{12}:Ce^{3+}$ and $Y_3Al_{4.75}Cr_{0.25}O_{12}:Er^{3+}$ composites is significantly quenched. The intensity of the emission peak at 688.5 nm decreases 7.5 and 25 times, respectively. Finally, the intensity of the chromium emission is strongly dependent on the concentration of Ln^{3+}. It is observed that the higher the concentration of terbium, the higher the emission intensity of chromium, while the situation in the $Y_3Al_{4.75}Cr_{0.25}O_{12}:Ce^{3+}$ and $Y_3Al_{4.75}Cr_{0.25}O_{12}:Er^{3+}$ samples is opposite. For instance, if the concentration of Ln^{3+} is increased from 1 to 5 mol - %, the intensity of the peak at 688.5 nm in the $Y_3Al_{4.75}Cr_{0.25}O_{12}:Tb^{3+}$ samples increases 3.5 times, in the $Y_3Al_{4.75}Cr_{0.25}O_{12}:Ce^{3+}$ and $Y_3Al_{4.75}Cr_{0.25}O_{12}:Er^{3+}$ samples the intensity decreases by about 2.5 and 5.5 time, respectively. The intensity of the emission of europium doped samples is almost constant, i.e. independent on the concentration of europium.

3.3. Eu^{3+} Emission in Garnet Structure Hosts

The third part of experimental work was devoted to investigate europium luminescence properties in garnet structure hosts. The $^5D_0 \rightarrow {}^7F_{1,2}$ transitions of Eu^{3+} are widely explored due to the practical application of europium doped compounds as a component for different type of displays, while the $^5D_0 \rightarrow {}^7F_4$ transitions were “forgotten”, because the human eye is insensitive to this

particular wavelength emission. The garnet host was chosen, since the composition of the matrix is easily modified.

3.3.1. Dependence of the $^5D_0 \rightarrow {}^7F_4$ Transitions of Eu^{3+} on the Local Environment in Garnet Powders

The XRD patterns of obtained powders of $Y_3Al_5O_{12}$ (YAG), $Y_3Ga_5O_{12}$ (YGG), $Gd_3Ga_5O_{12}$ (GGG), $Lu_3Al_5O_{12}$ (LuAG), and $Lu_3Ga_5O_{12}$ (LuGG) samples doped with 1% Eu^{3+} are shown in Figure 21.

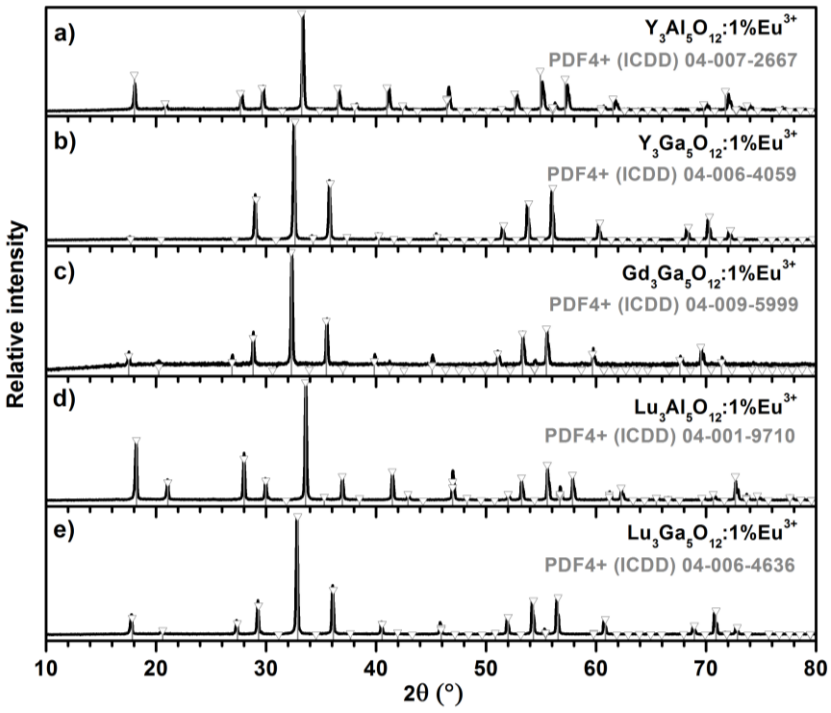

Fig. 21. XRD patterns of YAG, YGG, GGG, LuAG and LuGG samples annealed at 1500 or 1400 °C for 4 h in air.

The obtained patterns match well with reference patterns which are also given for comparison. All synthesized materials are single phase. As expected, there are some changes in the peak position due to different ionic radii of Lu, Y, and Gd located onto dodecahedral lattice site and Al, Ga located onto octahedral and tetrahedral lattice sites [48]. Due to the different X-ray scattering power of the rare earth ions and of Al and Ga, the peak intensities in the XRD patterns also slightly fluctuate [168].

Figures 22, 23 and 24 display the reflection, excitation and emission spectra of the YAG-YGG, LuAG-LuGG and YGG-GGG series, respectively. The body colour of all synthesized powders is pure white. This goes hand in hand with the reflection spectra, where very little absorption in the visible region is observed. The reflectance values at longer wavelengths are close to unity indicating high brilliance of the prepared materials. The typical Eu^{3+} absorption lines originating from the $^7F_0 \rightarrow {}^5L_6$ transitions are observed in the range of 395-397 nm in each reflection spectrum.

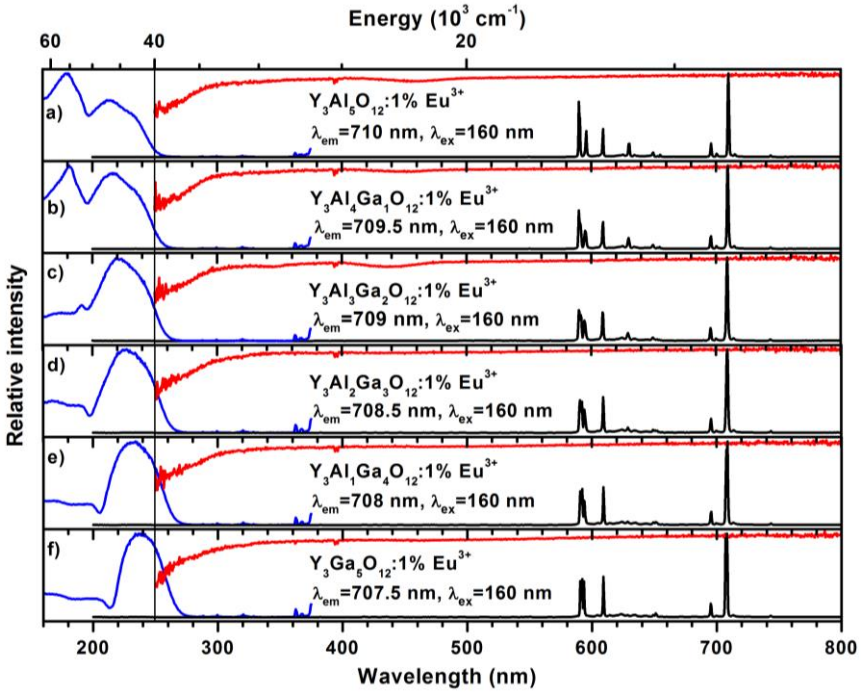

Fig. 22. Reflection, excitation and emission spectra of YAG-YGG system samples.

The excitation spectra monitored at $\lambda_{em} \approx 710$ nm reveal that the charge transfer (CT) to Eu^{3+} occurs in all garnet samples in the UVC range. It is also evident that the CT energy decreases with increasing gallium content in the structure, which is in a good agreement with the recent work of P. Dorenbos [169]. The observed CT band shift to lower energy upon increasing Ga content can be attributed to the resulting longer RE-O bond length. For instance, substituting all Al by Ga in YAG results in an average Y-O bond length increase from 2.371 to 2.390 Å [29] and it is well known that CT energy decreases with larger average distance to the surrounding anions [170-172]. The CT band shift

is obvious for the YAG-YGG and LuAG-LuGG systems. However, this trend is not so visible for the YGG-GGG system due to similar radii of Y^{3+} and Gd^{3+} ions. Besides the slight CT band shift to lower energy the narrowing of the CT band itself was also observed. In addition to the CT band, samples containing Gd^{3+} ions also possessed some lines at around 275 and 310 nm in the excitation spectra monitored for the Eu^{3+} emission at 710 nm. These lines are attributed to the $^8S_{7/2} \rightarrow {}^6I_J$ and $^8S_{7/2} \rightarrow {}^6P_J$ transitions of Gd^{3+} ions, respectively, and are an evidence of efficient $Gd^{3+} \rightarrow Eu^{3+}$ energy transfer.

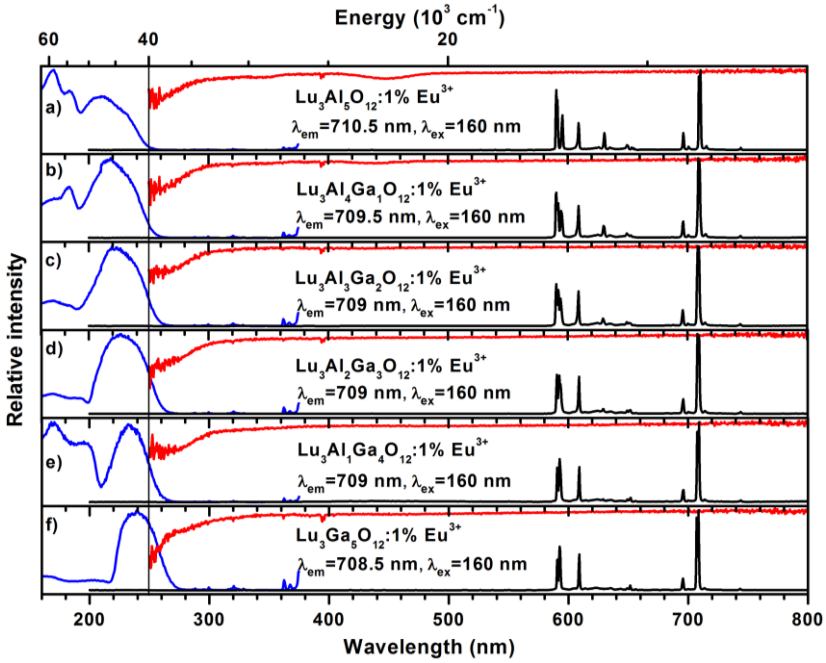

Fig. 23. Reflection, excitation and emission spectra of LuAG-LuGG samples.

All powders were excited at 160 nm for taking the emission spectra, which were corrected according to the system calibration file. Three major emission lines are observed at 585-600, 610-625, and 680-720 nm originating from the $^5D_0 \rightarrow {}^7F_J$ transitions of Eu^{3+} ions. The strongest emission at 680-720 nm originates from $^5D_0 \rightarrow {}^7F_4$ transitions of Eu^{3+}. The $^5D_0 \rightarrow {}^7F_1$ and $^5D_0 \rightarrow {}^7F_2$ transitions of Eu^{3+} are causing the lines at 585-600 nm and 610-625 nm, respectively. The emission spectra of YAG-YGG, LuAG-LuGG and YGG-GGG garnets are in a very good agreement with the emission spectra of $Ca_3Sc_2Si_3O_{12}$ garnet doped with Eu^{3+} proposed by Bettinelli et al. [155].

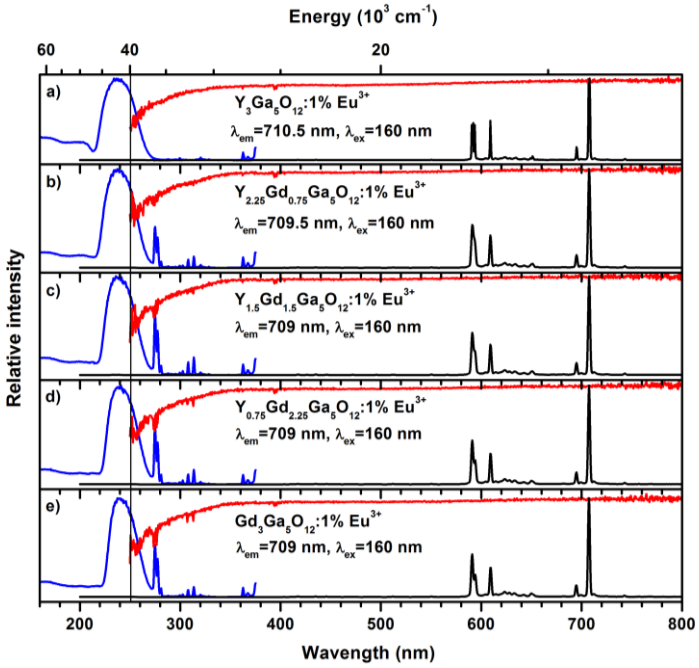

Fig. 24. Reflection, excitation and emission spectra of YGG-GGG samples.

The intensity of all spectra was normalized to unity. Therefore, the Eu^{3+} emission spectra are observed as a function of the host matrix composition. The intensity of $^5D_0 \rightarrow {}^7F_1$ transition decreases with increasing Ga content in the structure regardless of the rare earth ion onto the dodecahedral site. On the other hand, the intensity of $^5D_0 \rightarrow {}^7F_2$ transition slightly increases following the same trend. Furthermore, the emission spectra of the samples without Ga^{3+} in the structure contain well defined sharp lines. However, with addition of Ga^{3+} ions those lines tend to broaden and merge due to the formation of nonequivalent Eu^{3+} sites leading to the emission at slightly different wavelengths. Those emission lines then overlap resulting in a broader line. It is also interesting to note that no typical Gd^{3+} line emission was observed for the garnet samples containing gadolinium, even though they were excited at 160 nm.

The ionic radius and electronegativity (EN) of M^{3+}cations of host matrixes were given in Table 2. Table 4 shows the average EN values of all M^{3+} cations in the compound (**EN-all**), the average EN values of M^{3+} cations occupying octahedral and tetrahedral sites (**EN-oct-tetr**), absorption at 254 nm (**Abs.**), luminous efficacies (**LE)** and the percentage fraction of the emission of

$^5D_0 \rightarrow {}^7F_4$ transition (integral of 680-720 nm range) with respect to the whole Eu^{3+} emission spectrum (integral of 570-720 nm range) (**Em_4**).

Table 4. Characteristics of synthesized samples

Compound	EN-all	EN-otc-tetr	Abs. [%]	LE [lm/W]	Em_4 [%]
$Y_3Al_5O_{12}$: 1% Eu^{3+}	1.45	1.51	39	372	39.5
$Y_3Al_4Ga_1O_{12}$: 1% Eu^{3+}	1.46	1.53	51	354	41.6
$Y_3Al_3Ga_2O_{12}$: 1% Eu^{3+}	1.46	1.54	48	355	41.5
$Y_3Al_2Ga_3O_{12}$: 1% Eu^{3+}	1.47	1.55	48	352	43.3
$Y_3Al_1Ga_4O_{12}$: 1% Eu^{3+}	1.48	1.57	30	353	43.4
$Y_3Ga_5O_{12}$: 1% Eu^{3+}	1.49	1.58	59	353	44.6
$Lu_3Al_5O_{12}$: 1% Eu^{3+}	1.48	1.51	29	356	39.8
$Lu_3Al_4Ga_1O_{12}$: 1% Eu^{3+}	1.49	1.53	34	342	41.5
$Lu_3Al_3Ga_2O_{12}$: 1% Eu^{3+}	1.50	1.54	47	351	42.7
$Lu_3Al_2Ga_3O_{12}$: 1% Eu^{3+}	1.51	1.55	39	352	43.1
$Lu_3Al_1Ga_4O_{12}$: 1% Eu^{3+}	1.52	1.57	41	311	42.1
$Lu_3Ga_5O_{12}$: 1% Eu^{3+}	1.52	1.58	65	373	43.2
$Y_{2.25}Gd_{0.75}Ga_5O_{12}$: 1% Eu^{3+}	1.49	1.58	50	362	43.0
$Y_{1.5}Gd_{1.5}Ga_5O_{12}$: 1% Eu^{3+}	1.50	1.58	46	361	43.3
$Y_{0.75}Gd_{2.25}Ga_5O_{12}$: 1% Eu^{3+}	1.50	1.58	52	361	42.2
$Gd_3Ga_5O_{12}$: 1% Eu^{3+}	1.51	1.58	58	359	42.9
YPO_4: 1% Eu^{3+}	1.340	-	10	336	47.9
$LaPO_4$: 1% Eu^{3+}	1.327	-	65	371	44.5
$GdPO_4$: 1% Eu^{3+}	1.386	-	16	387	47.0
$LuPO_4$: 1% Eu^{3+}	1.431	-	33	354	49.8

The minor shift (~2-3 nm) of the Eu^{3+} emission peak maximum to the shorter wavelengths was observed if aluminium was replaced by gallium (see Figure 22 and Figure 23), thus indicating the weak crystal field effect on the 4f-4f transitions of Eu^{3+} ions. Moreover, it was also noted that the fraction of $^5D_0 \rightarrow {}^7F_4$ transition with respect to the whole emission spectrum increases with increasing average EN values of M^{3+} ions in the garnet structure compounds. This consistent pattern is also common in rare earth orthophosphates (Table 4). The observed trends are shown in Figure 25. The increasing fraction of the $^5D_0 \rightarrow {}^7F_4$ transition in the emission spectra is also expected to reduce the luminous efficacy of the phosphor due to low human eye sensitivity in this spectral region.

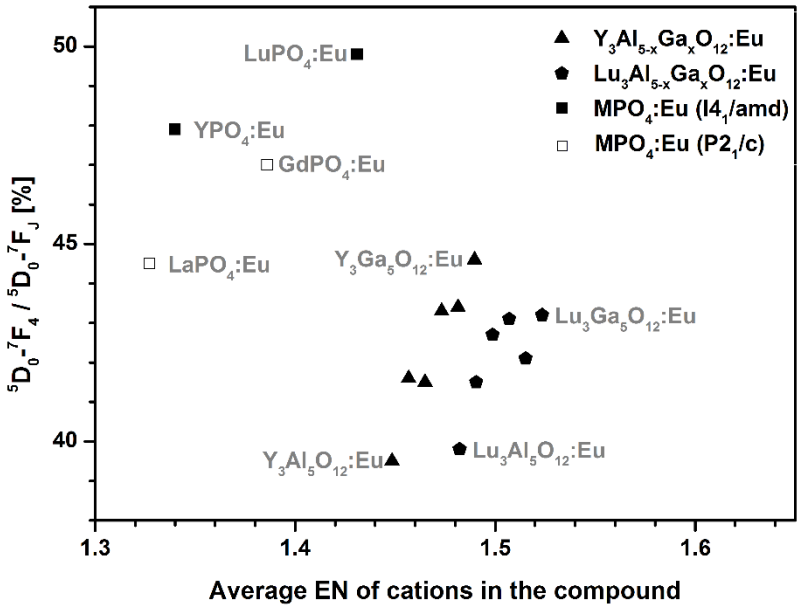

Fig. 25. The ratio of $^5D_0 \rightarrow {}^7F_4$ / $^5D_0 \rightarrow {}^7F_J$ as a function of the average EN values of all cations in the host matrix.

The dependence of the $^5D_0 \rightarrow {}^7F_4$ transitions of Eu^{3+} was described by R. A. Sa Ferreira *et al.* in 2006 [173]. It was demonstrated, that if the solution of $Na_9[EuW_{10}O_{36}]$ is diluted the environment of Eu^{3+} is more polarized due to the geometric distortion of the environment. It causes a decrease of the intensity of the $^5D_0 \rightarrow {}^7F_1$ and $^5D_0 \rightarrow {}^7F_4$ transitions in the emission spectrum, while the $^5D_0 \rightarrow {}^7F_2$ transitions are increased. In the present work, the environment of Eu^{3+} ions is more polarized if the cations in the compound has lower EN. Therefore, the emission of the $^5D_0 \rightarrow {}^7F_4$ transitions is increased with increasing of EN as it is demonstrated in the Figure 25.

Figure 26 shows decay curves of YAG:Eu^{3+} and YGG:Eu^{3+} samples and decay time dependence on x in $Y_3Al_{5-x}Ga_xO_{12}$:1%Eu^{3+} or $Lu_3Al_{5-x}Ga_xO_{12}$:1%Eu^{3+}. The decay curves were fitted by a single exponential decay $I(t) = I_0 \cdot exp(-t/\tau)$, where $I(t)$ is intensity at a given time t, I_0 is the initial intensity, and τ is a lifetime [174]. It is obvious that decay times get shorter with increasing gallium instead of aluminium. The shortened decay times usually corresponds to decreased efficiency of the activator ions. The shortened decay time again could be associated to the polarization of the local activator ion environment. The site is more polarized, the decay time is longer. To conclude, the exhibiting

high lifetime (ms range) and optical image generation in transparency window of tissue (the relatively high-transmission spectral region between 650-1100 nm) enable the deep red and NIR emitting inorganic particles to be applied in biochemical and medical imaging.

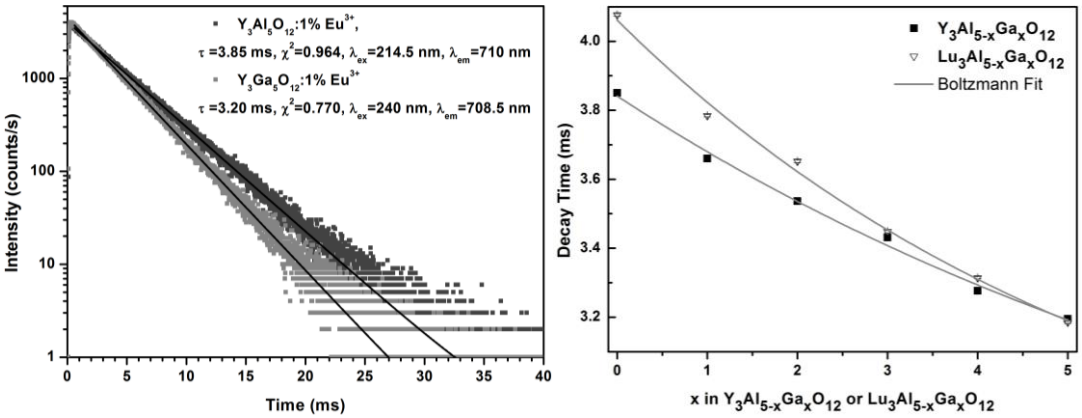

Fig. 26. Decay curves of YAG:Eu^{3+} and YGG:Eu^{3+} (left) and decay time dependence on the chemical composition (right).

3.3.2. Synthesis and Luminescence Properties of Europium-Doped YAG, YGG and $Y_3(Al,In)_5O_{12}$ Crystals

This study allows to discuss the size-dependent luminescence properties of europium doped garnets. The precursor powder of YAG:5%Eu^{3+}, YAG:30%Eu^{3+}, YGG:5%Eu^{3+}, YGG:30%Eu^{3+} and $Y_3Al_{4.5}In_{0.5}O_{12}$:5%$Eu^{3+}$ were synthesized by solid-state reaction. The XRD patterns (Figure 27a,b,c,d) shows that YAG:5%Eu^{3+} and YAG:30%Eu^{3+} powders even annealed at 1500-1550 °C contain impurity perovskite yttrium aluminate ($YAlO_3$, PDF2 (ICSD) 00-033-0041) phase. The peaks of YGG:5%Eu^{3+} and YGG:30%Eu^{3+} diffraction patterns are attributed lonely to the garnet phase since all peaks are analogous to XRD pattern of YGG (PDF2 (ICSD) 00-043-0512).

The precursor powders were used to grow crystals by the traveling solvent floating zone method. The YAG:5%Eu^{3+}, YGG:5%Eu^{3+} and YGG:30%Eu^{3+} crystals were grown in pure argon atmosphere, while during the growth of YAG:30%Eu^{3+} 1% of oxygen was added. In addition, the crystal of $Y_3Al_{4.5}In_{0.5}O_{12}$ was grown unsuccessfully. The precursor powders obtained by

solid-state reaction synthesis contained the impurities of $YAlO_3$, $Y_4Al_2O_9$ and other mixed-metal oxides. Due to the evaporation of indium oxide during the growth, it was difficult to find/keep an optimal growth conditions and the final polycrystalline product was the mixture of garnet and perovskite phases, while Kawata *et al.* has successfully grown the crystal of $Gd_3In_2Ga_3O_{12}$ by the floating zone method [175].

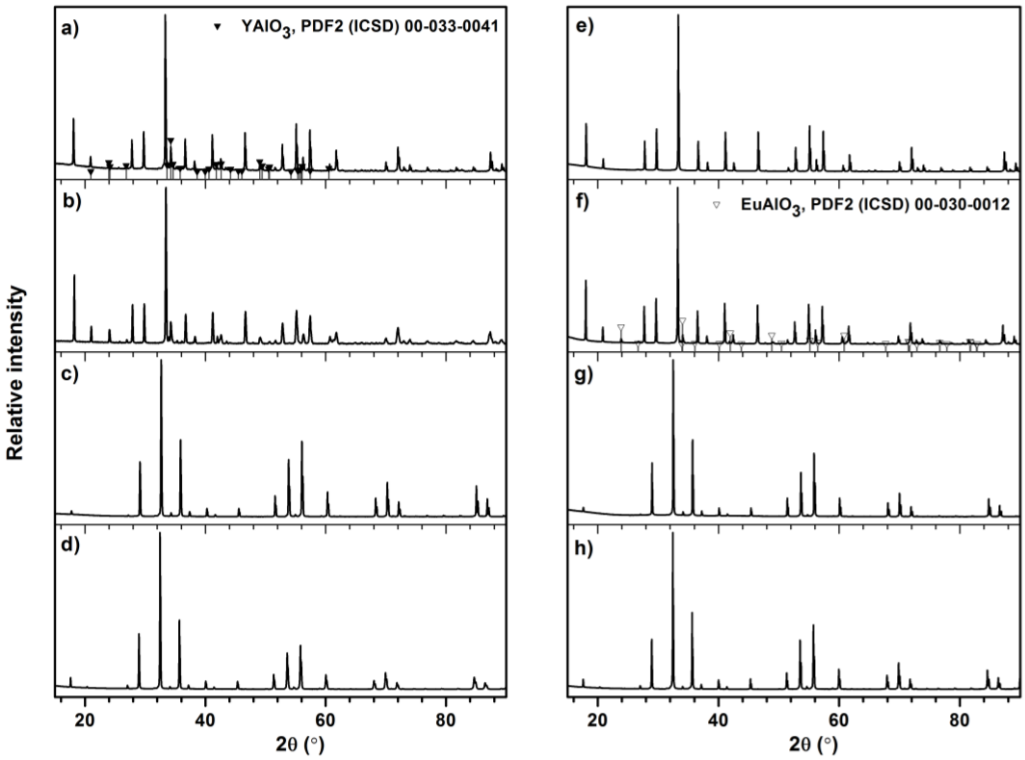

Fig. 27. The XRD patterns of precursor powders annealed at 1500 °C ((a) YAG:5%Eu^{3+}, (b) YAG:30%Eu^{3+}, (c) YGG:5%Eu^{3+} and (d) YGG:30%Eu^{3+}) and ground crystals ((e) YAG:5%Eu^{3+}, (f) YAG:30%Eu^{3+}, (g) YGG:5%Eu^{3+} and (h) YGG:30%Eu^{3+}).

The small pieces of the product were cut by diamond saw and ground for XRD analysis (Figure 27e,f,g,h). These XRD patterns confirms that the single phase garnets YAG:5%Eu^{3+}, YGG:5%Eu^{3+} and YGG:30%Eu^{3+} were obtained. However, the crystal grown using YAG:30%Eu^{3+} precursor powders retains the impurity (Y,Eu)AlO_3 phase . The peaks signed by empty triangular refer to the peaks of $EuAlO_3$ (PDF2 (ICSD) 00-030-0012) in Figure 27f. Note, that it is difficult to clarify the cause of the origin of the impurity phase. The data of Table

5 implies, that the content of europium or adding 1% of oxygen in growing atmosphere are not the only reasons for the formation of the impurity. The proper conditions for the growth of YAG:30%Eu^{3+} should be improved (pressure, growth rate, atmosphere and etc.) in order to obtain a single-phase product considering the pure $Eu_3Al_5O_{13}$ has been obtained [105].

Table 5. The growth atmosphere and identified phases of the grown crystals.

Crystal	**Growth atmosphere**	**Identified phases**
YAG:5%Eu^{3+}	100% Ar	Garnet
YAG:5%Eu^{3+}	80% Ar and 20% O_2	Garnet
YAG:30%Eu^{3+}	100% O_2	Garnet and (Y,Eu)AlO_3
YAG:30%Eu^{3+}	99% Ar and 1% O_2	Garnet and (Y,Eu)AlO_3
YGG:5%Eu^{3+}	100% Ar	Garnet
YGG:30%Eu^{3+}	100% Ar	Garnet

The Laue XRD technique was used to investigate the quality of the crystals. If the simulated pattern matches well the Laue pattern of XRD, this indicates, that each reflected plane is identified. Such single crystal can be re-orientated to the desired position. Laue patterns of YAG:5%Eu^{3+}, YAG:30%Eu^{3+}, YGG:5%Eu^{3+} and YGG:30%Eu^{3+} crystals are demonstrated in Figure 28.

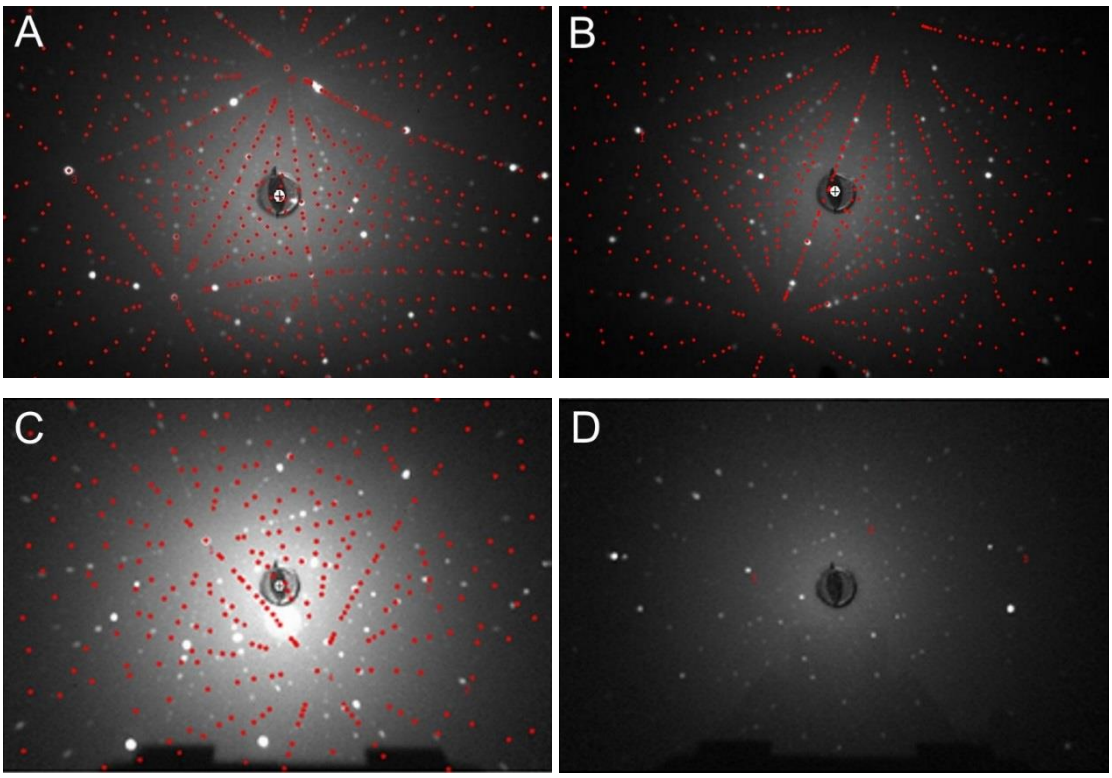

Fig. 28. Laue patterns of XRD of (A) YAG:5%Eu^{3+}, (B) YAG:30%Eu^{3+}, (C) YGG:5%Eu^{3+} and (D) YGG:30%Eu^{3+} crystals. Red points exhibit the simulated Laue pattern.

It is obvious that obtained and simulated points matches well in Figure 28A representing the high quality of the YAG:5%Eu^{3+}. The obtained Laue pattern of YAG:30%Eu^{3+} contains extra spots (planes). This could be explained by the secondary phase which was also identified by XRD technique. The Laue XRD measurements has demonstrated, that YGG:5%Eu^{3+} and YGG:30%Eu^{3+} crystals (Figure 28 C and D, respectively) contains many defects. The observed and simulated points of YGG:5%Eu^{3+} doesn't match, while the high symmetry points in the Laue pattern of YGG:30%Eu^{3+} have not been identified.

X-ray fluorescence method showed the distribution of europium, yttrium and aluminium or gallium ions on the cut crystal surface. The pictures of YGG:30%Eu^{3+} grown at argon atmosphere is demonstrated in Figure 29. It can be clearly seen, that europium ions are concentrated and content of yttrium, aluminium or gallium is decreased at the interfaces of defects. The distribution of ions on other crystal surface is not presented, because the data are very similar to the given pictures of the YGG:30%Eu.

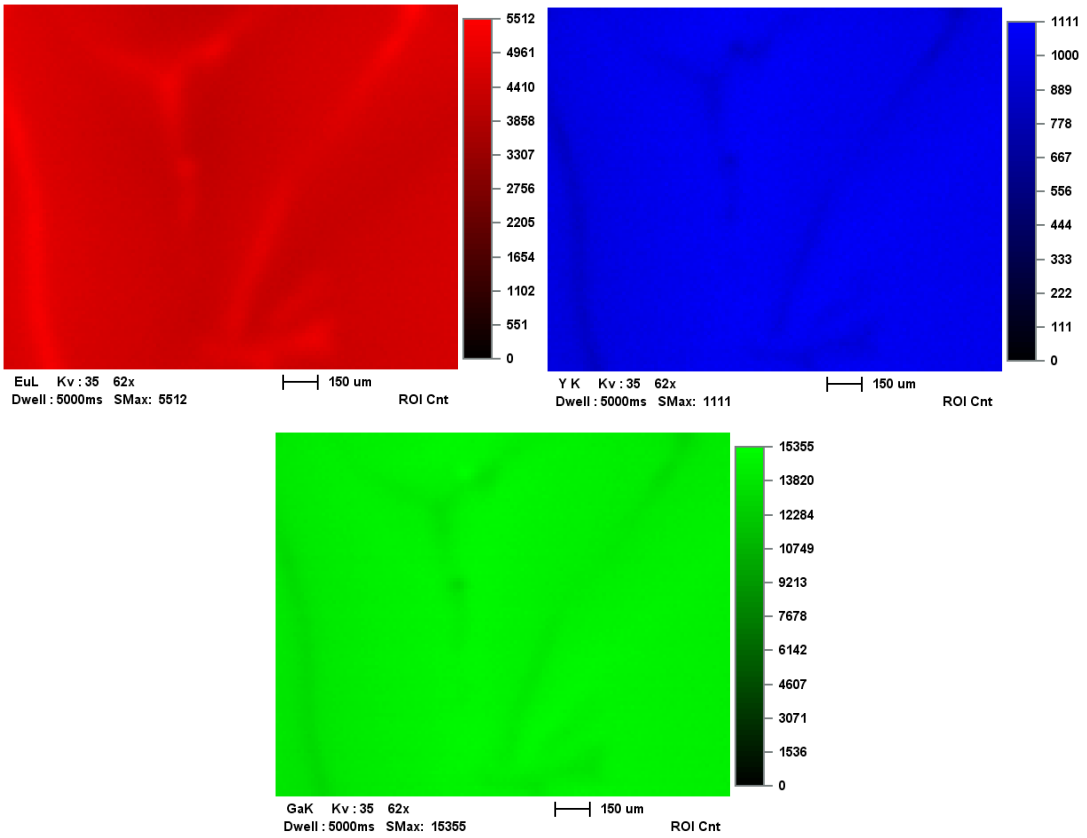

Fig. 29. Distribution of Eu, Y and Ga ions in the YGG:30%Eu^{3+}.

The photoluminescence properties of europium doped crystals are presented in Figure 30. Excitation spectra of the YAG:Eu^{3+} and YGG:Eu^{3+} precursor powders and crystals were measured at room temperature at the recorded 590.5 nm and 592 nm emission wavelength, respectively. It contains several intensive sharp lines associated to the f-f electronic transitions of Eu^{3+} ions with maximum at 394 nm ($^7F_0 \rightarrow {}^5L_6$ transitions). The peaks with maximum at 527, 465, 362, 347.5, 320 nm could be attributed to the $^7F_0 \rightarrow {}^5D_1$, $^7F_0 \rightarrow {}^5D_2$, $^7F_0 \rightarrow {}^5D_4$, $^7F_0 \rightarrow {}^5L_{10}$ and $^7F_0 \rightarrow {}^5H_6$, respectively. The 370-390 nm range is rich of the peaks due to the $^7F_0 \rightarrow {}^5L_{6,7,8}$ and $^7F_0 \rightarrow {}^5G_{2,4,5,6}$ transitions [176]. It is obvious that the quantity of the direct f-f electronic transitions is increased with the concentration of europium. This could be explained by the increased luminescent centres of europium. There is one more domain in the excitation spectra in the 250-280 nm region which contains the Eu^{3+} and O^{2-} charge-transfer band (CTB). First, with increasing the unit-cell volume (Ga^{3+} is larger than Al^{3+} and Eu^{3+} is larger than Y^{3+}), a redshift of a CTB band is observed. The peaks of

YAG:5-30%Eu and YGG:5-30%Eu crystals are located at 252, 254, 260.5 and 268 nm, respectively. The redshift and narrowing of CTB is also inherent for $Y_3(Al,Ga)_5O_{12}$, $Lu_3(Al,Ga)_5O_{12}$, $(Y,Gd)_3Ga_5O_{12}$ and YBO_3:Eu. Wei *et al.* explained such behaviour by bonding [177]. In the CTB excitation, O 2*p* electrons are promoted to the 4 *f* levels of Eu^{3+} ions, therefore, the peak position of the CTB band is determined by the energy difference between the O 2*p* valence bands and the Eu 4 *f* levels. If the cell volume of unit-cell would increase, the Y-O and Eu-O bond distance would increase accordingly. It is clear that the bonding interaction would be weaker in the smaller particle-sized sample, one could, therefore, expect that the energy level of the O 2*p* valence band would rise, while that of the Y 4*d* + 15*s* (Eu 5*d* + 16*s*) conduction band and Eu 4 *f* level would descend. The total effect of increasing the unit-cell volume on the energy levels perhaps resulted a narrower band gap between the O *2p* valence and Eu *4 f*. The narrowing of CTB might also result from the weakening of the interactions between the Eu^{3+} ions with the surrounding. Finally, the powders have rather large surface, therefore the CTB exhibit very high intensity peak in excitation spectra for precursor powders, while the intensity of CTB peak in crystals is reduced 2.3-3.7 times, respectively.

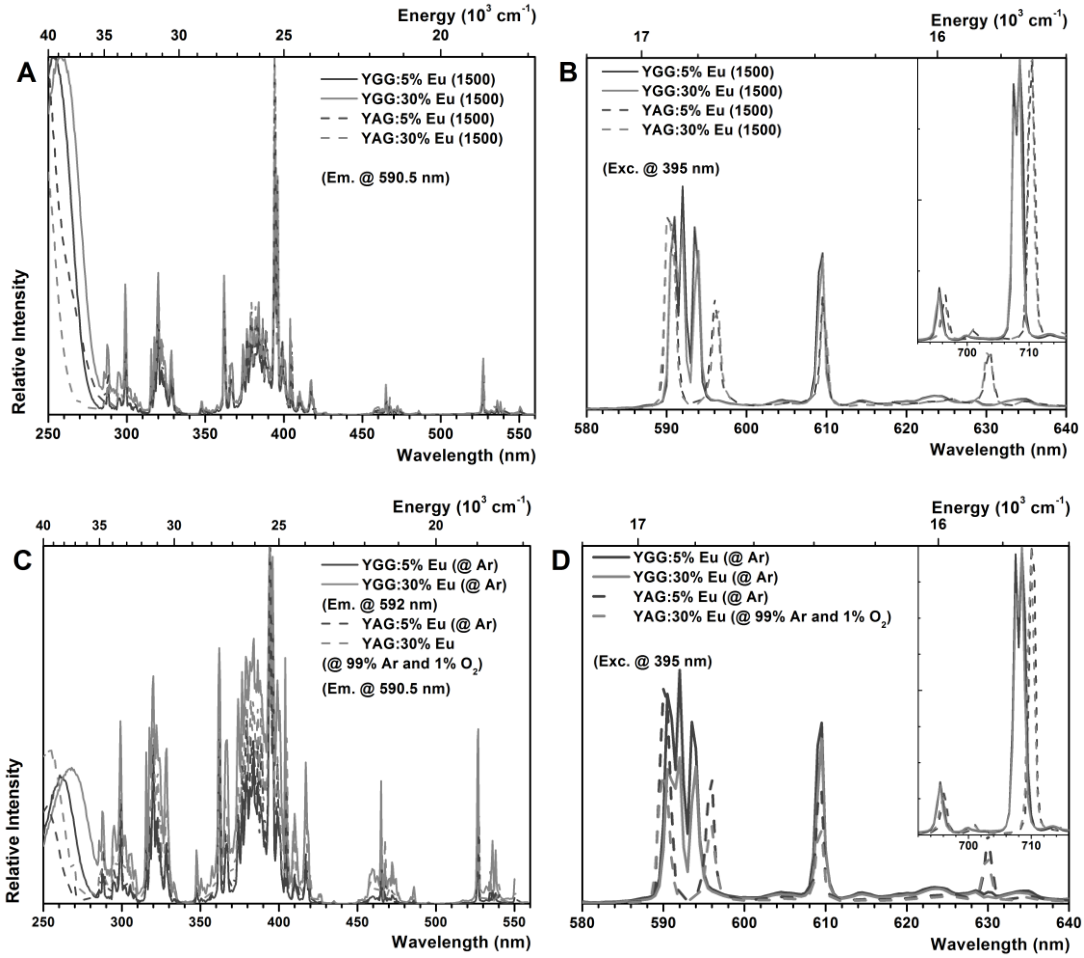

Fig. 30. Excitation and emission spectra of the precursor powder (A and B, respectively) and crystals (C and D, respectively).

The emission spectra reveal the presence of peaks at 590.5 or 592 nm, 609.5 nm and 710 or 708.5 nm, attributed to $^5D_0 \rightarrow {}^7F_1$, $^5D_0 \rightarrow {}^7F_2$ and $^5D_0 \rightarrow {}^7F_4$ transitions, respectively. The terms of Judd-Ofelt theory describes the intensity of the transitions between different *J* levels depending on the symmetry of the local environment of the Eu^{3+} activators. Magnetic dipole transitions ($^5D_0 \rightarrow {}^7F_{1,3}$) are permitted, while electric dipole transitions ($^5D_0 \rightarrow {}^7F_{0,2,4}$) are forbidden. For the most cases, the local symmetry of the Eu^{3+} activators does not have an inversion center, thus the parity forbidden is partially permitted. Subsequently, if Eu^{3+} ions occupy the inversion center sites, the $^5D_0 \rightarrow {}^7F_1$ transition should be relatively strong, while the $^5D_0 \rightarrow {}^7F_2$ transition is parity forbidden and should be very weak. Moreover, a more distorted lattice is inevitably associated with a lower symmetry of the crystal field, and will be of

benefit to the $^5D_0 \rightarrow {}^7F_2$ emission [177]. The ratio of the red emission at 610 nm to the orange emission at 591 nm (**R_2/O**) and the percentage fraction of the emission of $^5D_0 \rightarrow {}^7F_4$ transition (integral of 680-720 nm range) with respect to the whole Eu^{3+} emission spectrum (integral of 570-720 nm range) (**Em_4**) are given in Table 6.

Table 6. Luminescence properties of Eu^{3+}-doped garnet powders and crystals excited at 394 nm.

Sample	R_2/O	Em_4 [%]
YAG:5%Eu^{3+} (1500 °C)	0.59	38.1%
YAG:5%Eu^{3+} (@ 100% Ar)	0.52	36.9%
YAG:30%Eu^{3+} (1500 °C)	0.55	39.8%
YAG:30%Eu^{3+} (@ 99% Ar and 1% O_2)	0.56	44.7%
YGG:5%Eu^{3+} (1500 °C)	0.70	40.4%
YGG:5%Eu^{3+} (@ 100% Ar)	0.77	37.7%
YGG:30%Eu^{3+} (1500 °C)	0.84	41.7%
YGG:30%Eu^{3+} (@ 100% Ar)	1.13	42.6%

The powder sheets process rather large surface area and high surface energy, which would not only form the main impetus for assembly but also result in high degree of disorder and correspond to lower symmetry of the crystal field around Eu^{3+} ions. A lower symmetry of the crystal field will result in a higher R_2/O value [159]. It was expected that the R_2/O value would be higher in the precursor powder than in the crystals. However the red-orange emission ratio only slightly differ between YAG:Eu powders and crystal. The R_2/O is even faintly increases after the growth of YAG:30%Eu^{3+}. This could be associated with the impurity phase which remains in the compound and cause the defect in the crystal.

The percentage fraction of the emission of $^5D_0 \rightarrow {}^7F_4$ transitions with respect to the whole Eu^{3+} emission spectrum shows that 5% europium doped YAG and YGG powders exhibit the more red emission than the crystals (Table 6). If europium concentration is increased, the situation is opposite. The 30% europium doped YAG and YGG crystals emit more red light than the powders (Em_4 is 39.8 or 41.7 and 44.7 or 42.2, respectively). The different quenching concentration pre-exists for powders and crystals. The concentration quenching effect involves the possible nonradiative transfer between neighbouring Eu^{3+}

ions, which increases the mobility of the excited state within the host matrix and therefore increases the probability of nonradiative de-excitation via quenching centers-traps. If the concentration of luminescent centers increases, quenching occurs first in particles containing many traps, while those particles containing few or no traps quench only at high concentration or do not quench at all. Therefore, quenching occurs at higher europium concentration in smaller particles [177]. Recently, Kalesnikov *et al.* [178] have published the paper demonstrating that the same quenching concentration but different affect is observed for $^5D_0 \rightarrow {}^7F_2$ and $^5D_0 \rightarrow {}^7F_4$ transitions in YAG:Eu^{3+}. Nevertheless, the optimal concentration for the Em_4 of europium should be investigated.

Figure 31 demonstrates the dependence of Em_4 on the R_4/R_2 and R_4/O.

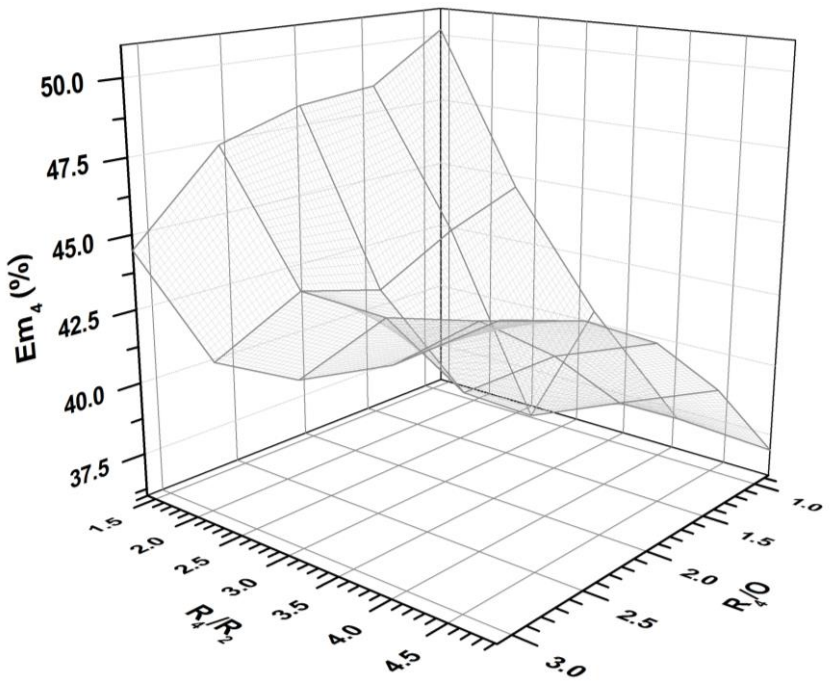

Fig. 31. Em_4 dependence on R_4/R_2 and R_4/O.

The R_4/R_2 is a ratio of the red emission at ~710 nm to the orange emission at 591 nm. The R_4/O is a ratio of the red emission at ~710 nm to the red emission at 610 nm. The results implies that low intensities of the peaks of $^5D_0 \rightarrow {}^7F_1$ and $^5D_0 \rightarrow {}^7F_2$ transitions compared with the intensity of the $^5D_0 \rightarrow {}^7F_4$ transitions do not guarantee the high yield of Em_4 due to the very low multiplicity of the peaks. To conclude, the more detailed investigation of the structure is needed,

because the highest Em_4 value is obtained if all peaks of $^5D_0 \rightarrow {}^7F_{1,2,4}$ transitions are relatively high.

3.3.3. Correlation between the Structure and the Luminescence Properties

The europium doped Y-Al-Ga-O system described in section 3.3.2. has been chosen for the neutron diffraction study. Moreover, the new 8 compounds having $Y_3Al_{5-x}In_xO_{12}$:1%Eu^{3+} (x = 0.5, 1.25 and 1.75), $Y_3Ga_{5-x}In_xO_{12}$:1%Eu^{3+} (x = 0.5, 1.25 and 1.75), YIG and $Y_3Al_{2.5}Fe_{2.5}O_{12}$ have been additionally synthesized in order to discuss in details the relationship between the structure and/or luminescence properties. Figure 32 gives XRD patterns of newly synthesized samples by sol-gel method after annealing at 1500 °C. The pure garnet phase of the Y-Al-In-O system was obtained if indium content was 0.5. With the increase of indium, the secondary phases of $YAlO_3$ and/or EuO appear. The final products of Y-Ga-In-O systems are the pure garnets since each peak is in good agreement with the reference data. The XRD patterns of YIG and $Y_3Al_{2.5}Fe_{2.5}O_{12}$ are not given, but the data showed that the pure garnets were obtained.

The crystal structures were refined by the Rietveld profile method in combination of 1.8857 Å and 1.49369 Å neutron wavelength data with the use of Fullprof program. The reflections of garnets were indexed in the space group Ia3d. The effect of the sample holder was also taken to the account. The reflections of vanadium were indexed in the space group Im3m. The assumed peak shape corresponded to the Thompson-Coxt-Hastings pseudo-Voigt function. In the last cycle of the refinement a total of 52-55 parameters were varied: scale, displacement and transparency factors, 12 polynomial background points, three free coordinates of the oxygen anion, shorter neutron wavelength, zero point, three parameters for the halfwidths description, a lattice constant parameter, one shape parameter and four individual anisotropic thermal parameter. The additional parameters for the occupancy of atoms at 24d and 16a positions also have been introduced for the mixed-metal garnets. Note, europium

highly absorbs neutrons, therefore europium content was fixed to 0.03 in each sample.

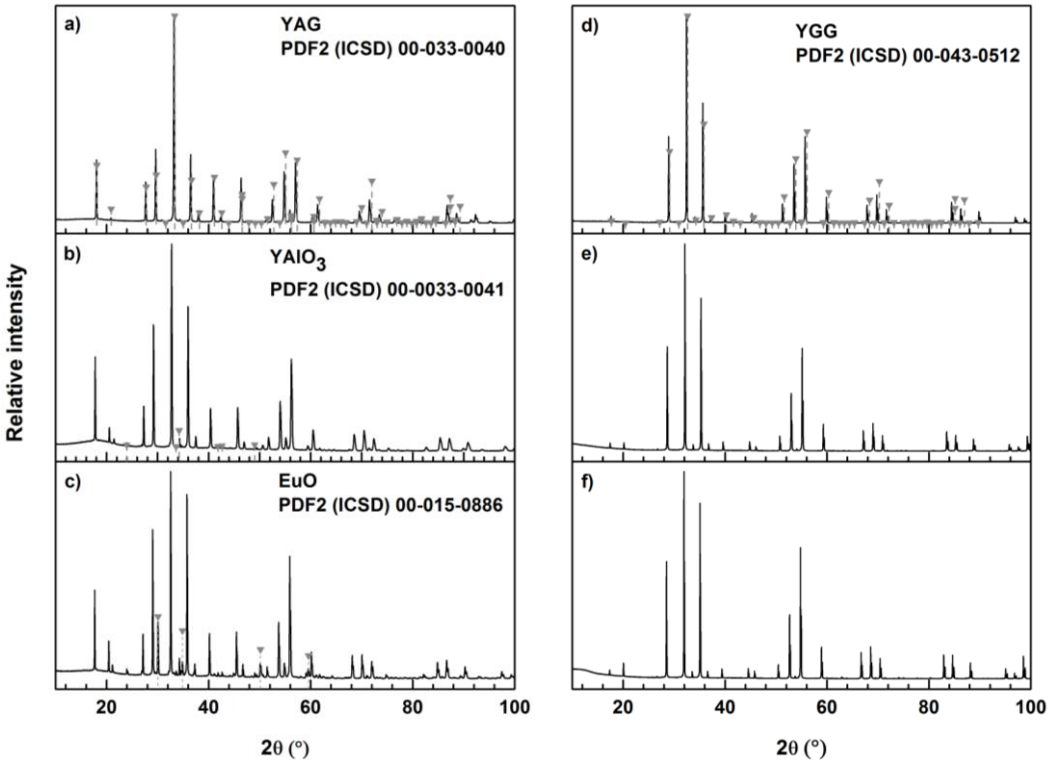

Fig. 32. XRD patterns of (a) $Y_3Al_{4.5}In_{0.5}O_{12}$:1%$Eu^{3+}$, (b) $Y_3Al_{3.75}In_{1.25}O_{12}$:1%$Eu^{3+}$, (c) $Y_3Al_{3.25}In_{1.75}O_{12}$:1%$Eu^{3+}$, (d) $Y_3Ga_{4.5}In_{0.5}O_{12}$:1%$Eu^{3+}$, (e) $Y_3Ga_{3.75}In_{1.25}O_{12}$:1%$Eu^{3+}$ and (f) $Y_3Ga_{3.25}In_{1.75}O_{12}$:1%$Eu^{3+}$.

Figure 33 represents the dependence of the refined lattice constant as the function of x in europium doped $Y_3A_{5-x}B_xO_{12}$. All garnet systems follow the Vegard's law stating the lattice parameter increases linearly as a function of the concentration of the constituent elements, while Nakatsuka *et al.* [29] and Rodic *et al.* [30] observed large deviation from Vegard's law in $Y_3Al_{5-x}Ga_5O_{12}$ and $Y_3Al_{5-x}Fe_xO_{12}$, respectively.

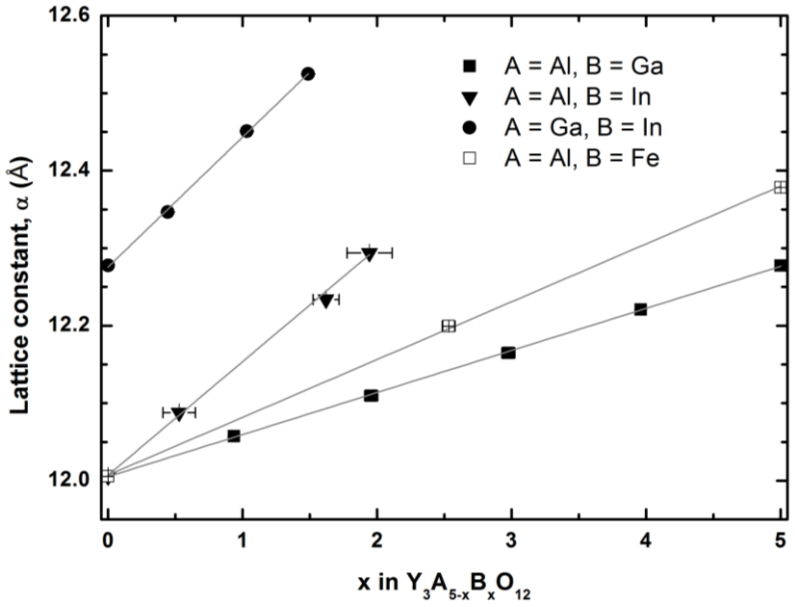

Fig. 33. $Y_3A_{5-x}B_xO_{12}$ lattice parameter as a function of x.

Concerning the general garnet formula $[A_{1-p}B_p]_2(A_{(3-x+2p/3}B_{(x-2p)/3})_3O_{12}$, the fractional parameter f_{Ga} corresponding to the degree of Ga preference for the tetrahedral site is defined by f_{Ga} = 1-(2p/x) [29]. If f_{Ga} = 0.6 (p = 2x), the ions are distributed without any site preference on both the tetrahedral an octahedral sites, because the cation ratio between octahedral and tetrahedral sites is 2:3. The f_{Ga} values are much larger than 0.6 for all compositions, thus gallium ion preferentially enters tetrahedral sites in YAG-YGG system (Figure 34). It is obvious that the higher degree of freedom for the cation to choose the site among the tetrahedral and octahedral sites, more gallium occupies the tetrahedral site, contrary to the effect of cation size. The present f_{Ga} values are much smaller than the results of Marezio *et.al.* [179] and Nakatsuka *et al.* [29].

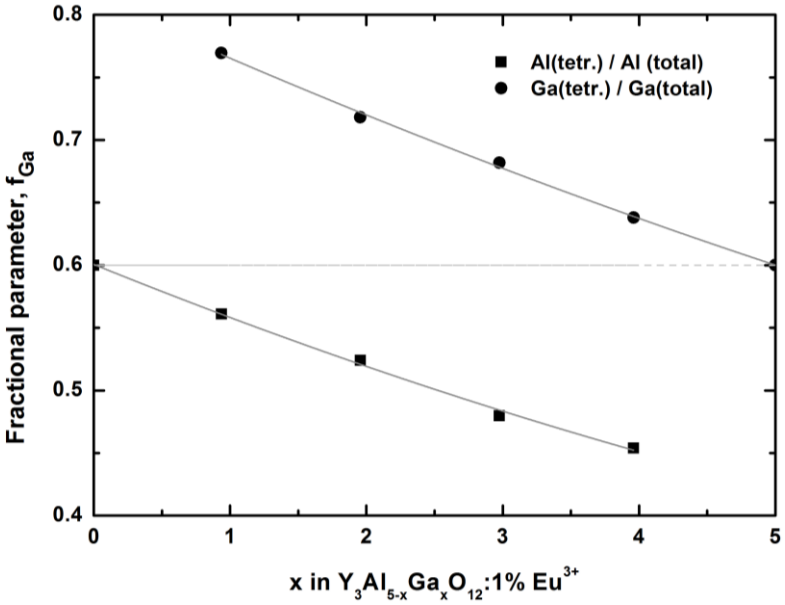

Fig. 34. Preferred site occupation of Al^{3+} and Ga^{3+} among tetrahedral and octahedral sites.

The mismatches could arise due to the different radiation source used for the diffraction. In the previous study, XRD was used to determine the structure. The neutrons interact with the atomic nucleus and not with the electrons as photons do. This has important consequences: the response of neutrons from light atoms is much higher than for X-rays. And neutrons also easily distinguish atoms of comparable atomic number. Therefore, the values obtained by neutron diffraction data are expected to be more accurate. Moreover, the iron ion preferentially occupies octahedral sites in YAG-YIG, while the indium ion takes only octahedral sites in YAInG and YGInG, indicating compliance with limiting radius theory. The refined formula representing preferred position of cations among tetrahedral and octahedral sites are given in Table 7.

Note, that the refined structure perfectly matches the synthesized composition formula for Y-Al-Ga-O and Y-Al-Fe-O systems, while rather high mismatches between theoretical and practical composition are observed for compositions containing indium. The incongruities for the Y-Al-In-O system could be explained by the formation of the secondary phases resulting different ratio of aluminium to indium in the garnet compared with the initial values. The variation of refined and initial ratio of gallium to indium have no explanation, since all peaks have been attributed to the garnet phase in XRD patterns.

Table 7. Synthesized composition and refined formula.

$Y_{3-y}Eu_yA_{5-x}B_xO_{12}$	x	Refined x	Refined Formula
A = Al	0	-	$Y_{2.97}Eu_{0.03}Al_2Al_3O_{12}$
A = Al, B = Ga	1	0.94(5)	$Y_{2.97}Eu_{0.03}(Al_{0.89}Ga_{0.11})_2[Al_{0.76}Ga_{0.24}]_3O_{12}$
A = Al, B = Ga	2	1.95(5)	$Y_{2.97}Eu_{0.03}(Al_{0.72}Ga_{0.28})_2[Al_{0.53}Ga_{0.47}]_3O_{12}$
A = Al, B = Ga	3	2.97(5)	$Y_{2.97}Eu_{0.03}(Al_{0.53}Ga_{0.47})_2[Al_{0.32}Ga_{0.68}]_3O_{12}$
A = Al, B = Ga	4	3.97(4)	$Y_{2.97}Eu_{0.03}(Al_{0.28}Ga_{0.72})_2\ [Al_{0.16}Ga_{0.84}]_3O_{12}$
B = Ga	5	-	$Y_{2.97}Eu_{0.03}Ga_3Ga_2O_{12}$
A = Al, B = In	0.5	0.53(12)	$Y_{2.97}Eu_{0.03}(Al_{0.71}In_{0.26})_2[Al]_3O_{12}$
A = Al, B = In	1.25	1.62(10)	$Y_{2.97}Eu_{0.03}(Al_{0.19}In_{0.81})_2[Al]_3O_{12}$
A = Al, B = In	1.75	1.94(17)	$Y_{2.97}Eu_{0.03}(Al_{0.03}In_{0.97})_2[Al]_3O_{12}$
A = Ga, B = In	0.5	0.44(2)	$Y_{2.97}Eu_{0.03}(Ga_{0.78}In_{0.22})_2[Ga]_3O_{12}$
A = Ga, B = In	1.25	1.03(2)	$Y_{2.97}Eu_{0.03}(Ga_{0.49}In_{0.51})_2[Ga]_3O_{12}$
A = Ga, B = In	1.75	1.49(2)	$Y_{2.97}Eu_{0.03}(Ga_{0.26}In_{0.74})_2[Ga]_3O_{12}$
A = Al, B = Fe	2.5	2.54(2)	$Y_3(Al_{0.33}Fe_{0.67})_2[Al_{0.60}Fe_{0.40}]_3O_{12}$
B = Fe	5	-	$Y_3Fe_3Fe_2O_{12}$

Figure 35 and Figure 36 shows the variation of the interatomic distances and the length of shared-unshared edges with the composition (x).

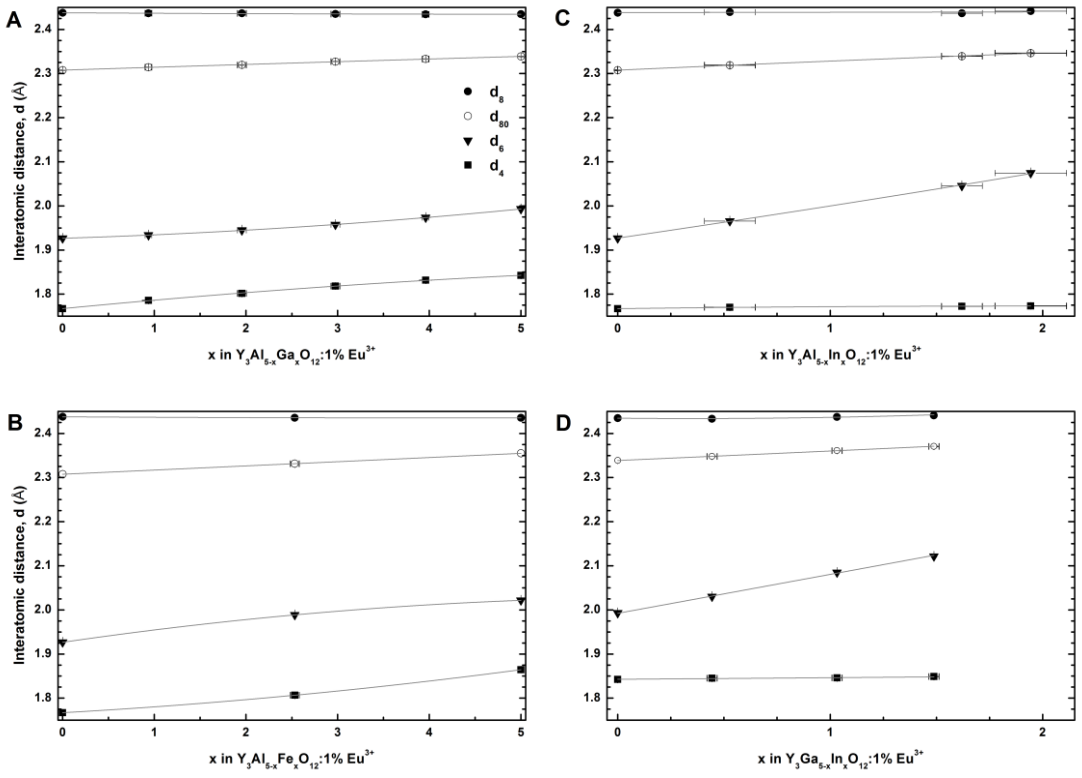

Fig. 35. Interatomic distances of different garnets: (A) $Y_3Al_{5-x}Ga_xO_{12}:Eu^{3+}$, (B) $Y_3Al_{5-x}Fe_xO_{12}:Eu^{3+}$, (C) $Y_3Al_{5-x}In_xO_{12}:Eu^{3+}$ and (D) $Y_3Ga_{5-x}In_xO_{12}:Eu^{3+}$.

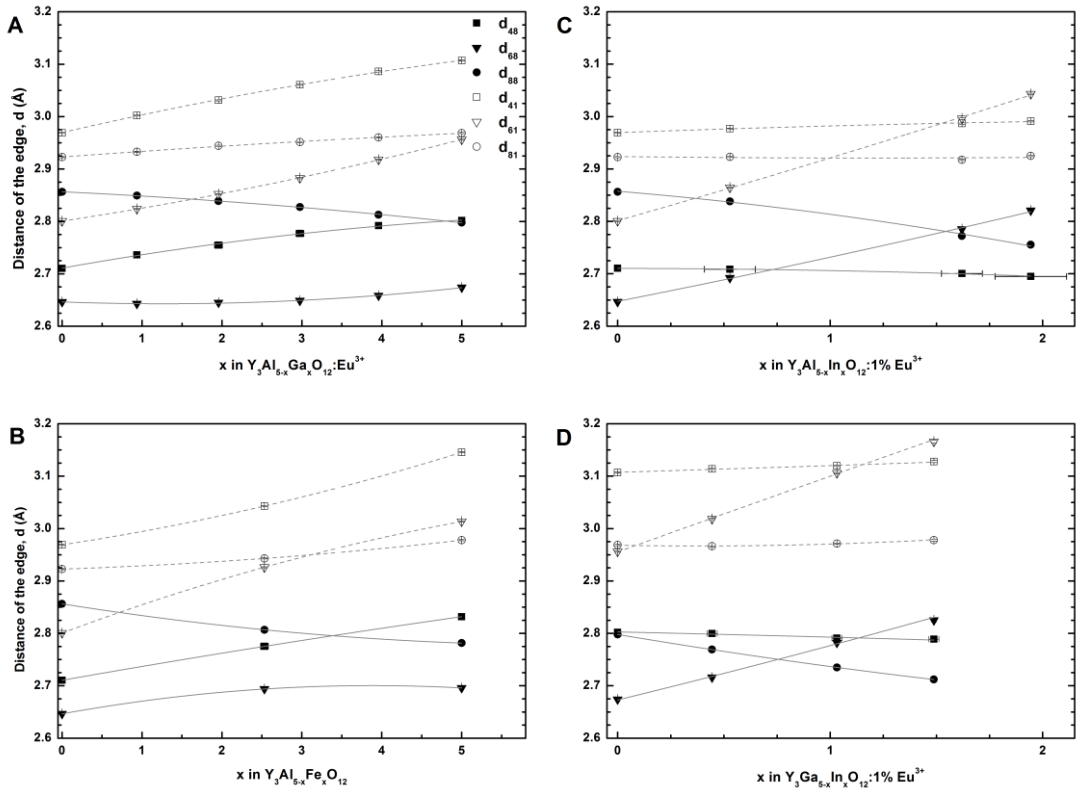

Fig. 36. Shared and unshared edges of different garnets: (A) $Y_3Al_{5-x}Ga_xO_{12}:Eu^{3+}$, (B) $Y_3Al_{5-x}Fe_xO_{12}:Eu^{3+}$, (C) $Y_3Al_{5-x}In_xO_{12}:Eu^{3+}$ and (D) $Y_3Ga_{5-x}In_xO_{12}:Eu^{3+}$.

If the content of x is increased, the interatomic distance d_8 is almost constant in all systems while the value of d_{80} gradually enhances (see Fig. 35). This indicates the deformation of eight-coordinated site caused by the displacement of oxygen anions. The distances d_6 enlarge in all garnet systems demonstrating the bond covalence increase, while the d_4 increases only in the YAG-YGG and YAG-YIG and remains almost the same in YAG-YAInG and YGG-YGInG systems. The value of d_4 remains consistent, because according to the limitary radius theory indium is too large for tetrahedral position.

The results in Figure 36 show that shared edge d_{88} gradually decreases with the variation of composition (x) in all garnet systems. Moreover, the shared edge d_{48} also slightly decreases in Y-Al-In-O and Y-Ga-In-O systems, while all unshared edges and shared edge d_{68} are increased in each system. This implies that the shielding effect of the anions forming the polyhedral shared edges, which relaxes the repulsive force between the cations across the shared edges, increases between the cations at dodecahedral position with the composition (x).

It results less interaction between the luminescent centers, while the repulsive force of cations at tetrahedral and octahedral positions is strengthen.

The bonds in the dodecahedral site can be visualized as a distorted cube in which half of the 8 bonds are longer than the other half (Figure 37) [155].

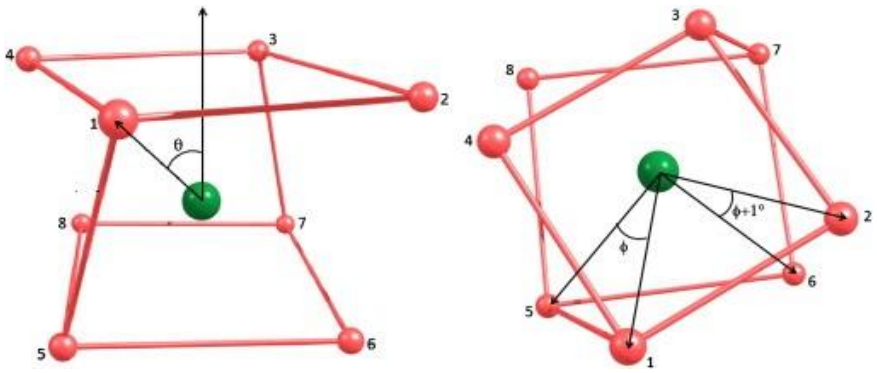

Fig. 37. Schematic representation of the eight-fold cubic coordination of Eu^{3+} in garnets. Oxygen atoms are located at the corners and the Eu^{3+} close to the center of the distorted cube.

These bonds are directly affected by the spatial arrangement of atoms in the tetrahedral and octahedral sites. The deviation from cubic symmetry at the rare-earth site is mainly determined by the compression of the cube, which results in a tetragonal distortion that can be approximately represented as a ratio of the O-O bond distances d_{88} and d_{48} (d_{88}/d_{48}). Decreasing the ratio d_{88}/d_{48} represents a relaxation of the distortion, bringing the polyhedron closer to cubic, while increasing the ratio d_{88}/d_{48} represents a compression of the cube, further distorting it from its idealized structure. Physically, d_{88} represents an O-O bond distance that is shared with an adjacent dodecahedron, while d_{48} represents an O-O bond distance shared with an adjacent tetrahedron (Figure 2).

The d_{88}/d_{48} and Em_4 values are given in Table 8. Wu *et al.* have demonstrated, that emission and excitation in different families of garnets directly correlate to the distortion around the Ce^{3+} ion [180]. It is obvious that the Em_4 parameter is affected not only by the site distortion, since there is no data correlation between different garnet systems. Figure 38 shows that the polarization of d_{48} could directly influence the Em_4. With the increase of d_{48},

Em_4 gradually increase indicating caused by strengthened cation-cation repulsive force.

Table 8. Dependence of d_{88}/d_{48} and Em_4 on chemical composition

Compound	**d_{88}/d_{48}**	**Em_4 (%)**
$Y_3Al_5O_{12}$:1%Eu^{3+}	1.054	39.5
$Y_3Al_4Ga_1O_{12}$:1%Eu^{3+}	1.041	41.6
$Y_3Al_3Ga_2O_{12}$:1%Eu^{3+}	1.030	41.5
$Y_3Al_2Ga_3O_{12}$:1%Eu^{3+}	1.018	43.3
$Y_3Al_1Ga_4O_{12}$:1%Eu^{3+}	1.008	43.4
$Y_3Ga_5O_{12}$:1%Eu^{3+}	0.999	44.6
$Y_3Al_{4.5}In_{0.5}O_{12}$:1%$Eu^{3+}$	1.048	39.8
$Y_3Al_{3.75}In_{1.25}O_{12}$:1%$Eu^{3+}$	1.026	39.5
$Y_3Al_{3.25}In_{1.75}O_{12}$:1%$Eu^{3+}$	1.022	39.1
$Y_3Ga_{4.5}In_{0.5}O_{12}$:1%$Eu^{3+}$	0.989	42.9
$Y_3Ga_{3.75}In_{1.25}O_{12}$:1%$Eu^{3+}$	0.980	42.0
$Y_3Ga_{3.25}Ga_{1.75}O_{12}$:1%$Eu^{3+}$	0.972	41.9

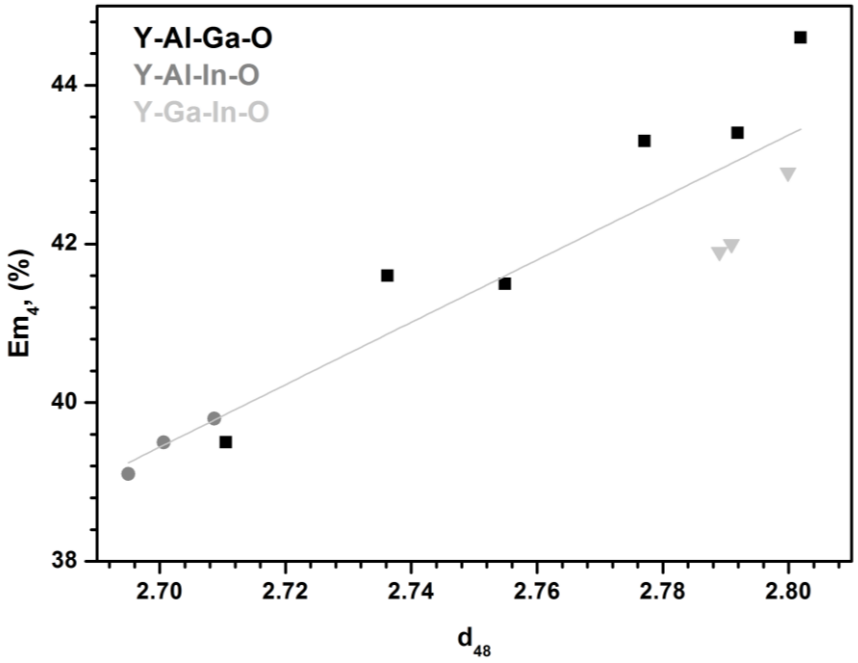

Fig. 38. Em_4 dependence on d_{48}.

CONCLUSIONS

1. The single-phase mixed-metal garnets $Y_3Al_{5-x}M_xO_{12}$ (M = In, Cr, Mn) and $Y_3Ga_{5-x}In_xO_{12}$ synthesized by the sol-gel route were obtained only with narrow substitutional range if aluminium is replaced by indium ($1.75 < x < 2.00$), chromium ($1.00 < x < 1.25$), manganese ($1.00 < x < 1.25$) or gallium is replaced by indium ($2.00 < x < 2.25$) in YAG and YGG, respectively. The substitutional level for aluminium sites is lower in the case of cobalt ($0.25 < x < 0.50$) or nickel ($0.50 < x < 1.00$) and extremely low in the case of copper ($0.10 < x < 0.25$). The yttrium iron-cobalt garnet phase, however, was not obtained at the same conditions. The substitution limit is dependent on ionic radius, major oxidation state and/or characteristic coordination number.
2. It was determined, that the mean cationic radius (limitary radius) at which still formation of garnet phase occurs is in the range of 0.516-0.706 Å. There is no a particular rigid range of limitary radius value for garnet structure compounds. However, the limitary radius could be roughly predicted taking into account the ionic radius, the major oxidation state and the characteristic coordination number of the cations.
3. The sol-gel derived $Y_3(Al,In)_5O_{12}:Ln^{3+}$ (Ln^{3+} = Ce, Eu, Tb or Er) garnets contained In_2O_3 impurity phase, the amount of which increased with increasing indium content. It was demonstrated for the first time, that the replacement of aluminium by indium leads to weaker emission of cerium or europium doped phosphors and extremely drop of the emission of terbium doped mixed-metal garnet, while the emission of erbium doped products slightly increases. In addition, the substitution causes the blue-shift of Eu^{3+}-O^{2-} charge-transfer in $Y_3(Al,In)_5O_{12}:Eu^{3+}$.
4. The luminescence properties of $Y_3(Al,In)_5O_{12}:Ln^{3+}$ garnets was found to be dependent on the amount of lanthanide. With increasing of Ln^{3+} content the intensity of the broad band emission at 530 nm corresponding to $[Xe]5d^1 \rightarrow [Xe]4f^1$ transitions of Ce^{3+} ions decreased in

$Y_3(Al,In)_5O_{12}:Ce^{3+}$. The peaks at 580-600 nm, 600-640 nm, 640-660 and 690-715 nm attributed to the $^5D_0 \rightarrow {}^7F_1$, $^5D_0 \rightarrow {}^7F_2$, $^5D_0 \rightarrow {}^7F_3$ and $^5D_0 \rightarrow {}^7F_4$ transitions, respectively, slightly enhanced in $Y_3(Al,In)_5O_{12}:Eu^{3+}$. The different emission peaks corresponding to $^5D_4 \rightarrow {}^7F_6$ (at 480-510 nm, blue region), $^5D_4 \rightarrow {}^7F_5$ (at 535-565 nm, green region), $^5D_4 \rightarrow {}^7F_4$ and $^5D_4 \rightarrow {}^7F_3$ (at 580-610 nm and 610-635 nm, red region) transitions increased in $Y_3(Al,In)_5O_{12}:Tb^{3+}$. The peaks corresponding to $^4S_{3/2} \rightarrow {}^4I_{15/2}$ transitions at 530-580 nm irregularly varied in $Y_3(Al,In)_5O_{12}:Tb^{3+}$.

5. The luminescence of lanthanides is completely quenched in $Y_3Al_{4.5}Cr_{0.5}O_{12}:Ln^{3+}$, while the excitation and emission peaks caused by Cr^{3+} transitions are dominating. The emission of $Y_3Al_{4.5}Cr_{0.5}O_{12}:Ln^{3+}$ (Ln^{3+} = Tb^{3+}, Eu^{3+}, Ce^{3+} or Er^{3+}) samples was observed in the far-red region. The most intense sharp line at 688.5 nm corresponds to the $^2E_4 \rightarrow {}^4A_2$ transitions. The enhanced emission of Cr^{3+} in the terbium-chromium co-doped $Y_3Al_5O_{12}$ could be associated to the efficient energy transfer from Tb^{3+} to Cr^{3+} ions.
6. The transitions of $^5D_0 \rightarrow {}^7F_4$ is dominant in europium doped garnets. The percentage fraction of the emission of $^5D_0 \rightarrow {}^7F_4$ transition (integral of 680-720 nm range) with respect to the whole Eu^{3+} emission spectrum (integral of 570-720 nm range)(Em_4) increases with the increasing average electronegativity values of M^{3+} ions in the garnets indicating that polarization of the dodecahedral site reduces the value of Em_4.
7. The pure $Y_3Al_5O_{12}:5\%Eu^{3+}$, $Y_3Ga_5O_{12}:5\%Eu^{3+}$ and $Y_3Ga_5O_{12}:30\%Eu^{3+}$ crystals and impurity phase containing $Y_3Al_5O_{12}:30\%Eu^{3+}$ have been successfully grown by the traveling solvent floating zone method, while the $Y_3Al_{4.5}In_{0.5}O_{12}:5\%Eu^{3+}$ was not obtain under the same conditions due to the indium oxide evaporation.
8. The luminescence spectra of europium doped $Y_3Al_5O_{12}$ and $Y_3Ga_5O_{12}$ precursor powders and crystals are rather similar. The decrease of the intensity and red-shift of the charge-transfer band was observed in the

excitation spectrum of precursor powders. The optimal concentration of europium to obtain the highest value of Em_4 for powders and for crystals should be investigated individually.

9. $Y_3Al_{5-x}In_xO_{12}$:1%Eu^{3+} (x = 0.5, 1.25 and 1.75), $Y_3Ga_{5-x}In_xO_{12}$:1%Eu^{3+} (x = 0.5, 1.25 and 1.75), $Y_3Fe_5O_{12}$ and $Y_3Al_{2.5}Fe_{2.5}O_{12}$ compounds follow the Vegard's law: the lattice parameter increases linearly as a function of the concentration of the constituent elements. Moreover, indium or iron ion preferably occupies octahedral site, while gallium ion preferably occupies tetrahedral site, contrary to the effect of the cation size.
10. The refinement of neutron diffraction data demonstrated that interatomic distances gradually increase with composition (x), though the d_4 distance in $Y_3(Al,In)_5$:1%Eu^{3+} and $Y_3(Al,In)_5$:1%Eu^{3+} remains consistent, because indium ionic radius is too large for tetrahedral position. The analysis of shared-unshared edges showed that the shielding effect of the anions forming the polyhedral shared edges increases between the cations at dodecahedral position with the composition (x) resulting less interaction between the luminescent centers, while the repulsive force of cations at tetrahedral and octahedral positions is strengthen.
11. The calculated deviation from cubic symmetry at the eight-coordinated site shows that with more distorted cube the Em_4 decreases in $Y_3Al_5O_{12}$-$Y_3Ga_5O_{12}$ system. This is in a good agreement with the data of the Em_4 dependence on the average electronegativity values of M^{3+} ions. However, other effect such as cation-cation repulsive force between eight-coordinated and four-coordinated cations should be taken into the account on purpose to describe Em_4.
12. Europium doped garnets are the promising compound for optical imaging or NIR-laser application do to the highly expressed emission of $^5D_0 \rightarrow {}^7F_4$ transitions and long life time (ms range).

ACKNOWLEDGEMENTS

I wish to express my sincere gratitude to Prof. Aivaras Kareiva for the invitation to Sol-Gel group and leading me all last 10 years. I am thankful for supporting me in each step and for very valuable comments on our manuscripts.

I am very much indebted to Prof. Jiri Pinkas, Prof. Thomas Jüstel and Prof. Christian Rüegg for collaboration, for stimulating discussions and for fruitful help.

I would also like to thank Assoc. Prof. Artūras Katelnikovas for valuable remarks and my first discussion in luminescence.

I give my sincere gratitude to Dr. Denis V. Sheptyakov and Dr. Ekaterina Pomjakushina for the valuable comments and manifold support with crystallography and crystal growth, respectively.

I would like to thank to Dr. Vladimir Pomjakushin, Dr. David Enseling, Artūras Akelis and Martynas Misevicius for technical assistance.

I am grateful for the Lithuanian Ministry Education and Science Scholarship administered through the Ministry of Education, Youth and Sport of the Czech Republic. J. Pinkas gratefully acknowledges the financial support by the GACR 203/04/0296 and the Ministry of Education of the Czech Republic (MSM0021622410). I am also thankful for the Sciex-NMSch and DAAD Fellowships to stay at Paul Scherrer Institute and Muenster University of Applied Sciences, respectively.

I wish to thank all my colleagues from Sol-Gel chemistry group at Vilnius University, from Laboratory of Neutron Scattering and Imaging at PSI and from Group Tailored Optical Materials for their kind hospitality. Sorry, I can not name, but I remember everyone!

Finally, I thank my family members for their love and help, for not losing their patience during the last half year.

LIST OF PUBLICATIONS

Articles in journals

1. R. Skaudzius, A. Katelnikovas, D. Enseling, A. Kareiva, T. Juestel. Dependence of the $^5D_0$-$^7F_4$ Transitions of Eu^{3+} on the Local Environment in Phosphates and Garnets. *J. Lumin.*, 147 (2014) 290-294.
2. R. Skaudzius, J. Pinkas, R. Raudonis, A. Selskis, R. Juskenas, A. Kareiva. On the limitary radius of garnet structure compounds $Y_3Al_{5-x}M_xO_{12}$ (M=Cr, Co, Mn, Ni, Cu) and $Y_3Fe_{5-x}Co_xO_{12}$ ($0 \leq x \leq 2.75$) synthesized by sol-gel method. *Mater. Chem. Phys.*,135 (2012) 479-485.
3. R. Skaudzius, A. Selskis, J. Pinkas and A. Kareiva. Synthesis and evolution of crystalline garnet phases in $Y_3Al_{5-x}In_xO_{12}$. *J. Physics: Conf. Series*, **93** (2007) 012003.

Articles in proceedings

1. Articles in proceedingsR. Skaudzius, A. Beganskiene, S. Sakirzanovas, D. Jasaitis and A. Kareiva. Mixed metal garnets $Y_3Al_xM_{5-x}O_{12}$ (M-Ga, In): phase formation peculiarities. Proceedings of 44th Meeting of the Serbian Chemical Society. Belgrad, February 6-7, (2006) 113-116.

Published contributions to academic conferences

1. R. Skaudzius, D.V. Sheptyakov, A. Katelnikovas, D. Enseling, Th. Jüstel, Ch. Rüegg and A. Kareiva. Neutron Diffraction Study and Luminescence Properties of Eu^{3+}-doped $Y_3(Al,Ga)_5O_{12}$, $Y_3(Al,In)_5O_{12}$ and $Y_3(Ga,In)_5O_{12}$. The 14th European Powder Diffraction Conference, Aarhus, Denmark, 15-18 June (2014) 165-166.
2. R. Skaudžius, E. Pomjakushina, Ch. Rüegg, D. Enseling, T. Jüstel and A. Kareiva. Single crystal growth of $Y_3Al_5O_{12}$:Eu^{3+} and $Y_3Ga_5O_{12}$:Eu^{3+} garnets by the traveling solvent floating zone method and its luminescence properties. ”Chemistry and chemical technology” Proceedings of the international conference, Kaunas, Lithuania, April 25, (2014) 57-60.

3. R. Skaudzius, D. V. Sheptyakov, A. Katelnikovas, D. Enseling, A. Kareiva, T. Juestel and Ch. Rueegg. Neutron Diffraction Study and Luminescence Properties of $Y_3(Al,In)_5O_{12}$:1%Eu and $Y_3(Ga,In)_5O_{12}$:1%Eu Compounds. 18th International Scientific Conference "EcoBalt 2013", Vilnius, Lithuania, 25-27 October (2013) 98.
4. R. Skaudžius, E. Pomjakushina, Ch. Rüegg, D. Enseling, T. Jüestel, A. Kareiva. Single Crystal Growth of $Y_3Al_5O_{12}:Eu^{3+}$ by the Traveling Solvent Floating Zone Method and its Luminescence Properties. 11th International Conference of Lithuania's Chemists. Vilnius, Lithuania, 27 September (2013) P43.
5. R. Skaudzius, A. Akelis, A. Katelnikovas, I. Bogdanoviciene, T. Juestel, D. V. Sheptyakov, Ch. Rueegg and A. Kareiva. Synthesis of Mixed-Metal Garnets and their Study by Neutron Diffraction. International Conference on Neutron Scattering. Edinburgh, UK, 8-12 July (2013) P032.
6. R. Skaudzius, A. Katelnikovas and T. Juestel. Luminescent Properties of $MPO_4:Eu^{3+}$ (M = Y, Gd, Lu OR La) Phosphors Synthesized by Solid-State Reaction for Optical Imaging and FTIR Laser Application. International Conference of Young Chemists "Nanochemistry and Nanomaterials". Palanga, Lithuania, 7-9 December (2012) 43.
7. D. Jasaitis, A. Akelis, T. Juestel, A. Kareiva, A. Katelnikovas and R. Skaudzius. Matrix Induced Differences in Luminescence Properties of Lanthanide-Substituted Mixed-Metal $L:Y_3Al_{5-x}M_xO_{12}$ ((M=In, Cr; L=Ce, Eu, Er and Tb; $1.50 \leq x \leq 2.25$) Garnets Synthesized by Sol-Gel Method. International Symposium on Ceramic Materials and Components for Energy and Environmental Applications. Dresden, Germany, 20-23 May (2012) 85
8. R. Skaudzius and A. Kareiva. Synthesis and characterization of lanthanide-doped mixed-metal garnets by sol-gel method. The Seventh Int. Conference on High-Performance Ceramics. Xiamen, China, 4-7 November (2011) 28.
9. R. Skaudzius and A. Kareiva. Matrix induced differences in luminescence properties of lanthanide-doped or lanthanide-substituted mixed-metal garnets

synthesized by sol-gel method. 10th International Conference of Lithuanian Chemists „Chemistry 2011“. Vilnius, Lithuania, 14 October, (2011) 99.

10. R. Skaudzius, J. Pinkas, Z. Moravec, A. Kareiva and D. Jasaitis. Sol-gel synthesis and characterization of new mixed-metal garnets. Int. Symposium on Advanced Complex Inorganic Nanomaterials “ACIN 2011”. Namur, Belgium, 11-14 September (2011) P094.
11. R. Skaudzius, R. Raudonis, A. Beganskiene and A. Kareiva. New mixed-metal garnets as host matrixes for luminescent materials. 16th International Symposium on Intercalation Compounds “ISIC16”. Sec, Czech Republic, May 23-26, (2011) P092.
12. R. Skaudžius, M. Ahlhelm, A. Adam, A. Beganskiene and A. Kareiva. Synthesis and characterization of mixed-metal garnets $Y_3Al_{5-x}In_xO_{12}$ and $Y_3Ga_{5-x}In_xO_{12}$. 9th National Lithuanian Conference „Chemistry 2009“. Vilnius, Lithuania, October 16, (2009) 45.
13. R. Skaudžius and A. Kareiva. Mixed metals garnets $Y_3Al_{5-x}In_xO_{12}$ and $Y_3Ga_{5-x}In_xO_{12}$ synthesis, phases transformation and characterization. Students Conference ”Chemistry and Chemical Technology”. Kaunas University of Technology, Kaunas, Lithuania, 9 May (2008) 108-109 (In Lithuanian).
14. R. Skaudzius, A. Selskis, J. Pinkas and A. Kareiva. Synthesis and evolution of crystalline garnet phases in $Y_3Al_{5-x}In_xO_{12}$. Int. Baltic Sea Region Conf. “Functional Materials and Nanotechnologies 2007”. Riga, Latvia, April 2-4, (2007) 20.
15. R. Skaudžius and A. Kareiva. Synthesis and characterization of yttrium aluminium garnet and phase transformations substituting aluminium by indium. The International Research Conference for Students ”Chemistry and Chemical Technology”. Vilnius University, Vilnius, Lithuania, 27 April (2007) 175-176.
16. R. Skaudzius, S. Sakirzanovas, A. Katelnikovas, A. Beganskiene and A. Kareiva. Spectroscopic evaluation and characterization of different mixed-metal garnets. Conference “European seminar on infrared spectroscopy, ESIS 2006”. Lyon, France, April 4-6, (2006) 57.

17. R. Skaudzius, A. Beganskiene, S. Sakirzanovas, D. Jasaitis and A. Kareiva. Mixed metal garnets $Y_3Al_xM_{5-x}O_{12}$ (M-Ga, In): phase formation peculiarities. Conference "44th Meeting of the Serbian Chemical Society". Belgrad, February 6-7, (2006) 53.

Publications not included in the thesis

1. G. Nenartaviciene, R. Skaudzius, R. Raudonis and A. Kareiva. Synthesis of lead-based 1212 and 3212 superconductors by an aqueous sol-gel method. *Centr. Eur. J. Chem.*, **7** (2009) 362-368.2.
2. R. Skaudzius, A. Zalga and A. Kareiva. Sol-gel synthesis of nanocrystalline $LaAlO_3$-M_2O_3 (M = La, Al) and Nd:$LaAlO_3$-M_2O_3 composite materials via „phase metathesis" route. *Materials Science (Medžiagotyra),* 14 (2008) 193-197.
3. R. Skaudzius, A. Zalga and A. Kareiva. Sol-gel synthesis of nanocrystalline $LaAlO_3$-M_2O_3 (M = La, Al) and Nd:$LaAlO_3$-M_2O_3 composite materials via „phase metathesis" route. 17th International Baltic Conference „Materials Engineering 2008". Kaunas, Lithuania, November 6-7, (2008) 55-56.

REFERENCES

[1] G. Menzer, Z. Kristallogr., 63 (1926) 157-158.

[2] G. Boulon, Opt. Mater., 34 (2012) 499-512.

[3] L.G.D. Silveira, L.F. Cotica, I.A. Santos, M.P. Belançon, J.H. Rohling, M.L. Baesso, Mater. Lett., 89 (2012) 86-89.

[4] C.P. Khattak, F.F.Y. Wang, Handbook on the Physics and Cheimstry on Rare Earth, Elsevier, Amsterdam, 1979.

[5] G. Blasse, B.C. Grabmaier, Luminescent Materials, Springer-Verlag, Berlin, 1994.

[6] K. Riwotzki, M. Haase, J. Phys. Chem. B, 102 (1998) 10129-10135.

[7] C.R. Ronda, J. Lumin., 72-74 (1997) 49-5454.

[8] Z. Shuxiu, IEEE T. Plasma Sci., 34 (2006) 294-304.

[9] X. Huang, S. Han, W. Huang, X. Liu, Chem. Soc. Rev., 42 (2013) 173-201.

[10] J.E. Geusic, H.M. Marcos, L.G. Vanuitert, Appl. Phys. Lett., 4 (1964) 182-184.

[11] A. Katelnikovas, P. Vitta, P. Pobedinskas, G. Tamulaitis, A. Žukauskas, J.E. Jørgensen, A. Kareiva, J. Cryst. Growth, 304 (2007) 361-368.

[12] D. Hreniak, W. Strek, P. Mazur, R. Pazik, M. Zabkowska-Waclawek, Opt. Mater., 26 (2004) 117-121.

[13] R.A. Rodríguez-Rojas, E. De la Rosa-Cruz, L.A. Díaz-Torres, P. Salas, R. Meléndrez, M. Barboza-Flores, M.A. Meneses-Nava, O. Barbosa-García, Opt. Mater., 25 (2004) 285-293.

[14] M. Nishi, S. Tanabe, M. Inoue, M. Takahashi, K. Fujita, K. Hirao, Opt. Mater., 27 (2005) 655-662.

[15] E. Garskaite, M. Lindgren, M.A. Einarsrud, T. Grande, J. Eur. Ceram. Soc., 30 (2010) 1707-1715.

[16] D. Boyer, G. Bertrand-Chadeyron, R. Mahiou, Opt. Mater., 26 (2004) 101-105.

[17] Y.H. Zhou, J. Lin, M. Yu, S.M. Han, S.B. Wang, H.J. Zhang, Mater. Res. Bull., 38 (2003) 1289-1299.

[18] Y.H. Zhou, J. Lin, S.B. Wang, H.J. Zhang, Opt. Mater., 20 (2002) 13-20.
[19] P. Głuchowski, R. Pązik, D. Hreniak, W. Stręk, J. Lumin., 129 (2009) 548-553.
[20] P.F.S. Pereira, M.G. Matos, L.R. Ávila, E.C.O. Nassor, A. Cestari, K.J. Ciuffi, P.S. Calefi, E.J. Nassar, J. Lumin., 130 (2010) 488-493.
[21] E. Taylor, P.R. Edwards, R.W. Martin, Phys. Status Solidi A, 209 (2012) 461-464.
[22] A. Katelnikovas, J. Jurkevičius, K. Kazlauskas, P. Vitta, T. Jüstel, A. Kareiva, A. Žukauskas, G. Tamulaitis, J. All. Compd., 509 (2011) 6247-6251.
[23] A. Zabiliute, S. Butkute, A. Zukauskas, P. Vitta, A. Kareiva, Appl. Opt., 53 (2014) 907-914.
[24] A. Gibson, H. Dehghani, Philos. T. Roy. Soc., 367 (2009) 3055-3072.
[25] I. Muliuoliene, S. Mathur, D. Jasaitis, H. Shen, V. Sivakov, R. Rapalaviciute, A. Beganskiene, A. Kareiva, Opt. Mater., 22 (2003) 241-250.
[26] E. Garskaite, PhD Thesis, Vilnius University, Vilnius, Lithuania (2006).
[27] P. Fischer, W. Hälg, P. Roggwiller, E.R. Czerlinsky, Solid State Commun., 16 (1975) 987-992.
[28] A. Nakatsuka, A. Yoshiasa, S. Takeno, Acta Crystallogr. B, 51 (1995) 737-745.
[29] A. Nakatsuka, A. Yoshiasa, T. Yamanaka, Acta Crystallogr. B, 55 (1999) 266-272.
[30] D. Rodic, M. Mitric, R. Tellgren, H. Rundlof, J. Magn. Magn. Mater., 232 (2001) 1-8.
[31] O.Y. Goncharov, Crystallogr. Rep., 48 (2003) 1-7.
[32] K. Ohno, T. Abe, J. Electrochem. Soc., 133 (1986) 638-643.
[33] W.T. Hsu, W.H. Wu, C.H. Lu, Mater. Sci. Eng. B, 104 (2003) 40-44.
[34] A. Kareiva, Mater. Sci-Medzg., 17 (2011) 428-437.
[35] H.S. Yoder, M.L. Keith, Am. Mineral., 36 (1951) 519-533.
[36] M.L. Keith, R. Roy, Am. Mineral., 39 (1954) 1-23.
[37] F. Bertaut, F. Forrat, Compt. Rend., 242 (1956) 382-283.
[38] S. Geller, M.A. Gilleo, Acta Cryst., 10 (1957) 239-240.

[39] J.W. Nielsen, E.F. Dearborn, J. Phys. Chem. Solids, 5 (1958) 202-207.
[40] J.E. Geusic, H.M. Marcos, L.G. Van Uitert, Appl. Phys. Lett., 4 (1964) 182-184.
[41] S. Geller, Z. Kristallogr., 125 (1967) 1-47.
[42] G.A. Novak, G.V. Gibbs, Am. Mineral., 56 (1971) 791-825.
[43] J.E. Huheey, E.A. Keiter, R.L. Keiter, Inorganic Chemistry: Principles of Structure and Reactivity, HarperCollins College Publishers, New York, 1993.
[44] L.C. Nathan, J. Chem. Educ., 62 (1985), 215-216.
[45] K.Y. Li, D.F. Xue, Chin. Sci. Bull., 54 (2009) 328-334.
[46] K.Y. Li, D.F. Xue, J. Phys. Chem. A, 110 (2006) 11332-11337.
[47] L.H. Ahrens, Geochim. Cosmochim. Acta, 2 (1952) 155-169.
[48] R. Shannon, Acta Crystallogr. A, 32 (1976) 751-767.
[49] M.A. Gilleo, S. Geller, J. Appl. Phys., 29 (1958) 380-381.
[50] R.W. Grant, H. Wiedersich, S. Geller, U. Gonser, G.P. Espinosa, J. Appl. Phys., 38 (1967) 1455-1456.
[51] H.S.C. O'Neill, A. Navrotsky, Am. Mineral., 68 (1983) 181-194.
[52] M.H. Mahmoud, H.H. Hamdeh, J.C. Ho, A.M. Abdalla, A.I. Abdel-Mageed, Solid State Commun., 120 (2001) 451-453.
[53] S.H. Song, C.C.H. Lo, S.J. Lee, S.T. Aldini, J.E. Snyder, D.C. Jiles, J. Appl. Phys., 101 (2007) 517-530.
[54] H. Hemmati, J.R. Lesh, Opt. Lett., 19 (1994) 1322-1324.
[55] S. Konno, K. Yasui, Appl. Opt., 37 (1998) 551-554.
[56] C.X. Wang, G.Y. Wang, A.V. Hicks, D.R. Dudley, H.Y. Pang, N. Hodgson, 6100 (2006) 14-19.
[57] D.R. Dudley, O. Mehl, G.Y. Wang, E.S. Allee, H.Y. Pang, N. Hodgson, Technol. Dev. 7193 (2009) 1-8.
[58] Y. Ma, H. Li, J. Lin, X. Yu, Opt. Laser Technol., 43 (2011) 1491-1494.
[59] S.E. Wang, S.Q. Zhu, Z.Q. Chen, Q.G. Yang, J. Pan, J Russ Laser Res, 34 (2013) 166-167.

[60] J. Liu, B. Ozygus, S. Yang, J. Erhard, U. Seelig, A. Ding, H. Weber, X. Meng, L. Zhu, L. Qin, C. Du, X. Xu, Z. Shao, J. Opt. Soc. Am. B, 20 (2003) 652-661.

[61] D.G. Kochiev, A.M. Prokhorov, A.V. Lukashev, I.A.S. Hcherbakov, S.K. Vartapetov, A.M. Prokhorov, Handbook of Solid-State Lasers, Woodhead Publishing, Sawston, 2013.

[62] S. Duran, M. Zato, J. Cataract Refr. Surg., 27 (2001) 1025-1032.

[63] J.M.H. Teichman, K.F. Chan, P.P. Cecconi, N.S. Corbin, A.D. Kamerer, R.D. Glickman, A.J. Welch, J. Urology, 165 (2001) 876-879.

[64] R. Tooher, P. Sutherland, A. Costello, P. Gilling, G.U.Y. Rees, G.U.Y. Maddern, The Journal of Urology, 171 (2004) 1773-1781.

[65] A.S. Sandhu, A. Srivastava, P. Madhusoodanan, T. Sinha, S.K. Gupta, A. Kumar, G.S. Sethi, R. Khanna, Armed Forces Med. J. India, 63 (2007) 48-51.

[66] E.N. Sobol, A.B. Shekhter, A.V. Baskov, Lasers for Medical Applications, Woodhead Publishing, Sawston, 2013.

[67] D.G. Kochiev, A.M. Prokhorov, A.V. Lukashev, I.A.S. Hcherbakov, S.K. Vartapetov, A.M. Prokhorov, Surgical solid-state lasers and their clinical applications, Woodhead Publishing, Sawston, 2013.

[68] T. Jüstel, H. Nikol, C. Ronda, Angew. Chem. Int. Ed., 37 (1998) 3084-3103.

[69] J. Hou, X. Yin, Y. Fang, F. Huang, W. Jiang, Opt. Mater., 34 (2012) 1394-1397.

[70] C. Sommer, P. Hartmann, P. Pachler, H. Hoschopf, F.P. Wenzl, J. All. Compd., 520 (2012) 146-152.

[71] Q.Y. Zhang, X.Y. Huang, Prog. Mater Sci., 55 (2010) 353-427.

[72] B.M.J. Smets, Mater. Chem. Phys., 16 (1987) 283-299.

[73] C.R. Ronda, J. All. Compd., 225 (1995) 534-538.

[74] C.R. Ronda, J. Lumin., 72 (1997) 49-54.

[75] R.J. Xie, N. Hirosaki, M. Mitomo, K. Sakuma, N. Kimura, Appl. Phys. Lett., 89 (2006) 1-3.

[76] H.S. Jang, D.Y. Jeon, Appl. Phys. Lett., 90 (2007) 5-7.

[77] H. Yamamoto, T. Yamamoto, Phosphors for white LEDs, Woodhead Publishing, Sawston, 2014.

[78] R. Murugan, V. Thangadurai, W. Weppner, Angew. Chem. Int. Ed., 46 (2007) 7778-7781.

[79] R. Murugan, W. Weppner, P. Schmid-Beurmann, V. Thangadurai, Mater. Sci. Eng. B, 143 (2007) 14-20.

[80] S. Ohta, T. Kobayashi, T. Asaoka, J. Power Sources, 196 (2011) 3342-3345.

[81] S. Teng, J. Tan, A. Tiwari, Curr. Opin. Solid State Mater. Sci., 18 (2014) 29-38.

[82] A.S. Hudson, Rev. Phys. Techn., 1 (1970) 9-10.

[83] M. Pardavi-Horvath, J. Magn. Magn. Mater., 215–216 (2000) 171-183.

[84] Q. Yang, H. Zhang, Y. Liu, Q. Wen, L. Jia, Mater. Lett., 62 (2008) 2647-2650.

[85] K. Praveena, S. Srinath, J. Magn. Magn. Mater., 349 (2014) 45-50.

[86] F. Grasset, S. Mornet, A. Demourgues, J. Portier, J. Bonnet, A. Vekris, E. Duguet, J. Magn. Magn. Mater., 234 (2001) 409-418.

[87] S. Chandra, K.C. Barick, D. Bahadur, Adv. Drug Deliver. Rev., 63 (2011) 1267-1281.

[88] M.-S. Tsai, W.-C. Fu, W.-C. Wu, C.-H. Chen, C.-H. Yang, J. All. Compd., 455 (2008) 461-464.

[89] J.J. Kingsley, L.R. Pederson, MRS Proc., 296 (1992) 1-3.

[90] J. McKittrick, L.E. Shea, C.F. Bacalski, E.J. Bosze, Displays, 19 (1999) 169-172.

[91] M.B. Kakade, S. Ramanathan, P.V. Ravindran, J. All. Compd., 350 (2003) 123-129.

[92] Y. Liao, D. Jiang, T. Feng, J. Shi, J. Mater. Res., 20 (2005) 2934-2939.

[93] S. Hosseini Vajargah, H.R. Madaah Hosseini, Z.A. Nemati, Mater. Sci. Eng. B, 129 (2006) 211-215.

[94] H. Li, X. Liu, Q. Zhang, L. Huang, J. Rare Earth., 25 (2007) 401-406.

[95] K. Guo, H.H. Chen, X. Guo, X.X. Yang, F.F. Xu, J.T. Zhao, J. All. Compd., 500 (2010) 34-38.

[96] L. Zhang, Z. Lu, J. Zhu, H. Yang, P. Han, Y. Chen, Q. Zhang, J. Rare Earth., 30 (2012) 289-296.
[97] A. Leleckaite, A. Kareiva, Opt. Mater., 26 (2004) 123-128.
[98] P. Vaqueiro, M. Arturo Lopez-quintela, J. Mater. Chem., 8 (1998) 161-163.
[99] M. Veith, S. Mathur, A. Kareiva, M. Jilavi, M. Zimmer, V. Huch, J. Mater. Chem., 9 (1999) 3069-3079.
[100] K. Blazek, A. Krasnikov, K. Nejezchleb, M. Nikl, T. Savikhina, S. Zazubovich, Phys. Status Solidi B, 241 (2004) 1134-1140.
[101] E. Garskaite, N. Dubnikova, A. Katelnikovas, J. Pinkas, A. Kareiva, Collect. Czech. Chem. Commun., 72 (2007) 321-333.
[102] S. Saxena, A. Asokkumar K, B. Lal, J. Sol-Gel Sci. Technol., 41 (2007) 245-248.
[103] N. Dubnikova, E. Garskaite, J. Pinkas, P. Bezdicka, A. Beganskiene, A. Kareiva, J. Sol-Gel Sci. Technol., 55 (2010) 213-219.
[104] N. Dubnikova, E. Garskaite, A. Beganskiene, A. Kareiva, Opt. Mater., 33 (2011) 1179-1184.
[105] E. Garskaite, S. Sakirzanovas, A. Kareiva, J. Glaser, H.J. Meyer, Z. Anorg. Allg. Chem., 633 (2007) 990-993.
[106] K. Matsumoto, K. Yamaguchi, T. Fujii, A. Ueno, J. Appl. Phys., 69 (1991) 5918-5920.
[107] P. Vaqueiro, M.A. López-Quintela, Chem. Mater., 9 (1997) 2836-2841.
[108] R.D. Sanchez, J. Rivas, P. Vaqueiro, M.A. Lopez-Quintela, D. Caeiro, J. Magn. Magn. Mater., 247 (2002) 92-98.
[109] S. Hosseini Vajargah, H.R. Madaah Hosseini, Z.A. Nemati, Mat. Sci. Eng. B, 129 (2006) 211-215.
[110] E. Garskaite, K. Gibson, A. Leleckaite, J. Glaser, D. Niznansky, A. Kareiva, H.J. Meyer, Chem. Phys., 323 (2006) 204-210.
[111] E. Garskaite, Z. Moravec, J. Pinkas, S. Mathur, R. Kazlauskas, A. Kareiva, Philos. Mag. Lett., 85 (2005) 557-562.
[112] I. Muliuoliene, D. Jasaitis, A. Kareiva, B. Blaschkowski, J. Glaser, H.J. Meyer, J. Mater. Sci. Lett., 22 (2003) 349-351.

[113] A. Katelnikovas, H. Bettentrup, D. Uhlich, S. Sakirzanovas, T. Jüstel, A. Kareiva, J. Lumin., 129 (2009) 1356-1361.
[114] A. Katelnikovas, T. Bareika, P. Vitta, T. Jüstel, H. Winkler, A. Kareiva, A. Žukauskas, G. Tamulaitis, Opt. Mater., 32 (2010) 1261-1265.
[115] A. Katelnikovas, H. Winkler, A. Kareiva, T. Jüstel, Opt. Mater., 33 (2011) 992-995.
[116] A. Katelnikovas, H. Bettentrup, D. Dutczak, A. Kareiva, T. Jüstel, J. Lumin., 131 (2011) 2754-2761.
[117] A. Katelnikovas, J.M. Ogiegło, H. Winkler, A. Kareiva, T. Jüstel, J. Sol-Gel Sci. Technol., 59 (2011) 311-314.
[118] A. Katelnikovas, J. Plewa, D. Dutczak, S. Möller, D. Enseling, H. Winkler, A. Kareiva, T. Jüstel, Opt. Mater., 34 (2012) 1195-1201.
[119] Y. Sang, H. Liu, X. Sun, X. Zhang, H. Qin, Y. Lv, D. Huo, D. Liu, J. Wang, R.I. Boughton, J. All. Compd., 509 (2011) 2407-2413.
[120] J.G. Li, T. Ikegami, J.H. Lee, T. Mori, Y. Yajima, J. Eur. Ceram. Soc., 20 (2000) 2395-2405.
[121] J.G. Li, T. Ikegami, J.-H. Lee, T. Mori, Y. Yajima, J. Eur. Ceram. Soc., 20 (2000) 2395-2405.
[122] C. Marlot, E. Barraud, S. Le Gallet, M. Eichhorn, F. Bernard, J. Solid State Chem., 191 (2012) 114-120.
[123] J. Li, F. Chen, W. Liu, W. Zhang, L. Wang, X. Ba, Y. Zhu, Y. Pan, J. Guo, J. Eur. Ceram. Soc., 32 (2012) 2971-2979.
[124] S. Feng, L. Guanghua, Modern Inorganic Synthetic Chemistry, Elsevier, Amsterdam, 2011.
[125] Y. Hakuta, T. Haganuma, K. Sue, T. Adschiri, K. Arai, Mater. Res. Bull., 38 (2003) 1257-1265.
[126] H. Yang, L. Yuan, G. Zhu, A. Yu, H. Xu, Mater. Lett., 63 (2009) 2271-2273.
[127] B. Huang, Y. Ma, S. Qian, D. Zou, G. Zheng, Z. Dai, Opt. Mater., 36 (2014) 1561-1565.

[128] X. Li, H. Liu, J. Wang, H. Cui, F. Han, Mater. Res. Bull., 39 (2004) 1923-1930.
[129] Z. Wu, X. Zhang, W. He, Y. Du, N. Jia, P. Liu, F. Bu, J. All. Compd., 472 (2009) 576-580.
[130] L. Xing, L. Peng, M. Gu, G. Tang, J. All. Compd., 491 (2010) 599-604.
[131] J.Y. Park, H.C. Jung, G.S.R. Raju, J.H. Jeong, B.K. Moon, J.H. Kim, Y.K. Lee, Curr. Appl. Phys., 13 (2013) 441-447.
[132] Z. Frukacz, D.A. Pawlak, Encyclopedia of Materials: Science and Technology, Elsevier, Oxford, 2001.
[133] H. Kimura, A. Miyazaki, J. Cryst. Growth, 250 (2003) 251-255.
[134] E. Kanchanavaleerat, D. Cochet-Muchy, M. Kokta, J. Stone-Sundberg, P. Sarkies, J. Sarkies, J. Sarkies, Opt. Mater., 26 (2004) 337-341.
[135] W.D. Xiang, B.Y. Zhao, X.J. Liang, Z.P. Chen, C.P. Xie, L. Luo, Z.M. Zhang, J.F. Zhang, J.S. Zhong, J. Inorg.Mat., 29 (2014) 614-620.
[136] Y. Yu, Z. Wu, S. Zhang, J. All. Compd., 302 (2000) 204-208.
[137] X. Xu, Z. Zhao, P. Song, G. Zhou, J. Xu, P. Deng, J. Opt. Soc. Am. B: Opt. Phys., 21 (2004) 543-547.
[138] P. Peshev, V. Petrov, N. Manuilov, Mater. Res. Bull., 23 (1988) 1193-1198.
[139] D. Petrova, O. Pavloff, P. Marinov, J. Cryst. Growth, 99 (1990) 841-844.
[140] A.G. Petrosyan, K.L. Ovanesyan, R.V. Sargsyan, G.O. Shirinyan, D. Abler, E. Auffray, P. Lecoq, C. Dujardin, C. Pedrini, J. Cryst. Growth, 312 (2010) 3136-3142.
[141] I. Shindo, N. Ii, K. Kitamura, S. Kimura, J. Cryst. Growth, 46 (1979) 307-313.
[142] S. Kimura, K. Kitamura, I. Shindo, J. Cryst. Growth, 65 (1983) 543-548.
[143] E. Kita, S. Takano, K. Kohn, K. Siratori, S. Kimura, A. Tasaki, J. Magn. Magn. Mater., 104–107, Part 1 (1992) 449-450.
[144] K. Wu, B. Yao, H. Zhang, H. Yu, Z. Wang, J. Wang, M. Jiang, J. Cryst. Growth, 312 (2010) 3631-3636.

[145] A. Yoshikawa, Y. Fujimoto, A. Yamaji, S. Kurosawa, J. Pejchal, M. Sugiyama, S. Wakahara, Y. Futami, Y. Yokota, K. Kamada, K. Yubuta, T. Shishido, M. Nikl, Opt. Mater., 35 (2013) 1882-1886.
[146] L. Tian, S. Wang, K. Wu, B. Wang, H. Yu, H. Zhang, H. Cai, H. Huang, Opt. Mater., 36 (2013) 521-528.
[147] M.D. Sturge, S.L. Blank, R. Wolfe, Mater. Res. Bull., 7 (1972) 989-997.
[148] Y. Zorenko, V. Gorbenko, V. Savchyn, M. Batentschuk, A. Osvet, C. Brabec, Radiat. Meas., 56 (2013) 134-138.
[149] V. Gorbenko, A. Krasnikov, M. Nikl, S. Zazubovich, Y. Zorenko, Opt. Mater., 31 (2009) 1805-1807.
[150] Y. Zorenko, V. Gorbenko, T. Zorenko, V. Savchyn, M. Batentschuk, A. Osvet, C. Brabec, J. Lumin., 154 (2014) 198-203.
[151] Y. Zorenko, V. Gorbenko, V. Savchyn, A. Suchocki, H. Wrzesinski, K. Walczyk, K. Fabisiak, P. Bilski, A. Twardak, Opt. Mater., 36 (2014) 1685-1687.
[152] W.T. Carnall, G.L. Goodman, K. Rajnak, R.S. Rana, J. Chem. Phys., 90 (1989) 3443-3457.
[153] C.R. Ronda, T. Jüstel, H. Nikol, J. All. Compd., 275–277 (1998) 669-676.
[154] C.-H. Kim, I.-E. Kwon, C.-H. Park, Y.-J. Hwang, H.-S. Bae, B.-Y. Yu, C.-H. Pyun, G.-Y. Hong, J. All. Compd., 311 (2000) 33-39.
[155] M. Bettinelli, A. Speghini, F. Piccinelli, A.N.C. Neto, O.L. Malta, J. Lumin., 131 (2011) 1026-1028.
[156] A.J. Silversmith, D.M. Boye, K.S. Brewer, C.E. Gillespie, Y. Lu, D.L. Campbell, J. Lumin., 121 (2006) 14-20.
[157] E. Cavalli, L. Esposito, J. Hostaša, M. Pedroni, J. Eur. Ceram. Soc., 33 (2013) 1425-1434.
[158] P.F. Smet, A.B. Parmentier, D. Poelman, J. Electrochem. Soc., 158 (2011) R37-R54.
[159] X.-C. Jiang, L.-D. Sun, C.-H. Yan, J. Phys. Chem. B, 108 (2004) 3387-3390.
[160] M.A. Gilleo, S. Geller, J. Phys. Chem. Solids, 10 (1959) 187-190.
[161] K. Li, C. Shen, Optik., 123 (2012) 621-623.

[162] H.K. Yang, H.M. Noh, J.H. Jeong, Solid State Sci., 27 (2014) 43-46.
[163] W. Zhang, J. Cen, Z. Hu, H. Wu, X. Sheng, L. Luo, Adv. Powder Technol., 24 (2013) 21-25.
[164] R. Skaudzius, A. Katelnikovas, D. Enseling, A. Kareiva, T. Jüstel, J. Lumin., 147 (2014) 290-294.
[165] D. Boal, P. Grunberg, J.A. Koningstein, Phys. Rev. B., 7 (1973) 4757-4763.
[166] K. Richter, R. Wannemacher, J. Heber, D. Mateika, J. Lumin., 47 (1990) 169-175.
[167] L.-M. Shao, X.-P. Jing, J. Lumin., 131 (2011) 1216-1221.
[168] A.R. West, Solid State Chemistry and its Applications, John Wiley & Sons, Chichester, 1984.
[169] P. Dorenbos, J. Lumin., 134 (2013) 310-318.
[170] P. Dorenbos, J. Lumin., 111 (2005) 89-104.
[171] G. Blasse, J. Solid State Chem., 4 (1972) 52-54.
[172] V. Jubera, J.P. Chaminade, A. Garcia, F. Guillen, C. Fouassier, J. Lumin., 101 (2003) 1-10.
[173] R.A. Sa Ferreira, S.S. Nobre, C.M. Granadeiro, H.I.S. Nogueira, L.D. Carlos, O.L. Malta, J. Lumin., 121 (2006) 561-567.
[174] Y.C. Chang, C.H. Liang, S.A. Yan, Y.S. Chang, J. Phys. Chem. C, 114 (2010) 3645-3652.
[175] M. Kawata, H. Toshima, Y. Miyazawa, S. Morita, J. Cryst. Growth, 128 (1993) 1011-1015.
[176] K. Binnemans, C. GorllerWalrand, J. Phys-Condens. Mat., 9 (1997) 1637-1648.
[177] Z.G. Wei, L.D. Sun, C.S. Liao, X.C. Jiang, Y. Chun-Hua, Y. Tao, X.Y. Hou, X. Ju, J. Appl. Phys., 93 (2003) 9783-9788.
[178] I.E. Kolesnikov, D.V. Tolstikova, A.V. Kurochkin, A.A. Manshina, M.D. Mikhailov, Opt. Mater., (2014) DOI:10.1016/j.optmat.2014.06.015.
[179] M. Marezio, J.P. Remeika, P.D. Dernier, Acta Crystallogr. B, 24 (1968) 1670-1674.

[180] J.L. Wu, G. Gundiah, A.K. Cheetham, Chem. Phys. Lett., 441 (2007) 250-254.